3D Printed Engineered Living Materials with Genetically Programmed Mechanical Properties and Bioproduction Performance for the Design of Functional Objects and Therapeutic Delivery Platforms

Gokce Altin Yavuzarslan

A dissertation

submitted in partial fulfillment of the

requirements for the degree of

Doctor of Philosophy

University of Washington

2024

Reading Committee:

Alshakim Nelson, Chair

Hal Alper

Lara Gamble

Program Authorized to Offer Degree:

Molecular Engineering and Sciences

University of Washington

Abstract

3D Printed Engineered Living Materials with Genetically Programmed Mechanical Properties and Bioproduction Performance for the Design of Functional Objects and Therapeutic Delivery Platforms

Gokce Altin Yavuzarslan

Chair of the Supervisory Committee:
Alshakim Nelson
Department of Chemistry

The synergy of synthetic biology and materials science yields innovative strategies to find alternative approaches for environmental, medical, and manufacturing challenges. Among these approaches, Engineered Living Materials (ELMs) stand out as a promising platform. ELMs, are a distinctive class of smart materials, which are synthetic living systems where genetically modified microorganisms are integrated into a polymer network, forming functional objects. The material properties and applications are determined by the cellular platform and the encapsulating polymer network. Nevertheless, gaps still exist in the seamless integration of biotic (cellular) and abiotic (polymer) components into a singular material, followed by their assembly into devices and machines. Herein, two different biocompatible polymer networks were developed including (i) a protein-based composite, bovine serum albumin (BSA) – poly

(ethylene glycol) diacrylate (PEGDA), and (ii) a synthetic matrix comprising PEGDA-glycerol. These photocurable polymer networks were designed for processing ELMs in light-based 3D printing technologies. The relationships between embedded microorganisms and surrounding polymer matrices were investigated with respect to microbial viability, microbial proliferation behavior, bioproduction capacity, and mechanical properties of ELMs. Subsequently, the interactions between engineered microbial metabolites (L-dopa, betaxanthin, and proteinase A) and protein-based (BSA-PEGDA) polymer matrix were utilized to program mechanical stiffness and degradation time points as desired of 3D printed ELM objects. In an alternative strategy, the polymer concentration of the synthetic matrix (PEGDA-Glycerol) was adjusted to tune the toughness and moduli of 3D printed ELM bioreactors. Finally, an innovative approach toward ELMs for advanced drug delivery was developed using metabolically engineered probiotic strains and 3D printed medical stents. These ELM stents were designed to detect inflammatory biomarkers and initiate responses through the secretion of anti-inflammatory small molecules. This strategy presents a substantial opportunity for facilitating long-term, localized delivery.

TABLE OF CONTENTS

LIST OF FIGURES

LIST OF TABLES

ACKNOWLEDGEMENTS

Embarking on the journey of a Ph.D. is both lengthy and exhilarating, and I extend my heartfelt gratitude to my Principal Investigator, Professor Alshakim Nelson for his unwavering guidance and support throughout this intellectual exploration. I am deeply thankful to Professor Hal Alper, Dr. James O. Park, Professor Lilo Pozzo, and Professor James Carothers for their invaluable guidance in our collaborative projects. Special thanks to my esteemed committee members, Professor Cole A. DeForest and Professor Lara Gamble, whose insightful questions and discussions have significantly enhanced my research perspective and skill set. Working with these pioneering professors and their esteemed research groups has been a truly enriching experience. I extend my appreciation to the current members and alumni of the Nelson Lab for their collaboration and contributions to our collective research endeavors. A special acknowledgment goes to the instrumental labs of the Chemistry Department, Molecular Analysis Facility, and Biology Department Imaging Center for their invaluable support. I express my sincere gratitude to The Scientific and Technological Research Council of Turkiye (TUBITAK) for supporting my Ph.D. studies during the first two years, enabling me to delve into my research with dedication.

To my cherished family and friends, your unwavering support has been a constant presence throughout my Ph.D. journey and beyond. My deepest thanks to my dear mother, Aynur Altin, for enveloping me in her love and tranquility, to my dear sister, Dr. Nazli Altin, for her consistent encouragement, and to my dear late father, Avni Altin, whose love and support I continue to feel. I am profoundly grateful for the endless support of my dear husband, Dr. Mithat Yavuzarslan.

This journey has been enriched by the collective efforts of these individuals and institutions, and I am truly grateful for the privilege of their presence in my academic and personal life.

CHAPTER 1. ENGINEERED LIVING MATERIALS (ELMS)

1.1 ABSTRACT

Engineered Living Materials (ELMs) have emerged as promising platforms for diverse applications, ranging from the human body to extreme environments and space exploration. This chapter explores the immense potential of ELMs in supporting global sustainability and addressing key challenges facing humanity. By combining microorganisms within a polymer matrix, ELMs offer unique features such as genetic control, sustained metabolite production, and self-sustainability. Inspired by natural systems, ELMs draw from bacterial biofilms, the gut microbiome, and algal-fungi co-cultures, enabling resilience in harsh conditions and stimuli-responsive properties. Applications include therapeutic ELMs for oral delivery, 3D-printed bioreactors, and biobatteries for on-demand chemical and energy production. ELMs also contribute to sustainable architecture as self-healing, adaptable, and environmentally friendly building materials. Beyond Earth, ELMs show potential for supporting long-duration space missions by addressing challenges in sustaining life. This chapter highlights the diverse capabilities of ELMs and their role in bio-inspired innovation for a sustainable future.

1.2 INTRODUCTION

In the quest to support global sustainability and general improvement of humankind, there is significant interest among the synthetic biology and material science communities to craft versatile platforms to expand deployment of current scientific breakthroughs to a range of varied and extreme settings ranging from the human body to the built environment. Beyond that, innovative solutions are needed to pave the way to design settlements even outside Earth for

establishment of new civilizations. Engineered Living Materials (ELMs), composite materials comprising microorganisms that are embedded within a polymer matrix, have emerged in recent years as platforms with high potential for deployment in industrial and remote settings (**Figure 1**). In particular, the combination of the biotic and abiotic elements in ELMs can allow for an array of

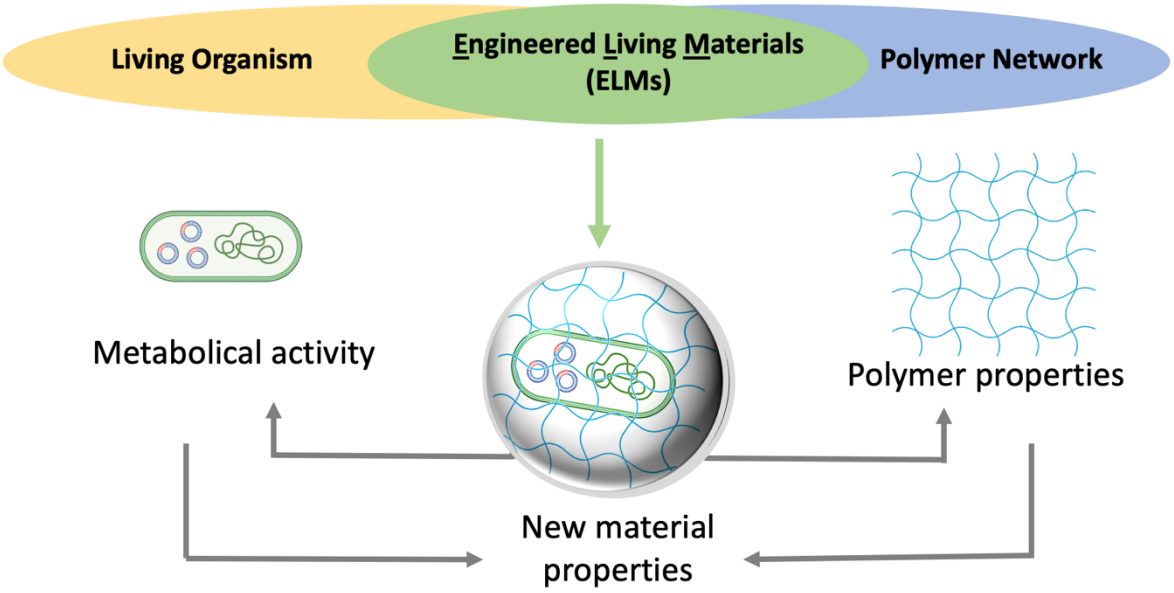

Figure 1.1. General design of engineered living materials.

features including genetic control over material properties[1,2], sustained metabolite productionn[3,4], processivity compatible with advanced manufacturing techniques to obtain desired 3D form factors[5,6] and a range of self-sustainable properties, including self-healing[7], shape memory[8], and sense/response capacity[9]. At this point, ELMs have the potential to offer unique solutions for diverse applications, particularly in on-demand bioproduction, green energy, space exploration, and sustainable built environments.

In the pursuit of more sustainable and resilient materials, many developed ELMs draw inspiration from natural systems that have evolved to thrive in extreme environments such as bacterial biofilms in industrial pipelines, the mammalian gut microbiome, and the algal-fungi co-

culture found in lichens. With integration of broader advancements in synthetic biology and polymer science, ELMs can be designed not only to maintain viability in harsh environments but also with a range of continuous or stimuli-responsive properties[7,8,9]. For instance, stimuli-responsive therapeutic ELMs for oral delivery have been developed to sense and treat inflammations in the gastrointestinal tract, in which living organisms in ELMs maintain viability while passing through a highly acidic gastric environment[9,10].

ELMs also have the potential to revolutionize the way we produce and power our world by enabling the distributed manufacture of chemical compounds and energy. Fabrication of 3D-printed bioreactors and biobatteries from ELMs enables the on-demand production of various chemicals[3-6] and energy[11-16], respectively. An important aspect of this approach is the possibility of reducing the environmental footprint associated with large-scale industrial processes by localizing and sustaining manufacturing. In addition to reducing the environmental footprint, using ELMs in architectural structures as self-healing, adaptable, and environmentally friendly building materials[17-19] helps to reduce the carbon footprint associated with construction. Moreover, introducing the photosynthetic ELM[20] to build design allows to fabrication of CO_2 consuming structures that contribute to the fight against climate change.

The applicability of ELMs is even extendable beyond the boundaries of our planet. Due to their capability to adapt to extreme conditions and to provide continuous resources, ELMs can provide support for long-duration space missions[21-24]. They have the potential to address the challenges of sustaining materials such as food, oxygen, medicine, energy sources, and building materials that are necessary to sustain life.

In this chapter, the immense potential of ELMs for enhancing sustainable development and how they can help humanity to address key challenges of our time are highlighted. Herein, we

examine the remarkable capabilities of ELMs, focusing on their diverse applications ranging from distributed manufacturing of chemicals and energy to therapeutic delivery within the body. Furthermore, we cover some of the intriguing features of ELMs, including shape responsiveness and self-healing capabilities, which will provide a powerful strategy for bio-inspired innovation in the future.

1.3 ELMS AS ON-DEMAND BIOPRODUCTION PLATFORMS

Industrial supply chains, for instance chemicals, energy, and pharmaceuticals, have heavily relied on centralized manufacturing and distribution channels for several decades. On the other hand, in the 21st century, the requirement for portable, on-demand, and distributed bioproduction systems has become essential to address or minimize issues associated with centralized manufacturing. Especially in challenging contexts like disease-affected areas, conflict zones, and space exploration. Currently, engineered living materials stand as promising candidates for creating portable, on-demand, and distributed bioproduction platforms.

In recent years, several groups have dedicated efforts to developing resilient Engineered Living Materials (ELM) platforms for bioproduction, catering to compounds of diverse molecular weights and complexities. An early example involved the use of spore-laden agarose hydrogels, showcasing on-demand chemical production resilience against various stresses like desiccation, solvents, and pH, owing to the inherent robustness of *B. subtilis* spores[25]. Extending this resilience to more conventional microbial chassis, Johnston *et al.* engineered ELMs using shear-thinning and self-healing functionalized pluronic hydrogels (F127-bis-urethane methacrylate). These ELMs, encapsulated with yeast or bacteria, demonstrated sustained production of small molecules and peptides from monocultures and consortia[6]. Notably, these ELMs remained resilient to desiccation, and recent advancements include an optimized preservation procedure allowing at least one year

of room temperature storage[26]. This breakthrough opens avenues for novel on-demand bioproduction applications, including remote military and space missions to provide essential drugs or chemicals.

Progressing toward Engineered Living Materials (ELMs) compatible with the production of both industrial and therapeutic proteins, Yuan *et al.* introduced the Bio-Produced Proteins on Demand (Bio-POD) platform[2]. This innovation facilitates cold-chain-independent protein production of up to 150 kDa. Beyond confirming that the base F127-BUM scaffold does not hinder the diffusion of larger products, this study underscores the superiority of ELMs in terms of absolute titer, reusability, and resilience to lyophilization compared to liquid culture methods. Expanding the utility of ELMs in biosynthetic routes with more than a few steps, Brooks et al. recently demonstrated the compatibility of ELMs with synthetic tripartite consortia for de novo synthesis of phenylpropanoids[3]. This work not only accesses microbial biosynthesis of phenylpropenes like eugenol but also emphasizes the effectiveness of spatially segregated strains for coculture stability over multiple reuse cycles. The observed enhanced stability in spatially segregated ELMs, compared to liquid culture counterparts, suggests potential translation to an industrial setting where long-term culture stability is economically crucial. Besides advancing bulk culture stability, efforts to integrate ELM scaffolds with inducible gene expression systems have yielded proof-of-concept platforms for bioproduction cycling[1]. The platform's capacity for oscillatory production and seamless product switching within a single culture over days to weeks demonstrates significant potential for the implementation of more efficient bioproduction platforms adaptable to fluctuating demands.

Apart from conventional scaffolds like alginate, hyaluronic acid, agarose, or pluronic-based structures, jammed hydrogel microparticles (HMPs) using a diverse range of base materials

have emerged as promising candidates for Engineered Living Materials (ELMs). Notably, the ability of these particles to adopt a 'jammed' state, responsible for their 3D printable properties such as shear-thinning and self-healing behavior[27], is independent of the particle composition. Exploiting this characteristic, Li *et al.* demonstrated the 3D printability and curing potential of jammed, yeast - laden HMPs, resulting in viable ELMs[28]. Addressing the crucial factor of printable cell density, which significantly influences intrinsic ELM productivity, Qian *et al.* previously established a method for 3D printing freeze-dried yeast cells with an unprecedented cell loading exceeding 75% by volume[29]. Both studies showcased higher biocatalytic activity in 3D printed lattices compared to bulk hydrogels of the same weight, likely attributed to improved mass transfer rates facilitated by increased surface area.

Beyond broadening the range of applicable chassis, product classes, scaffold materials, and productivity of Engineered Living Materials (ELMs), it is crucial to focus on efforts that enhance the compatibility of ELMs with efficient downstream processing (DSP) for the widespread industrial adoption of these bioproduction technologies. Addressing this need, Gao et al. have devised microbial-laden alginate ELMs, demonstrating the stability of cell viability and biocatalytic activity in pure organic solvents[4]. This platform not only facilitates ELM-based production of compounds incompatible with aqueous growth media but also streamlines downstream processing of organic products compared to systems requiring organic/aqueous biphasic production systems to sustain cell viability. Furthermore, Li *et al.* have recently introduced permeability-engineered, multi-layered microgels featuring an outer sieve layer that provides precise control over the permeability of molecules entering and exiting the gels[30]. Such a system holds the potential to enable DSP-light biomanufacturing, where selective diffusion of products from ELMs into the surrounding media eliminates the need for initial filtration steps to

remove cell debris before additional purification. Future advancements in this field should focus on seamlessly integrating these developments into comprehensive end-to-end bioprocessing workflows.

In addition to their role in bio-producing chemicals and pharmaceuticals, ELMs hold significant potential for sustainable energy production and storage. ELM platforms, notably employed as microbial fuel cells (MFCs), attract widespread industrial interest due to their capability for simultaneous wastewater treatment, electricity generation, and storage. For instance, biocomposites featuring the electrochemically active bacteria *S. oneidensis* have proven both robust to 3D printing processes[11] and capable of oscillating between energy generation and storage[12]. Advances in materials science, such as optimizing cell deposition density and function at the anode, utilizing Ag-Au core-shell nanowire foams[13], double layer alginate hydrogels[14], self-assembling reduced graphene oxide/polypyrrole hydrogels[15], and polyaniline–sodium alginate–graphene oxide (PANI–SA–GO)/carbon brush (CB) hydrogels[16], have contributed to improvements in cell viability and MFC performance. Progress has also been made in synthesizing robust air-breathing cathodes, enhancing MFC efficiency through improved oxygen reduction at the cathode[31,32]. While many systems have employed electrochemically active bacteria or microalgae, recent developments include MFCs with self-modified hydrogel anodes utilizing the yeast *Cystobasidium slooffiae* JSUX1 for enhanced electricity generation and hydrogen production from xylose[33]. Despite promising progress, further development is essential to enhance power generation and wastewater treatment efficiency, and to reduce manufacturing costs at scale, ultimately facilitating the commercialization of MFC technology.

1.4 ELMS IN THE REALM OF HIGH-PERFORMANCE MATERIALS

Self-healing and shape-morphing materials are a type of stimuli-responsive materials that respond to chemical and physical changes. In the context of ELMs, these changes can be governed by genetic expression within encapsulated organisms, or with stimuli-responsive polymers that comprise the extracellular matrix. Designing materials with self-healing properties is an important issue for the sustainability of new materials, as they offer a cheap and easy way to repair the possible damages in the material. As a type of living system, ELMs can exhibit self-healing properties due to their metabolic activity. The applicability of self-healing ELMs has been recently studied in different areas such as textiles[34], bricks[17], robotic skin[7], and wearable medical sensors[35]. The use of microbial extracellular matrices is one of the strategies for gaining self-healing behavior in ELM. Fungal mycelium and bacterial extracellular matrix are the most common types of materials that are used in tailored self-healing properties of ELM[7,34-37].

Mycelium materials are made from the vegetative part of filamentous fungi, and they have natural self-assembly and self-healing properties as the formation of network-like hyphal structures led to the ability that naturally fill void spaces within an existing matrix[7,17,34]. Elsacker *et al.* investigated the self-healing mechanism of a fungal mycelium material which was fabricated from Basidiomycete fungal species *Ganoderma lucidum*. Even though they observed that dried and plasticized mycelium materials can be reactivated for regeneration by rehydration, the healing process was not under control. Because newly sprouted hyphae have grown in all directions, not just towards the void. Instead of using pure mycelium ELMs, formulating ELMs by combining the fungal organism with polymer matrices allows controlling the self-healing behavior of ELMs as well as allowing them to be obtained as 3D form factors. For instance, a hydrogel formulated with agar, κ-carrageenan, and cellulose-based thickener was loaded with the fungus *Ganoderma*

lucidum and 3D printed by DIW into lattice architectures[7]. Since the self-healing behavior of mycelium-ELM is related to fungal growth in a hydrogel, the effect of growth rate on self-healing was evaluated by preparing specimens with different nutrient concentrations. To do that, 3 mm incisions were created for each sample and after an initial lag phase of mycelia, the self-healing rate was found 0.6-0.7 mm day $^{-1}$ if the nutrient concentration is higher than the threshold value of 6 %. The mechanical properties of the healed material were also evaluated. It was found that after the healing process, the material became stronger and stiffer.

Similar to fungal mycelium, bacterial extracellular matrices have also been used to gain re-generation properties of ELM[35,36]. Caro-Astorga *et al.*, showed that bacterial cellulose spheroids which are secreted from *Komagataeibacter rhaeticus* can be used to heal ELMs constructed from bacterial cellulose material. Freshly grown spheroids were able to heal the punctured hole within 3 days and restored the consistency and appearance of the original material. The mechanical properties of the healed material were reported weaker than the original material, still, it was found that after healing the material retained 40% of its tensile strength and 58% of its Young's modulus. In another study[37], curli nano fibers which are secreted from genetically modified *E. coli* were used to create cell-laden curli nanofiber-ELM hydrogel. When this ELM is placed in conditions that promote cell growth, ELM hydrogel is capable of growing and regenerating itself. Moreover, the rheological properties of curli nanofiber-ELM hydrogel were modulated by either genetically encoded factors or processing steps that allowed to process of the curli nanofiber-ELM spraying or extrusion. The self-healing properties of ELM are mostly related to cell growth in the ELM matrix with the presence of appropriate nutrients, thus healing time depends on the cellular proliferation rate which takes time. To overcome this issue, Chen *et al.*, programmed membrane proteins of *E. coli* and engineered two different *E. coli* strains which have nanobody-antigen pairs.

These bacterial strains are cultured separately and when they are mixed, they adhere to each other. Due to nanobody–antigen pairs in this bacterial material, it has fast recovery under stretching, bending, and self-healing properties. More importantly, the self-healing of this bacterial material not only depends on cellular growth but is also governed by adhesion between nanobody-antigen pairs. Thus, self-healing happens within several minutes.

As another type of stimuli responsiveness shape-morphing materials respond to chemical or physical inputs by changing their original shape. Programming shape morphing properties of ELM allowed to use of them as actuators[8,38] in the soft robotic areas and controlled release of therapeutic[8,39] in biomedical applications. In polymer science shape changing generally can be achieved by temperature, pH, or light changes. On the other hand, in ELM cell growth can be used for stimulation of shape morphing like in self-healing ELM. Rivera-Tarazone *et al.*, formulated ELM with *S. cerevisiae* cells which are embedded in a polyacrylamide matrix and showed that how shape changing of this ELM in aqueous media is mainly contributed by mechanical forces generated by the cell proliferation of *S. cerevisiae* rather than swelling of polyacrylamide gel. By using this phenomenon, they fabricated a 2D ELM sheet and killed cells designated areas by UV exposure (254 nm), and then this 2D ELM sheet was incubated in culture media. Within incubation cells in non-UV exposed areas proliferated which resulted in a change of the original shape from 2D to 3D. The control of cell proliferation by genetic modifications also allows for a program of the proliferation-induced shape-changing of ELMs. For instance, genetically modified *S. cerevisiae* which only proliferates in the presence of L-histine was used to design shape-morphing ELM. 2D ELM sheet was designed by killed-cell and alive-cell area and it only takes 3D helical shape when it was cultured with L-histidine[38]. Multi-material printing is another strategy to place different metabolically engineered strains, which proliferate by the presence of different

biochemical cues, in different areas in the same ELM object. By controlling chemical inputs in culture media, sequential growth can be tuned which leads to controlled shape-morphing [8].

1.5 IN SITU BIOPRODUCION OF THERAPEUTICS WITHIN THE BODY BY ELMS

In recent years, progress has been made towards using probiotic therapeutics to treat GI-related diseases as well as to support healthy gut microbiomes. One of the main limitations of probiotic therapeutic delivery via oral administration is poor survival rate of probiotics in gastric and intestine areas. Over the past decades, different microencapsulation methods such as spray drying[40], freeze drying[41], and electrospinning[42] have been developed to improve probiotic survival rates. On the other hand, designing of probiotic-containing ELMs as probiotic delivery platforms can not only improve the survival rate of probiotics, but also enhance colonization of them, and enable design of controlled probiotic release platforms. While targeted tissue delivery via oral probiotic drug formulations remains challenging, using such systems for treatment of gut-localized diseases (where probiotic niches naturally reside) such as IBD and colon cancer is likely to be more immediately tractable in a clinical setting. Furthermore, links between gut microbiome state and other tissues including the gut-brain axis, gut-liver axis, gut-skin axis, as well as links of gut dysbiosis with diseases including cancer, obesity, diabetes, and rheumatoid arthritis, highlight the potential for gut-localized ELM treatment modalities to have wide-ranging impact over many clinical indications in the future. Major requirements for safe, efficacious ELM closed-loop therapies include response to medically relevant concentrations of disease biomarkers, delivery of

sufficient quantities of therapeutic payload when needed, as well as extended retention and activity within the gut to avoid frequent intervention by patients or healthcare providers.

Recent advancements in highly sensitive and specific bacterial biosensors coupled with robust polymer encapsulation[43] and low-power electronics[44,45] have enabled ELMs capable of tracking and diagnosing active inflammation in the gut. Beyond sensing, much attention in this field has been given to development of ELM platforms for development of robust oral living therapeutic formulations robust enough to withstand the harsh gastric environment and reach out to the colon area for colonization of probiotics. Working towards improved IBD therapies, several recent works have highlighted the propensity of polymeric encapsulation to enhance efficacy towards *in vivo* mouse colitis models through enabling more robust functioning of wild type probiotics[46], co-delivery of probiotics and small molecule drugs for synergistic therapies[47], improved survival and metabolic function of engineered, ROS-scavenging probiotics[48], and application of novel polymeric formulations which selectively disrupt niches of colitis-associated species and prompt colonization of delivered probiotics[49].

Natural biopolymers such as alginate[47], cellulose[50,] and chitosan[48] are the commonly used materials in traditional probiotic-ELM formulations yet novel ELM designs centralized on the development of platforms with controlled probiotic release ability beyond maintaining cell survival in the GI tract. Inflammation markers such as ROS and NO have been selected as a chemical stimulus in recent ELM designs which are formed by chemically responsive crosslinkers. For instance, ROS-responsive probiotic ELM hydrogel formulated with alginate/polyvinyl alcohol microspheres which were crosslinked by 1,4-phenylenediboronic acid[9]. Since ROS attacked

carbon−boron bonds, the cross-linked hydrogel was disrupted with the presence of ROS in the gut and subsequently, ROS-scavenging probiotics were released. In another study, NO responsive cross-linking agent, N, N-(2-Amino-1,4-Phenylene) diacylamine, was used to fabricate a poly-γ-glutamic acid network in probiotic-ELM design[10]. NO reacts with N, N-(2-Amino-1,4-Phenylene) diacylamine irreversibly which led to the dissociation of ELM matrix and releasing of probiotics.

ELMs comprised of engineered probiotics that synthesize their own extracellular polymeric components have additionally shown efficacy in mouse colitis models via promotion of intestinal mucosal healing[50,51,52]. The microbial extracellular components serve as an encapsulation matrix as probiotics become embedded into this matrix while colonization progresses. This *in situ* encapsulation also allows for continual matrix formation and protects probiotics from adverse factors in disease areas such as competitive pathogens and antibiotic-mediated perturbations[51]. Beyond probiotic protective effects, microbial extracellular matrices can also be programmed with therapeutic properties for mucosal healing. For example, *Escherichia coli* Nissle 1917 (EcN) has been genetically engineered to synthesize curli nanofibers displaying trefoil factors as a therapeutic extracellular matrix, with mucosal healing and immunomodulation shown *in vivo*[52]. Even though probiotic-ELM formulations are promising as oral probiotic delivery platforms, they are largely still limited in the number of cargo releases and not largely applicable for long-term drug delivery. Future progress is thus needed to achieve ELM treatment modalities for chronic conditions, in which probiotic-laden polymeric matrices are stable for months to years without a need for intervention by a medical professional.

Beyond therapeutic activity within the body, ELMs can be developed for applications in external wound healing. Prior efforts have demonstrated the propensity of encapsulated spores to

secrete fluorescent reporters in the presence of *S. aureus* infection[25], which could be combined with a capacity to secret antibiotics to yield a closed-loop system in the future. In this vein, development of ELM nanofibrillar patches for application as sustained-release bacterial skin dressings[53] has recently been reported. Additionally, photoautotrophic ELMs with cyanobacteria/heterotrophic bacteria consortia encapsulated in a hydrogel matrix have been shown to convert light into functional biomolecules for wound healing[54]. Furthermore, development of ELMs with blue light-responsive violacein production for application as a spatiotemporally controlled skin therapeutic[55] highlights impressive progress towards the achievement of closed-loop therapeutic ELMs for external use cases.

CHAPTER 2. ADDITIVE MANUFACTURRING OF ENGINEERED LIVING MATERIALS WITH BIO-AUGMENTED MECHANICAL PROPERTIES AND RESISTANCE TO DEGRADATION

This chapter is adapted with permission from Altin-Yavuzarslan, G., Brooks, S. M., Yuan, S. F., Park, J. O., Alper, H. S., & Nelson, A. Additive Manufacturing of Engineered Living Materials with Bio-Augmented Mechanical Properties and Resistance to Degradation. *Advanced Functional Materials*, 2300332. Copyright 2023, Wiley, Online Library.

2.1 ABSTRACT

Engineered living materials (ELMs) combine living cells with polymeric matrices to yield unique materials with programmable functions. While the cellular platform and the encapsulating polymer network determine the material properties and applications, there are still gaps in our ability to seamlessly integrate the biotic (cellular) and abiotic (polymer) components into singular material, and then assemble them into devices and machines. Herein, we demonstrated the additive manufacturing of ELM hydrogels wherein bioproduction of metabolites from the encapsulated cells enhanced the properties of the surrounding biopolymer matrix. First, we developed aqueous resins comprising bovine serum albumin (BSA) and poly(ethylene glycol diacrylate) (PEGDA) with engineered *E. coli* or *S. cerevisiae* for vat photopolymerization to create objects with a wide array of 3D form factors. The BSA-PEGDA biopolymer matrix afforded hydrogels that were mechanically stiff and tough for use in load-bearing applications. Second, we demonstrated the continuous *in situ* production of L-DOPA, naringenin, and betaxanthin from the engineered cells encapsulated within the BSA-PEGDA biopolymer matrix. These microbial metabolites bioaugmented the properties of the biopolymer matrix by enhancing the stiffness (L-DOPA) or resistance to enzymatic degradation (betaxanthin). Finally, we demonstrated the assembly of the

3D printed ELM components into mechanically functional bolts and gears to showcase the potential to create functional ELMs with useful form factors. The advanced manufacturing of bio-augmented functional parts via *in-situ* chemical production have broad implications for the fabrication of biochemically and mechanically functional synthetic living machines.

2.2 INTRODUCTION

The convergence of synthetic biology and polymer science has led to the rapid emergence of engineered living materials (ELMs), which are bio-composite materials comprised of engineered cells embedded within polymeric matrices. ELMs have the potential to attain a level of precision, control, responsiveness, and chemical recyclability unachievable with traditional, abiotic materials[1-6]. The synergistic effect of coupling living cells with abiotic material components enables bio-augmentation of material properties and function[35,56,57]. Bio-augmentation occurs when *in-situ* production of chemical agents introduces a new function or capability to the material, and/or contribute to material properties in manner that is complementary to the existing polymer matrix. In both cases, the polymeric material does not serve simply as a passive containment matrix for cells, but rather a chemical canvas upon which synergy between the cells and polymer matrix can be exerted. While the minimum requirements for fully living, bio-augmented ELMs are cell viability and metabolic activity, the implementation of ELMs at their fullest potential requires advanced manufacturing processes to fabricate desired three-dimensional (3D) form factors, in addition to establishing a synergy between the embedded cells and polymer matrix for material performance.

Hydrogel ELMs have been successfully fabricated via advanced manufacturing processes such as 3D-bioprinting[56,57]. Specifically, direct-write extrusion 3D-printing has been successful in the fabrication of sensors, bioreactors, actuators, drug screening kits and microfluidic

devices[2,6,35,58-61]. However, this method of 3D-printing is limited in the complexity of the geometrical form factors that can be produced. Alternatively, vat photopolymerization is an additive manufacturing technique that allows for a greater range of geometrical designs that can vary in shape and connectivity[10,11,12]. In vat photopolymerization processes, objects are produced from a liquid resin in an additive fashion using visible light in a pattern-wise manner. Importantly, liquid resins must have both low viscosity (<10 Pa·s) and fast photocuring (at 405 nm) to achieve successful 3D-printing with high resolution[61,62,63]. Vat photopolymerization resins that can further incorporate and sustain microbial activity could provide an opportunity to create ELMs with greater geometrical complexity.

In this work, we posit that bovine serum albumin (BSA) is an ideal component for developing ELM resins for vat photopolymerization 3D printing as it affords mechanically robust hydrogels that exhibit high moduli and toughness (compressive modulus of 6.3 Mpa[65], which is comparable to articular cartilage[68]). These protein-based materials are also enzymatically degradable, which creates a route to a closed-loop life cycle for these materials. Recently, two different strategies have been developed to synthesize BSA-based resins for vat photopolymerization. These strategies include functionalization of the BSA surface lysines with methacrylic anhydride[65] or the conjugation of BSA with polyethylene glycol diacrylate (BSA-PEGDA)[66].

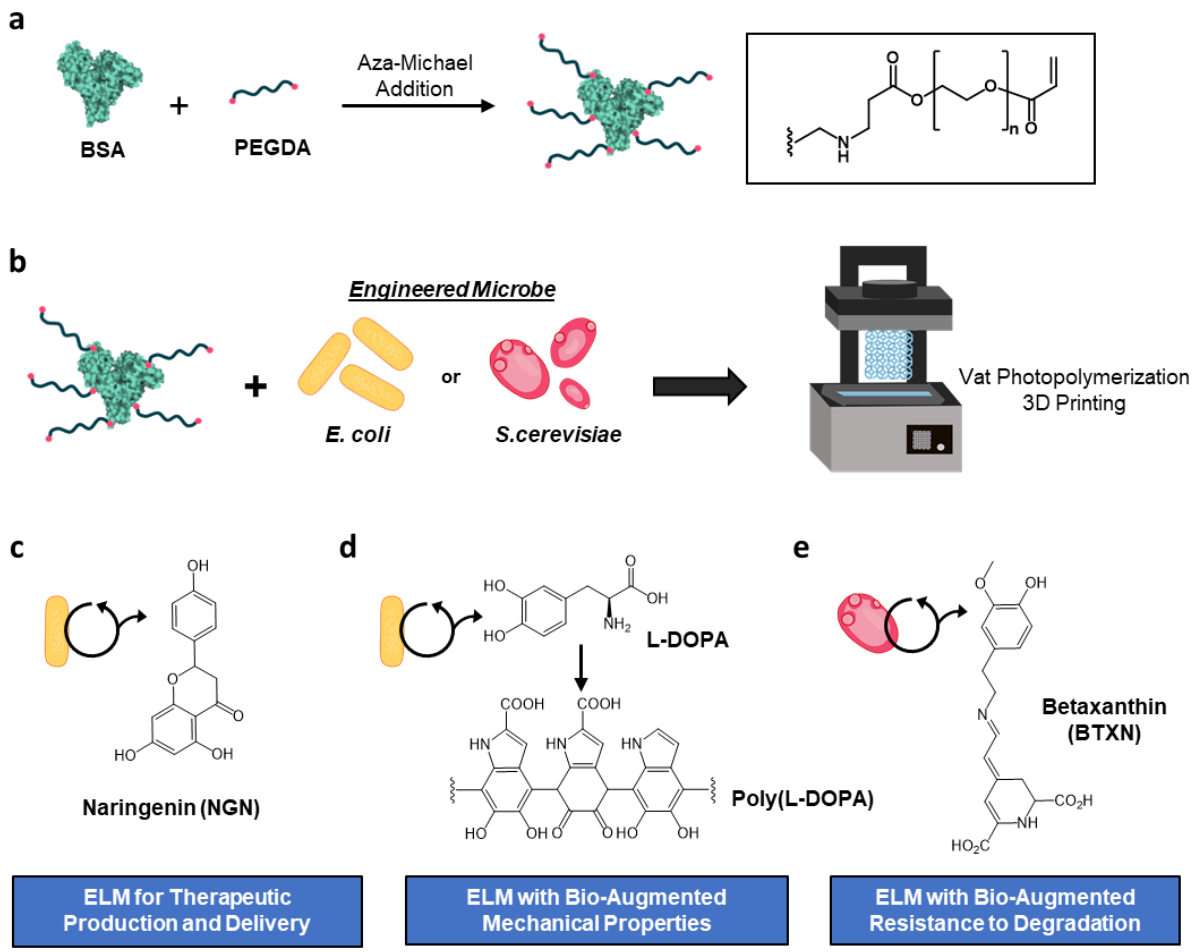

Figure 2.1. Additive manufacturing of ELMs with bio-augmented functionality and mechanical properties. a) BSA was functionalized via aza-Michael addition to afford pendant PEG-acrylate groups. b) Engineered *E. coli* or *S. cerevisiae* was added to the PEG-functionalized BSA to create an aqueous based resin for vat photopolymerization. The microbes were entrapped within the polymerized BSA-PEGDA hydrogel network. *E. coli* were engineered to produce c) naringenin or d) L-DOPA (the L-DOPA polymerized to afford poly(L-DOPA), and *S. cerevisiae* was engineered to produce betaxanthins. The 3D printed ELMs are referred to as ELM-EC-NGN, ELM-EC-LDOPA, or ELM-SC-BXN, respectively. (EC = *E. coli*, *S*C = *S. cerevisiae*, LDOPA = L-DOPA, BXN = betaxanthin, and NGN = naringenin).

While these BSA-PEGDA materials can be synthetically manipulated to alter physical properties, we hypothesized that engineered microbes could be incorporated into these protein-based matrices to produce bio-augmented ELMs endowed with new functionality that is either not inherent to the protein-polymer matrix or exceed the traits of BSA-PEGDA matrix alone. Previous studies have used microbial metabolites as the product of ELM bioreactors or to improve the

mechanical properties of ELMs with the production of microbial biopolymers such as genetically engineered protein nanofibers[1], bacterial cellulose[69,70], microbial pellet[71], bacterial biofilm[72]. On the other hand, there are still opportunities to select metabolites that can specifically interact with the surrounding polymer matrix to affect the mechanical properties.

Herein, it is demonstrated the additive manufacturing of ELM hydrogels wherein bioproduction of metabolites from the encapsulated cells bio-augment the innate properties of the surrounding BSA-PEGDA matrix (**Figure 2.1**). Vat photopolymerization was used to fabricate ELM hydrogels that were mechanically stiff and a range of object geometries. *E. coli* was engineered for the *in-situ* production of L-DOPA to enhance the mechanical stiffness of an ELM (ELM-EC-LDOPA); naringenin production was used to demonstrate an ELM (ELM-EC-NGN) for continuous production of a therapeutic compound (as a comparative example of bio-augmentation); and *S. cerevisiae* was engineered to produce betaxanthin to afford an ELM (ELM-SC-BXN) that could resist microbial degradation. As a final proof of concept, it is demonstrated the future potential for this field by 3D-printing robust ELM hydrogels as machine parts that can be assembled into mechanically functional ELM devices.

2.3 RESULT AND DISCUSSION

2.3.1 *ELM resins for vat photopolymerization 3D-printing*

ELM resins were created by adding the engineered microorganisms to an aqueous solution of BSA-PEGDA conjugates (**Figure 2.1**). The resins in this study were optimized for their printability based on their rheometric characterization. We first evaluated the viscosity of the resin formulations to ensure that the viscosity was <10 Pa·s. We, and others, have observed that this is ideal to ensure sufficient reflow during vat photopolymerization and to resolve finer features[65,66,73]. All the aqueous resins developed in this study were comprised of 30 wt% BSA with 0.075 wt%

$Ru(bpy)_3Cl_2$ and 0.24 wt% sodium persulfate as the photo-initiating system. PEGDA was added to the formulation for the conjugation of PEGDA to BSA via an aza-Michael addition reaction[66]. We investigated resin formulations that contained 3, 5, or 10 wt% PEGDA to identify the minimum amount of PEGDA required for printability. All three of the resin formulations had viscosities that were <1 Pa·s. (**Figure 2.2 a**).

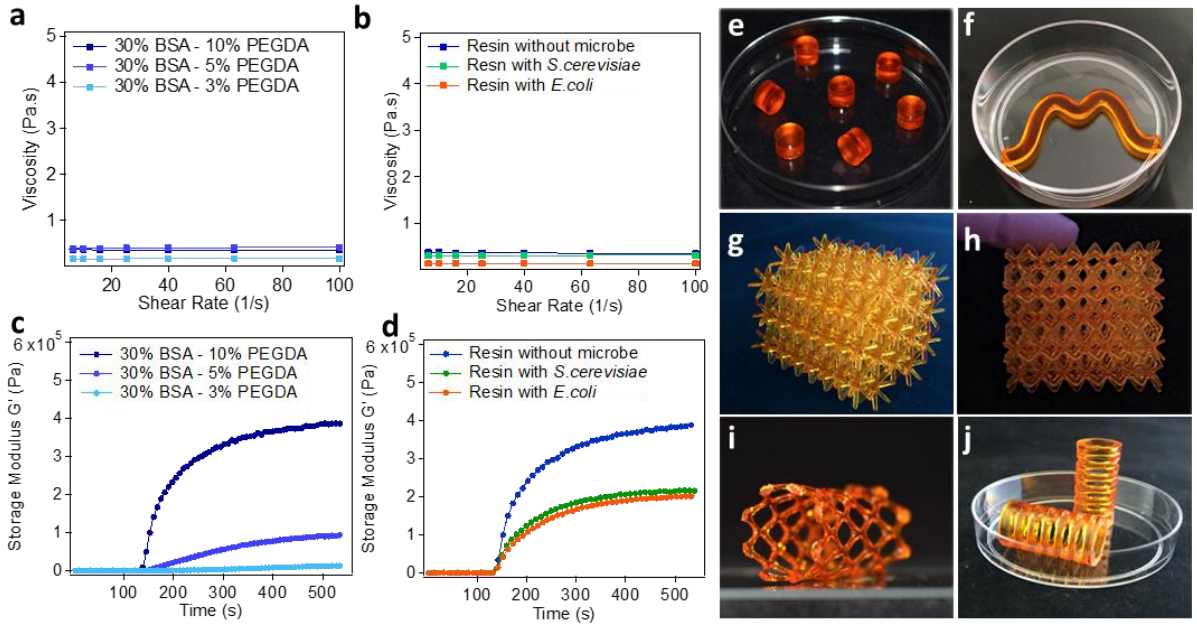

Figure 2.2. Rheological characterization and representative examples of ELMs 3D printed via vat photopolymerization. Graphs show minimal changes to the viscosity of the BSA-PEGDA solutions with a) different PEGDA concentrations, and b) in the presence and absence of microorganisms. Photorheometry experiments were performed to evaluate the change in the storage modulus (G', Pa) over time upon irradiation with 365 nm light, which was turned on after 120 s. The resulting graphs show the increase in the storage modulus for c) different PEGDA concentrations, and d) in the presence and absence of microorganisms. Optical images of 3D printed ELMs: e) 7 small cylinder-shaped constructs (in a 50 mm petri dish as a frame of reference); f) a wave-shaped construct (in a 50 mm petri dish); g) and h) lattice-shaped constructs (x=39.1 mm, y=33.6 mm, z=34.21 mm); i) stent-shape lattice (57.8 mm, y=33.4 mm, z=30.6 mm) and j) spring-shaped construct (in a 50 mm petri dish).

We next evaluated the time to reach gel-point (time at which storage modulus (G') = loss modulus (G")) and the rate of photocuring for each of the cell-free resins with different PEGDA concentrations in response to 405 nm light exposure. Photorheometry was used to evaluate the changes to G' and G" over time as the sample was irradiated with light. Although all the formulations were low viscosity fluids to start, their G' increased upon irradiation.

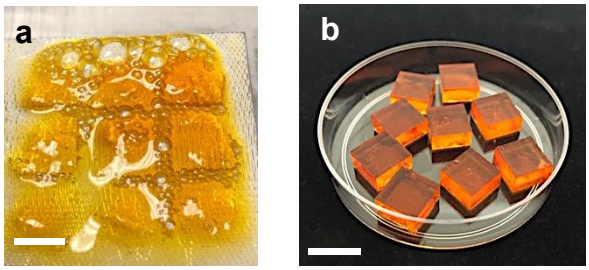

Figure 2.3. Optical images of SLA 3D printed constructs. a) Formulation of 30 wt% BSA with 5 wt% PEGDA (Entry 2, Table 2.1), unsuccessful printing, delamination was observed. b) Formulation of 30 wt% BSA with 10 wt% PEGDA (Entry 3, Table 2.1), printing was successfully completed.

The formulations with 3 wt% and 5 wt% PEGDA were insufficient to be used as SLA printable resins and failed to give successful prints (**Figure 2.3 a**). The gel-point was reached after 47.5 s and 20 s for the two resins, respectively (**Table 2.1**). An increase in the PEGDA concentration to 10 wt% further decreased the time required to reach gel-point to 4 s, which is suitable for a commercial Formlabs Form 2 printer. Similarly, the 10 wt% formulation exhibited the fastest rate of photocuring (**Figure 2.2 c**, **Table 2.1**). We found that 30 wt% BSA 10 wt% PEGDA showed the optimum concentration to formulate SLA printable resin for ELMs. To determine whether the addition of *E. coli* or *S. cerevisiae* to the resin formulations affected the viscosity and rate of photo curing, we added these cells (1 ml of cell culture, $1x10^9$ cells/mL for *S. cerevisiae* and $1x10^{10}$ cells/mL for *E. coli*, to 20 g of resin) to the resin formulation containing 30 wt% BSA and 10 wt% PEGDA. We observed that the addition of cells did not significantly alter the rheometric properties of the resin (**Figures 2.2 b, d, Table 2.1**). After the addition of microbial

culture media, resins were stirred for 30 min at 200 rpm to maintain homogenous distribution of microorganism in the resin. It has been observed that when the 30 wt% BSA, 10 wt% PEGDA formulation was stirred for 30 min at 200 rpm the viscosity was changed 1.0 Pa. s (Entry 3, **Table 2.1**) to 0.35 Pa. s (Entry 4, **Table 2.1**). Therefore, it may be said that the viscosity reduction of Entry 5, Entry 6, Entry 7, and Entry 8 was mainly caused by stirring step rather than the addition of microorganism or culture media to the resin formulation. According to the findings, Entry 1 and Entry 2 required longer time, 47.5 s and 20 s, respectively, to reach the crossover point compared to other formulations (**Table 2.1**). This longer time is not desirable to obtain 3D printed constructs in SLA 3D printers (**Figure 2.3 a**). When PEGDA concentration was increased from 3 wt% to 10 wt%, the resin reached the crossover point at least 10 times faster (Entry 3, **Table 2.1**). Presence of more PEGDA units in 30 wt% BSA, 10 wt% PEGDA formulation led to the reaction of the acrylate groups with each other more easily. Therefore, this formulation provided faster photocuring rate and shorter time to achieve crossover point (Entry 3, **Table 2.1**). 3D printed objects were successfully obtained with formulation 30 wt% BSA, 10 wt% PEGDA (Fig. 3b). In ELM formulations (Entry 6, and Entry 8, **Table 2.1**) both stirring step (30 min at 200 rpm) and presence of microbial culture could affect the time to reach crossover point and rate of photocuring (Entry 6 and Entry 8, **Table 2.1**). On the other hand, these changes did not affect the SLA. The optimized aqueous ELM resins were 3D-printed to afford a range of cell-laden object geometries that included cylinders, lattices, and tubular stents (**Figures 2.2 e-j**). These hydrogels were mechanically stiff, and therefore, could sustain its printed shape.

Table 2.1. Effect of PEGDA concentration and microbial culture media on rheological properties and SLA 3D printability of BSA-PEGDA conjugates.

Entry	BSA wt. %	PEGDA wt. %	Microbial Culture Media	Viscosity (Pa s)	G' rate change (Pa/s)	Crossover point (s)	Printability
1	30	3	-	0.17	0.003	47.5	No
2	30	5	-	0.40	70.45	20.0	No
3	30	10	-	1.00	2884.1	4.0	Yes
4*	30	10	-	0.35	-	-	Yes
5	30	10	LB	0.27	3535.07	10.0	Yes
6	30	10	*E. coli*	0.13	1238.82	13.5	Yes
7	30	10	YPD	0.35	1088.56	8.0	Yes
8	30	10	*S. cerevisiae*	0.30	1620.55	12.0	Yes

* Entry 4 was stirred for 30 min before measurement similar to Entry 5-8. These samples were stirred after the addition of microbial culture and/or culture media to provide the homogenous distribution of added compounds to resin formulation.

2.3.2 *Cell distribution and morphology of cells in 3D-printed ELMs*

One of the lesser-studied aspects of ELMs is cell distribution and proliferation in 3D-printed networks. This distribution plays an important role in understanding the optimal geometries and dimensions of ELMs as well as the potential for homogenous, *in situ* production of bio-augmented compounds.

Micro computed tomography (μCT) imaging showed the growth and distribution of the cells within the hydrogels in the hydrated state. After first printing, the cells were not visible in these scans owing to an initial low cell seeding density. As the cells proliferated within the hydrogels, the cell populations have been starting to image after 4 days (**Figure 2.4 a**). The light-orange regions in dark orange are represents the *S. cerevisiae* colonies. When the samples cultured over 21 d, high cell density were observed in μCT (**Figure 2.4 b**), which showed the *S. cerevisiae* cells were able to growth in BSA-PEGDA network, similar in time but different in spatial organization from another ELM formulation we previously studied.

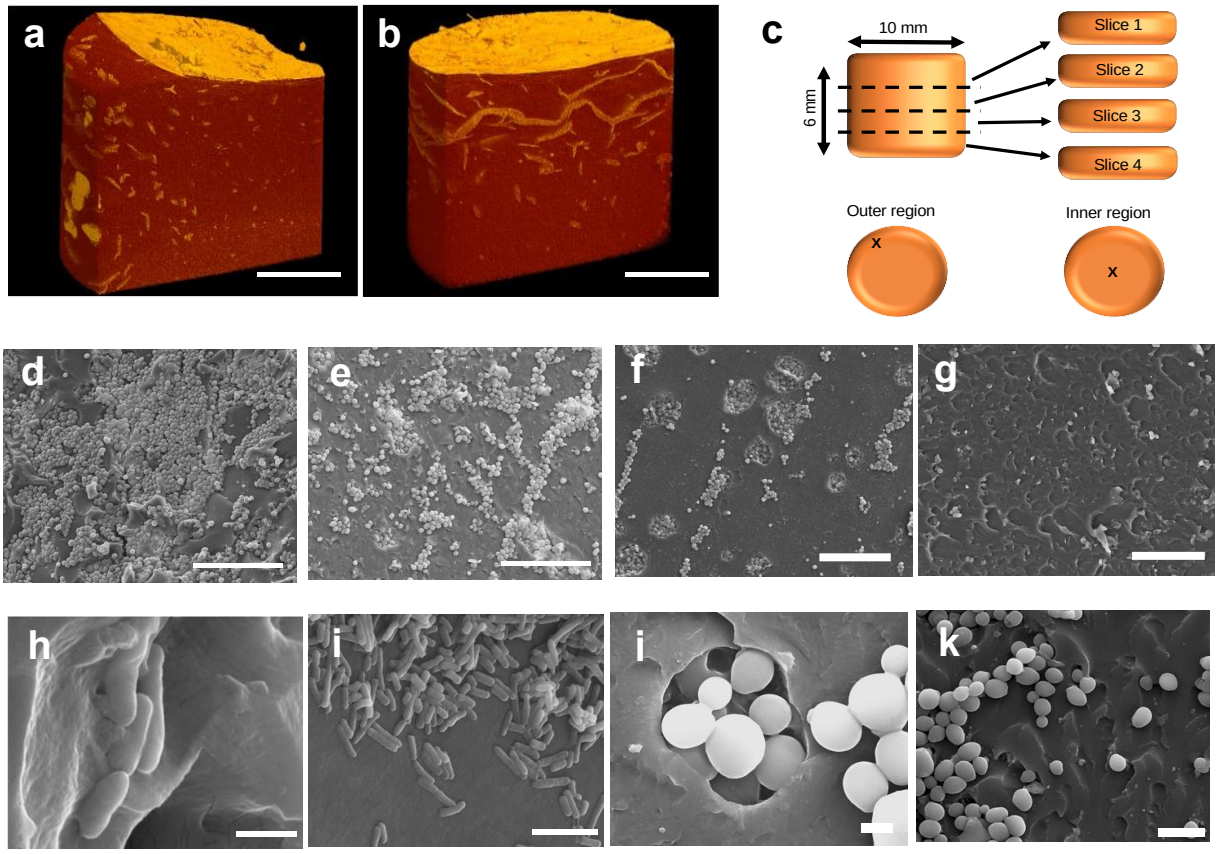

Figure 2.4. Cell growth and distribution were observed using μCT and SEM imaging of the ELMs. μCT image of *S. cerevisiae* in ELM-SC-BXN hydrogel after a) 4 d and b) 21 d of culturing (scale bar = 50 μm). c) Illustration showing the sample sectioning that was performed to evaluate the distribution of the cells within different regions of a 3D printed cylindrical construct. SEM images of *S. cerevisiae* in a 3D printed cylindrical ELM-SC-BXN construct in: d) the outer region of slice 1 at 500x magnification (scale bar = 50 μm); e) the inner region of slice 1 at 500x magnification (scale bar = 50 μm); f) the outer region of slice 2 at 500x magnification (scale bar = 50 μm); and g) the inner region of slice 2 at 500x magnification (scale bar = 50 μm). SEM images of *E. coli* in a 3D printed cylindrical ELM-EC-LDOPA construct at h) 20000x magnification (scale bar = 1 μm) and **i,** 5000x (scale bar = 5 μm). SEM images of *S. cerevisiae* in a 3D printed cylindrical ELM-SC-BXN construct at j) 7000x magnification (scale bar = 2 μm) and k) at 2500x magnification (scale bar = 10 μm).

Scanning electron microscopy (SEM) analysis of the dehydrated cylindrical samples were additionally used to assess the cell distribution and proliferation throughout the printed structure. Cross-sectional images were taken from different regions of a printed cylinder (**Figure 2.4 c**) of

ELM-SC-BXN and ELM-EC-LDOPA after 3 d of culturing, which showed the presence of spherical-shaped yeast cells[22] and rod-shaped bacterial cells,[75] respectively (**Figure 2.4**).

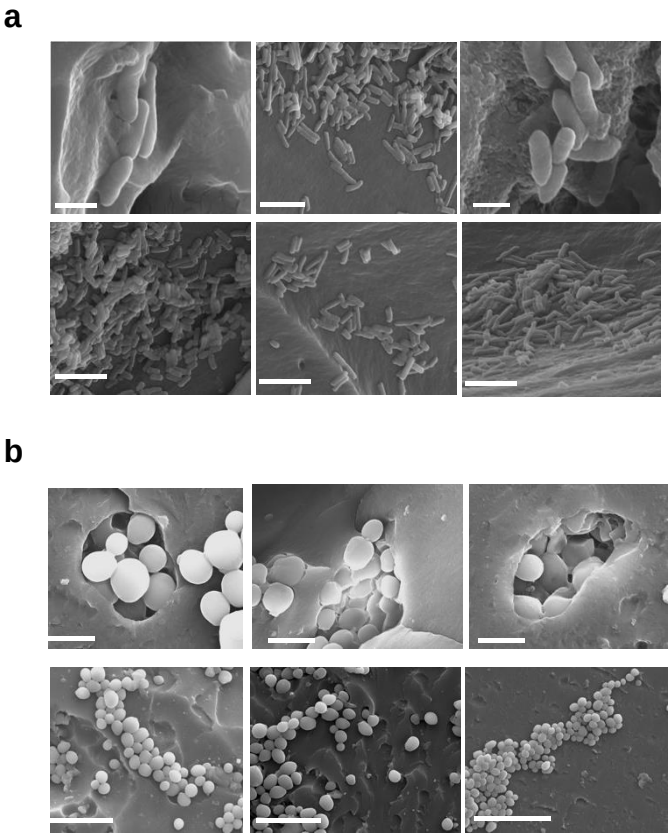

Figure 2.5. Morphology of cells in 3D printed ELMs. a) SEM images of *E. coli* in 3D printed ELM-EC-LDOPA constructs at different magnifications; 1000X magnification (scale bar 20 micron), 5000X (scale bar 5 micron), 20000X (scale bar 1 micron), b) SEM images of *S. cerevisiae* in 3D printed ELM-SC-BXN constructs at different magnifications; 1500X magnification (scale bar 20 micron), 2500X (scale bar 10 micron), 7000X (scale bar 2 micron).

The outer regions of the cylinder possessed the highest cell density (**Figures 2.4 d-f**) relative to the inner core regions (**Figures 2.4 e-g**), a phenomenon consistent with the 3D-reconstructed μCT images (**Figures 2.4 a, b**). The difference in cell density between the surface and core of the printed cylinder is likely attributed to the gradient of available nutrients that may exist, with highest nutrient concentration at the outer surface in contact with the culturing media. The SEM images also proved the cell growth process in 3D printed BSA-PEGDA constructs. *S. cerevisiae* forms

colonies process named budding[74]. In SEM images, both globose and ellipsoid in shape single *S. cerevisiae* cells (**Figures 2.4 j**, **2.5 b**) and small, medium, and large types of *S. cerevisiae* buds were observed (**Figure 2.4 j**, **Figure 2.5 b**). The observation of budding forms of *S. cerevisiae* showed that entrapped cells were able to proliferate across the BSA-PEGDA network. In SEM, the cellular surface of entrapped cells (either *E. coli* or *S. cerevisiae*) were visualized as smooth and non-damaged. Thus, it can be concluded that resin components (BSA-PEGDA conjugates, photo-initiator system), and photopolymerization of ELM resin during SLA 3D printing did not show any corrosive effects on entrapped cells.

2.3.3 *Continuous production and effect of bio-augmentation on ELM material properties*

As a first demonstration of bio-augmented manufacturing, we sought to enhance the ELM mechanical properties through incorporation of an engineered *E. coli* that produced L-DOPA (we will refer to this ELM as ELM-EC-LDOPA). L-DOPA can undergo oxidative coupling in the presence of oxygen to afford poly(L-DOPA)[76] (**Figure 2.1 c**) in a manner that can help cross-link and further strengthen the ELM matrix. Bio-adhesive poly(catecholamine)s including poly(dopamine), poly(norepinephrine), poly(epinephrine), and poly(L-DOPA) have been used as surface coating agents in applications such blood contact devices[77], wound dressing gels[78] and electro-biosensors[79]. The poly(catecholamine) coatings can form conjugates with molecules containing sulfhydryl or amino groups via Michael-addition or Schiff-base reaction based on phenolic hydroxyl or quinone groups[76,77,80]. ELM-EC-LDOPA was 3D-printed, and we confirmed *in situ* L-DOPA production over the course of 5 d where the titer reached 199.0 ± 3.2 mg/L (**Figure 2.6 a**).

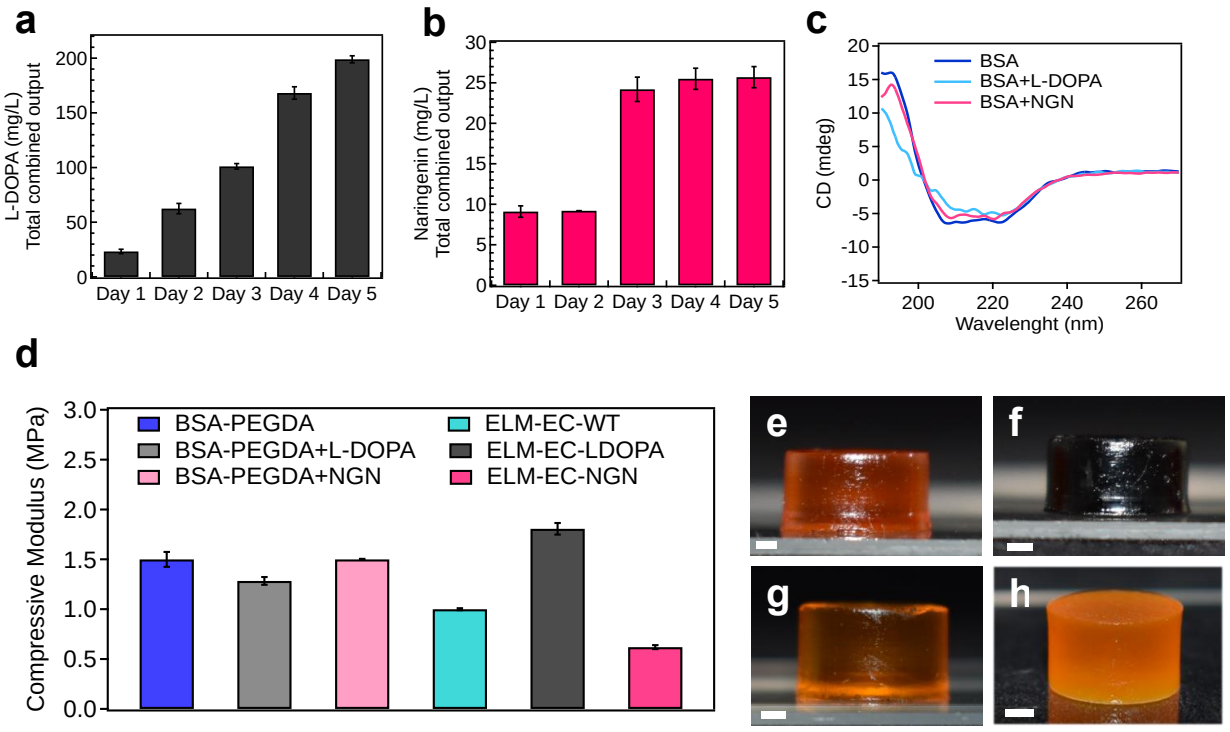

Figure 2.6. The continuous production of naringenin and L-DOPA were monitored over time and their effect on ELM moduli were characterized. a) Graph showing continuous L-DOPA production from ELM-EC-LDOPA over 5 d. Samples were prepared in triplicate; error bars represent ±5 s.d. b) Graph showing continuous naringenin production from ELM-EC-NGN over 5 d. Samples were prepared in triplicate; error bars represent ±1.5 s.d. c) CD spectra of BSA, BSA+L-DOPA (wherein L-DOPA was exogenously added to a solution of BSA), and BSA+NGN (wherein naringenin was exogenously added to a solution of BSA). BSA showed a negative peak that reach a maximum between 222 to 208 nm, which corresponds to α–helical structure. In the BSA+L-DOPA sample, the maximum peak was observed between 222 to 217 nm which suggests that the α–helical structure of BSA was altered by the presence of L-DOPA, but not naringenin. d) Uniaxial compression experiments were performed to obtain the compressive moduli for BSA-PEGDA, BSA-PEGDA+L-DOPA, BSA-PEGDA+NGN, ELM-EC-WT, ELM-EC-LDOPA and ELM-EC-NGN. Samples were prepared in triplicate; error bars represent ±0.07 s.d. Optical images of 3D printed cylindrical constructs after 5 d of culturing: e) BSA-PEGDA; f) ELM-EC-LDOPA; g) ELM-EC-NGN; h) ELM-SC-BXN.

Interestingly, while ELM-EC-LDOPA initially had an orange-brown color (primarily from the ruthenium photocatalyst), the structure turned black after 5 d of culture (**Figure 2.6 f**). L-DOPA production and subsequent oxidation can form dark intermediate products such as melanin-like compounds and poly(L-DOPA) derivatives[77]. UV-vis and CD spectroscopies confirmed that L-DOPA can bind directly to BSA.

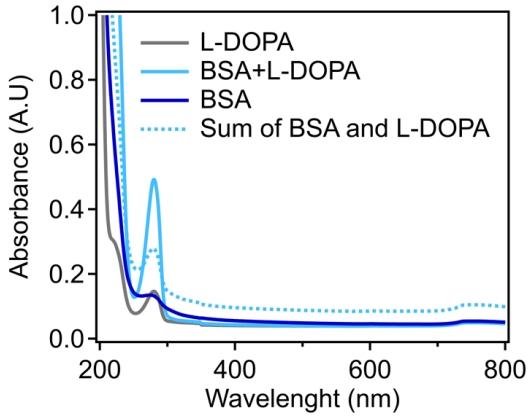

Figure 2.7. Interaction of L-DOPA to BSA. UV-absorption spectra of BSA, L-DOPA, sum of individual spectra of BSA and L-DOPA, and spectra of BSA+L-DOPA mixture.

We observed an increase in the strong UV-vis absorption band (280 nm) of BSA[81,82] upon the addition of L-DOPA, which was greater than the sum of the individual absorbance intensities of BSA and L-DOPA (**Figure 2.7**), thus indicating L-DOPA interactions with BSA. A small shift was also observed in the CD spectrum for BSA upon the addition of L-DOPA (**Figure 2.6 c**) corresponding to changes in the α-helical structure of the protein[82,83]. The obtained spectroscopic results provide evidence for L-DOPA binding with BSA. Uniaxial compression experiments were used to evaluate the mechanical properties of ELM-EC-LDOPA and showed that the bio-augmented ELM enabled by production of L-DOPA afforded enhanced stiffness. Specifically, the compressive modulus of BSA-PEGDA network (without cells) increased from 1.5 ± 0.08 MPa to 1.8 ± 0.06 MPa ($p = 0.017$) with the *in-situ* production of L-DOPA in ELM-EC-LDOPA (**Figure 2.6 d**). This increase in stiffness was not observed in any other instantiation of materials or ELMs that were often marked by decreases in stiffness when cells were present. For example, ELMs that were produced from wild type *E. coli* (ELM-EC-WT) without the production of L-DOPA, exhibited a decrease in elastic modulus of the BSA-PEGDA network (compared to the condition without cells) from 1.5 ± 0.08 MPa to 1.0 ± 0.01 MPa ($p = 0.013$) after 5 d of culturing (**Figure**

2.6 d). As another comparison, BSA-PEGDA (without cells) was exposed to L-DOPA exogenously by soaking the printed construct in a solution of L-DOPA (200 mg/L) for 5 d.

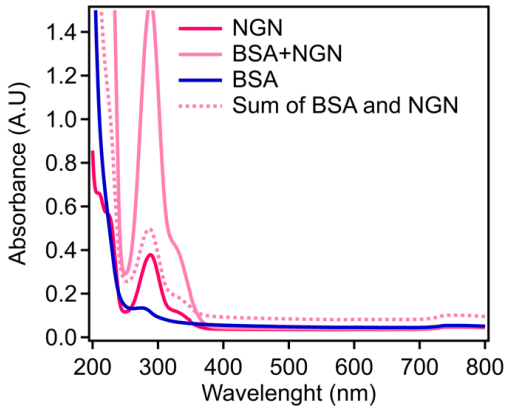

Figure 2.8. Interaction of naringenin (NGN) to BSA. UV-absorption spectra of BSA, NGN, sum of individual spectra of BSA and NGN, and spectra of BSA+NGN mixture.

The elastic modulus of these samples was 1.3 ± 0.04 MPa, which was lower than that of the ELMs with *in-situ* L-DOPA production (**Figure 2.6 d**). The difference ($p = 0.0015$) is attributed to the difference in the distribution of L-DOPA throughout the material. With the exogenous introduction of L-DOPA to printed samples, incorporation of L-DOPA can be limited by its diffusion into the matrix and likely more pronounced in the outer surface. In contrast, *in-situ* production offers the advantage of localized production and distribution of L-DOPA for enhanced mechanical properties via bio-augmentation. To show the specificity of the effect of L-DOPA-BSA interaction on mechanical enhancement, we tested the mechanical properties of ELM-EC-NGN. First, we evaluated the metabolic activity of an ELM to produce the flavonoid structure therapeutic, naringenin[84,85,86]. *In-situ* naringenin production was confirmed by LC-MS (**Figure 2.6 b**) over 5 d. The naringenin titer was 9.1 ± 0.7 mg/L after 1 d of culturing in media and reached 25.7 ± 4.9 mg/L after 5 d. The instability of naringenin in liquid culture media may affect the titered amount in LCMS. The binding of naringenin to BSA was confirmed by UV-vis and CD spectroscopy. Although naringenin can interact with albumin protein[87,88] (**Figure 2.8**), this interaction did not

cause conformational changes on BSA. The CD experiments confirmed that naringenin did not change the secondary structure of BSA, as both BSA and BSA+NGN samples showed the same CD spectrum (**Figure 2.6 c**). As expected, the i*n-situ* production of naringenin did not increase the compressive modulus of the ELMs (**Figure 2.6 d**). This trend indicates that ELM bio-augmentation is strongly dependent on the choice of bioactive compound produced and its interaction with the surrounding polymer matrix.

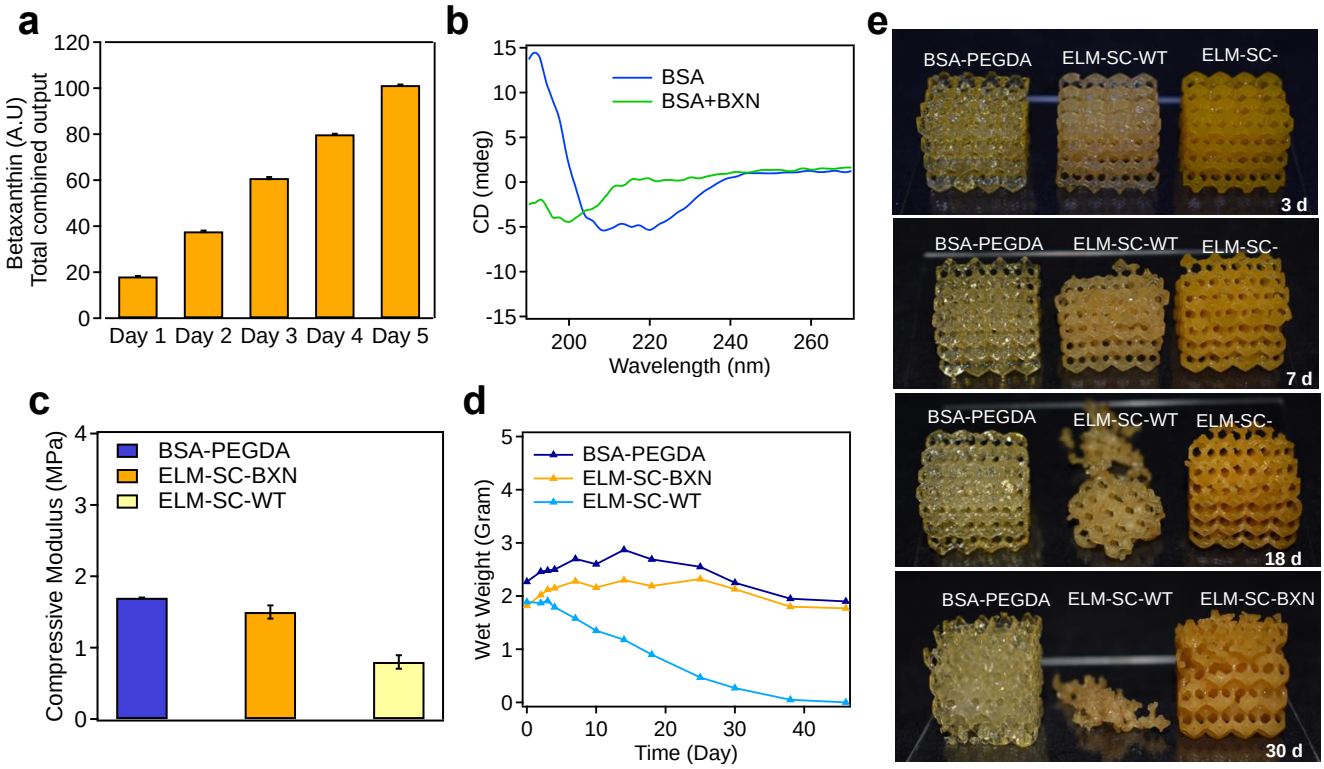

Figure 2.9. The effect of continuous betaxanthin production on microbial degradation of ELM constructs. a) Continuous betaxanthin production from ELM-SC-BXN over 5 d. Samples were prepared in triplicate; error bars represent ±0.5 s.d. b) CD spectra of BSA and BSA+BXN (wherein betaxanthin was exogenously added to a solution of BSA). c) Uniaxial compression experiments were performed to obtain the moduli for BSA-PEGDA, ELM-SC-BXN and ELM-SC-WT. Samples were prepared in triplicate; error bars represent ±0.09 s.d. d) Mass change of BSA-PEGDA, ELM-SC-BXN and ELM-SC-WT during degradation and e) optical images of BSA-PEGDA, ELM-SC-BXN and ELM-SC-WT over 30 d degradation period.

As a second demonstration of bio-augmented manufacturing of ELMs, we sought to control degradation through a protective metabolite production. Microorganisms will exogenously secrete enzymes to degrade or remodel an extracellular matrix[89], especially protein derived materials. Interestingly, we discovered that ELMs that produced betaxanthin from engineered *S. cerevisiae* (ELM-SC-BXN) resisted microbial degradation compared to ELMs that contained wild-type *S. cerevisiae* (ELM-SC-WT) (**Figure 2.9**). CD spectroscopy of BSA in the presence of betaxanthin shows a significant change in the secondary structure of the protein (unlike other molecules such as L-DOPA and naringenin). This difference suggests that betaxanthin is specifically binding to the BSA and disrupting its folded conformation (**Figure 2.9 b**). Binding of betaxanthin to BSA also confirmed by UV-vis data (**Figure 2.10**).

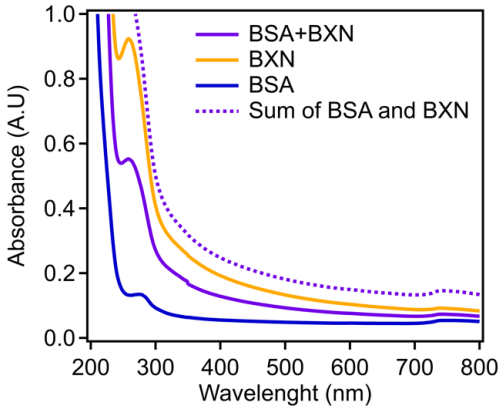

Figure 2.10. Interaction of betaxanthin (BXN) to BSA. UV-absorption spectra of BSA, BXN, sum of individual spectra of BSA and BXN, and spectra of BSA+BXN mixture.

After a few days of culturing, there was a noticeable difference between the stiffness (*p=0.073*) of ELM-SC-BXN and ELM-SC-WT, wherein the betaxanthin-producing ELM had a compressive modulus that was 2-fold higher than the ELM with wild-type cells (**Figure 2.9 c**). On the other hand, we did not find any significant difference (*p = 0.07*) between BSA-PEGDA and ELM-SC-BXN in terms of their elastic modulus (**Figure 2.9 c**). Therefore, we assumed that together with binding to BSA, betaxanthin may also bind to microbial enzyme as well which can

contribute the resistance to microbial degradation in ELM-SC-BXN samples. **Table 2.2** shows the degree of swelling (q) of ELM samples. BSA-PEGDA matrix without cell was used as control for each group.

Table 2.2. Degree of swelling of SLA 3D printed samples. (Samples were prepared in triplicate, (± s.d).

Sample	Degree of Swelling (q)
BSA-PEGDA in LB media	1.56 ± 0.05
ELM-EC-LDOPA	1.34 ± 0.01
ELM-EC-WT	1.56 ± 0.07
BSA-PEGDA+L-DOPA	1.33 ± 0.17
ELM-EC-NGN	2.70 ± 0.4
BSA-PEGDA+NGN	1.10 ± 0.01
BSA-PEGDA in YPD media	1.63 ± 0.03
ELM-SC-BXN	1.61 ± 0.07
ELM-SC-WT	1.89 ± 0.01

Proteinase-K was selected as a model enzyme to show binding of betaxanthin to microbial enzymes which are responsible to protein degradation.

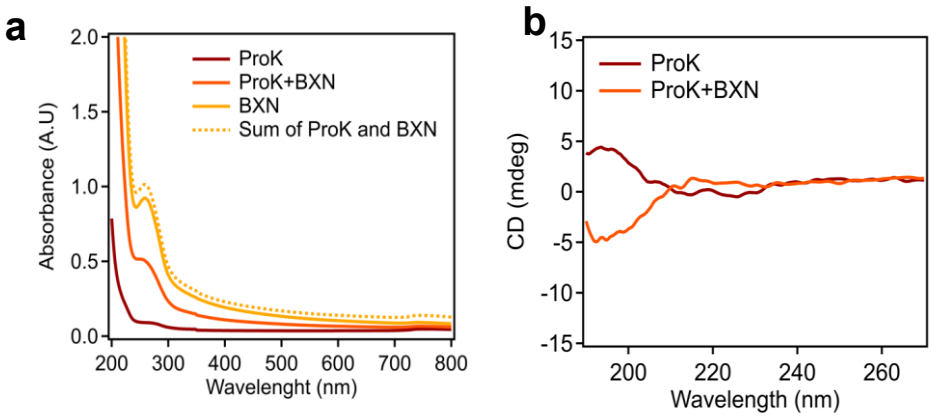

Figure 2.11. Effect of betaxanthin (BXN) on secondary structure of Proteinase K (ProK) a) Interaction of betaxanthin (BXN) to Proteinase K (ProK). UV-absorption spectra of ProK, BXN, sum of individual spectra of ProK and BXN, and spectra of ProK+BXN mixture. b) Effect of betaxanthin (BXN) on the secondary structure of Proteinase K (ProK). CD spectra of ProK with the presence of BXN (ProK+BXN).

Both UV-vis and CD spectroscopy data showed that betaxanthin interacted with Proteinase-K (**Figure 2.11 a**) and change the secondary structure of it (**Figure 2.11 b**). We compared the degradation of lattices printed from BSA-PEGDA, ELM-SC-WT, and ELM-SC-BXN over 45 d culture period (**Figure 2.9 d-e**). ELM-SC-WT showed an onset of mass loss after 3 d, which continued until complete microbial degradation after 38 d. In contrast, ELM-SC-BXN resisted microbial degradation (its performance was similar to BSA-PEGDA (without cells) control sample) and only exhibited a small degree of mass loss over the same period of time. At the end of the degradation period, the viability of ELM-SC-BXN samples was confirmed in agar plating experiments wherein viable cells were successfully cultured (**Figure 2.12**). Notably, ELM-SC-BXN remained intact throughout the culturing period, demonstrating potential for bio-augmented ELMs to be utilized for sustained microbe delivery and bioproduction applications.

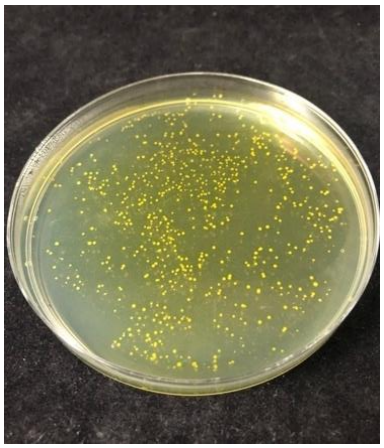

Figure 2.12. The long-term viability of cells in ELM-SC-BXN (samples collected on day 40).

Thus, our findings demonstrate that *in-situ* betaxanthin production can prevent the microbial degradation. Betaxanthin can accomplish this by binding to degradation enzymes and showing enzyme inhibitor effects, or by binding to the BSA molecule and making it resistant to degradation by enzymes.

2.3.4 *Mechanically functional robust ELM hydrogel constructs*

The additive manufacturing of mechanically robust ELMs can enable the future fabrication of soft "living machines" that can be assembled from the printed parts (**Figure 2.13**). A nut and bolt were individually printed using the ELM-EC-LDOPA resin. These two hydrogel components were mechanically stiff, and the nut was successfully screwed onto the bolt (**Figure 2.13 a, b**). As another demonstration, a set of three gears were printed from the ELM-SC-BXN resin and assembled (**Figure 2,13 c, d**). As expected for this device, the rotational motion of one gear was translated to adjacent gears. Our demonstrations show the potential for additive manufacturing as an advanced form of fabrication that will enable future users to print fully functional machines with arbitrary designs using ELMs and benefiting from the bio-augmented function of the cells within them.

2.4 CONCLUSION

The burgeoning field of ELMs is rapidly expanding the scope of synergistic, bio-augmented manufacturing to yield novel materials deployable in diverse settings ranging from on-demand production for natural disaster relief to *in-situ* therapeutic delivery. Successful production and scale-up of these materials requires an understanding of design principles for formulation and production of mechanically robust, bio-augmented systems. To this end, we fabricated ELMs via the additive manufacturing of photocurable BSA-PEGDA conjugates in the presence of engineered microorganisms. 3D-printed ELM constructs with complex geometries such as lattices, stents, bolts, and gears were successfully produced. Furthermore, μCT and SEM images indicated that the cells were viable within the BSA-PEGDA matrices. Despite the heterogeneous distribution of the cells within the cultured constructs, the presence of these cells introduced bio-augmented

material functionality and properties. In particular, the production of L-DOPA and betaxanthin demonstrated the important role that those chemical agents can have upon the properties of ELM. Additional studies are underway to fully understand the factors that control cellular and chemical agent distribution within 3D-printed ELMs.

2.5 EXPERIMENTAL SECTION

2.5.1 *Materials*

Bovine serum albumin was purchased from Nova Biologics, poly(ethylene glycol diacrylate), sodium persulfate, glutaraldehyde, naringenin, L-DOPA, spectinomycin, kanamycin, chloramphenicol, and ampicillin were obtained from Sigma-Aldrich. Tris(2,2′-bipyridyl) ruthenium (II) Chloride Hexahydrate, LB broth powder, LB agar powder, yeast extract, peptone, and glucose were purchased from Thermo Fisher Scientific.

2.5.2 *Preparation of the resin formulation*

Bovine serum albumin (BSA) and poly (ethylene glycol) diacrylate (PEGDA, M_w = 700) were used to synthesize PEGDA modified BSA conjugates. To optimize the PEGDA ratio of BSA-PEGDA conjugates, 3 wt%, 5 wt % and 10 wt% of PEGDA were used against 30 wt% BSA. To synthesize the BSA-PEGDA conjugates, first PEGDA (M_w = 700) was dissolved in DI water. Then, the desired amount of BSA powder was slowly added to PEGDA solution while gently mixed and let them react overnight at 4 °C. $Ru(bpy)_3Cl$ (0.748 mg/g of resin) and sodium persulfate (2.38 mg/g of resin) were added to BSA-PEGDA formulation before SLA 3D printing. To prepare ELM resin formulations, microorganisms, $1x10^9$ cells/mL for *S. cerevisiae* strains and $1x10^{10}$ cells/mL for *E. coli* strains, were added to resin formulation (2 wt%). Desired cell concentration was obtained by OD_{600} measurements.

2.5.3 *Strains, plasmids, media*

All strains, plasmids, and primers used in this study are listed in Table 2 and 3. NEB10β was used for gene cloning or propagation of expression vectors. It was cultivated in LB medium supplemented with appropriate antibiotics (100 μg mL^{-1} ampicillin, 50 μg mL^{-1} kanamycin, 30 ug mL^{-1} chloramphenicol, or 50 μg mL^{-1} spectinomycin (Sigma-Aldrich)) with 225 rpm orbital shaking at 37 °C.

Oligonucleotide primers that were used for PCR amplification were purchased from Integrated DNA Technologies (Coralville, IA). Ligated or Gibson-assembled DNA[90] were electroporated (2 mm Electroporation Cuvettes, Bioexpress) into *E. coli* electrocompetent cells with a BioRad Genepulser Xcell at 2.5 kV. The Frozen EZ Yeast Transformation II Kit (Zymo Research) was used to transform integrative cassettes into the yeast. Plasmids utilized for L-DOPA and Naringenin production were constructed as previously described[6]. For Betaxanthins cassette generation, the DNA fragment amplified from plasmid pCMC0759[91] with primers P1 and P2 was cloned into the amplicon generated from the vector p415-TDH3-dCas9-VPRADH1t-UraInt[92] with primers P3 and P4 via Gibson Assembly, followed by NotI-HF digestion.

The L-DOPA generating strain was created by transforming pCDF-pLPP-B30rbshpaB-hpaC-T7t into a Tyrosine overproducing strain as previously described[4]. The Naringenin generating strain was created by transforming *E. coli* BL21(DE3) with plasmids pETM-PUTRtrxA-TAL-PUTRtalB-4CL, pCDM-PssrA-UTRrpsT-CHS-PUTRglpD-CHI, pACM-PfdeR-mut-FdeR-PfdeA-mut-acpH-asacpT-asacpS, and pRSM-PcspA-mut-PadR-acs-ACC as previously described[91]. To create the Betaxanthins-producing strain, the NotI-HF digested Betaxanthins cassette was gel extracted and transformed into BY4741 yeast, followed by selection

of transformants on dropout media lacking leucine. Correct integrants were screened by colony PCR using primers P5 and P6 and confirmed via Sanger Sequencing.

Table 2.3. Description of strains and plasmids

Strain/plasmid	Description	Source
E. coli strains		
BL21(DE3)	E. coli str. B F– ompT gal dcm lon hsdSB(r_B^- m_B^-) λ (DE3 [lacI lacUV5- T7p07 ind1 sam7 nin5]) [$malB^+$]$_{K-12}$(λ^S)	New England Biolabs
E. coli BL21(DE3) Mut-17	[BL21(DE3)]: pETM-PUTRtrxA-TAL-PUTRtalB-4CL, pCDM-PssrA-UTRrpsT-CHS-PUTRglpD-CHI, pACM-PfdeR-mut-FdeR-PfdeA-mut-acpH-asacpT-asacpS, and pRSM-PcspA-mut-PadR-acs-ACC (KanR, AmpR, SpcR, CmR)	Reference [43]
eBL0430D	[E. coli BL21(DE3)] ΔtyrR , pET28-pYIBN-aroG(fbr)-B30rbs-tyrA(fbr)-tRRNC; KanR , pCDF-pLPP-B30rbs-hpaB-hpaC-T7t; KanR; SpcR	Reference [44]
S. cerevisiae strains		
BY4741	MATα SUC2 gal2 mal2 mel flo1 flo8-1 hap1 ho bio1 bio6 his3Δ1 leu2Δ0 met15Δ0 ura3Δ0	American Type Culture Collection (ATCC)
BY01	*S. Cerevisiae* BY4741: ura3:pCCW12-MjDOD(T261N; ACC to AAC)-pTDH3-CYP76AD5 -tPRM9 (URA3integration with Leu2 marker)	This Study
Plasmids		
pET28-pYIBN-aroG(fbr)-B30rbs-tyrA(fbr)-tRRNC. KanR	For L-DOPA production	Reference [44]
pCDF-pLPP-B30rbshpaB-hpaC-T7t. SpcR	For L-DOPA production	Reference [44]
pETM-PUTRtrxA-TAL-PUTRtalB-4CL	For Naringenin production	Reference [43]
pCDM-PssrA-UTRrpsT-CHS-PUTRglpD-CHI	For Naringenin production	Reference [43]
pACM-PfdeR-mut-FdeR-PfdeA-mut-acpH-asacpT-asacpS	For Naringenin production	Reference [43]
pRSM-PcspA-mut-PadR-acs-ACC	For Naringenin production	Reference [43]

Table 2.4. Primers and sequences

Primer	Sequence (5'-3')
P1	GTGGTTTCAGGGTCCATAAAGCgagctcCTGAACTGGCCGATAATTGC
P2	gatgcgtaaggagaaaataccgcatcaggTAGGTTGTCTGTGCCCATAC
P3	CCTGATGCGGTATTTTCTCCTTACG
P4	GAGCTCGCTTTATGGACCCTG
P5	GAAGGATAAGTTTTGACCATCAAAG
P6	GGTGAAGTTGTAGGTAGAGTAACC

2.5.4 *Culturing of metabolically engineered microorganism and ELM constructs*

S. cerevisiae BY01 and wild type *S. cerevisiae* BY4741 were grown in YPD (10 g L^{-1} yeast extract, 20 g L^{-1} peptone and 20 g L^{-1} glucose) media with 225 rpm at 30 °C. Wild type *E. coli* was grown in LB medium at 37 °C. 50 μg mL^{-1} spectinomycin and 50 μg mL^{-1} kanamycin was added to LB media to culture *E. coli* eBL0430D at 37 °C. To calculate L-dopa production from *E. coli* eBL0430D, antibiotic included LB media was enriched with 10 mM Vitamin C. *E. coli* BL21(DE3) was cultured in LB media contained 30 μg mL^{-1} chloramphenicol, 100 μg mL^{-1} ampicillin, 50 μg mL^{-1} spectinomycin and 50 μg mL^{-1} kanamycin at 30 °C. All strains were incubated in a shaking incubator at 225 rpm.

2.5.5 *Rheology measurements*

TA Instruments Discovery Hybrid Rheometer-2 was used in rheology measurements. Viscosity versus shear rate experiments was performed at a shear rate increasing from 1 to 100 s^{-1}. A 40 mm cone and plate geometry with a cone angle of 1.019°, a solvent trap, and a gap height of 26 μm were used during the analysis. For the photo rheology analysis, the rheometer was outfitted

with a collimated light source (λ = 400 nm, 10 mW cm^{-2}, Thorlabs) that was turned on 120 s after the start of the experiment. The storage and loss moduli were monitored for a total of 150 s at 1% strain and 6.28 rad/s by using a 20 mm parallel plate and a gap height of 1000 μm. Data collection and analysis were carried out with TRIOS software (TA Instruments).

2.5.6 *SLA 3D Printing*

A Formlabs Form 2 printer was used to fabricate SLA 3D printed ELM constructs in the Open Mode with a layer height of 100 μm. 3D models were designed in Autodesk Fusion 360 or downloaded from Thingiverse. After 3D printing, samples were removed from the build plate, rinsed in DI water to remove any uncured resin, and post-cured in a custom photocuring chamber (Quans, 400 nm, 1 mW/ cm^2) for 3 min. ELM constructs were cultured in appropriate liquid culture media and temperature according to the microbial strains present.

2.5.7 *Micro computed tomography (μCT) imaging of ELM constructs*

ELM constructs were cultured for in YPD prior to sampling for μCT imaging in which ELMs were cultured for 4 d, and 21 d for comparison. After culturing, samples were removed from culture media and washing with Dulbecco's phosphate-buffered saline (DPBS, 0.0009 M $CaCl_2$, 0.0027 M KCl, 0.005 M $MgCl_2.6H_2O$, 0.1368 M NaCl, 0.0152 M Na_2HPO_4). Washed constructs were cut into cubical slices with side lengths ~2 mm with a razor blade. Samples were mounted and allowed to sit overnight (~12 h before imaging). Samples were scanned with a Zeiss Versa 620 Scanner with the following scan parameters: Zeiss. 20X, 70kV, 8.5 W, 2 s acquisition time, detector 6.015 mm, source -10.119 mm, XYZ [-65, -19373, 469], camera bin 2, 180+fan, 1201views, no filter, dithering. Multi reference and secondary reference with LE1 filter. Reconstructed with center shift 3.224, beam hardening 0, theta 0, byte scaling [-0.1, 0.5], binning

1, recon filter smooth (kernel size = 0.7). Scans were reconstructed by Xradia Reconstructor with 0.85-micron voxels. Images were processed using ImageJ.

2.5.8 *Scanning Electron Microscopy (SEM) imaging of ELM constructs*

ELM constructs were cultured for 3 d prior to sampling for SEM analysis. After 3 d of culturing, constructs were removed from culture media and washed with Dulbecco's phosphate-buffered saline (DPBS, 0.0009 M $CaCl_2$, 0.0027 M KCl, 0.005 M $MgCl_2.6H_2O$, 0.1368 M NaCl, 0.0152 M Na_2HPO_4). Washed constructs were fixed with 8% glutaraldehyde (Sigma-Aldrich) solution for 48 h at room temperature. Cross-section samples were collected by cutting the samples 1.5 mm thickness after fixation. These samples were dried by stepwise ethanol dehydration with concentration range of 10, 20, 30, 40, 50, 60, 70, 80, 90 and 100 % were performed for 10 min in turn. Prior to SEM imaging, samples were coated with approximately 4 nm platinum by Leica EM ACE600 to maintain the conductivity. The Sirion XL30 scanning electron microscope was performed to image the microorganism in cross section area of ELM constructs. The SEM was operated at a high vacuum with an accelerating voltage of 15 kV.

2.5.9 *Betaxanthin production*

Thermo Labsystems Fluoroskan Ascent FL Fluorescence Microplate Reader was used to determine the continuous betaxanthin production capacity of ELM-SC-BXN constructs. After SLA 3D printing, cylinder-shaped ELM-SC-BXN constructs (x = 10.5 mm, y = 10.5 mm, z = 7 mm) were placed in 15 mL sterile culture tubes and cultured in 3 mL YPD media (10 g L^{-1} yeast extract, 20 g L^{-1} peptone and 20 g L^{-1} glucose) with 225 rpm at 30 °C for 5 days. In each day, samples were collected from cultured media, centrifuged at 4400 rpm for 10 min, supernatants were collected and placed in a microplate. Fluorescence intensity of samples were measured at

excitation: 485 nm / emission: 520 nm. ELM-SC-BXN constructs were washed with YPD and placed in new culture tubes and cultured in fresh YPD each day. Cylinder-shaped BSA-PEGDA constructs (x = 10.5 mm, y = 10.5 mm, z = 7 mm) were used as negative control and cylinder-shaped ELM-SC-WT constructs (x=10.5 mm, y = 10.5 mm, z = 7 mm) were used as positive control which were cultured in the same conditions for 5 d.

2.5.10 *L-DOPA production*

Cylinder-shaped ELM-EC-LDOPA constructs (x = 10.5 mm, y = 10.5 mm, z = 7 mm) were placed in 15 mL sterile culture tubes after 3D printing. 3 mL of LB media (50 μg mL^{-1} spectinomycin, 50 μg mL^{-1} kanamycin) were added and constructs were cultured in shaking incubator with 225 rpm, at 37 °C for 5 days. To monitor the continuous production of L-DOPA, 10 mM Vitamin C was added the culture media to eliminate the oxidation of L-DOPA. In each day samples were collected from cultured media, centrifuged at 4400 rpm for 10 min, filtered with 0.2-μm nylon syringe filters (Wheaton Science) then analyzed. Continuous L-DOPA production was determined by Bruker Esquire LC-Ion Trap Mass Spectrometer with Agilent HPLC. Mass spectrometer was operated in positive mode, scan range was between 50.00 m/z to 1100.00 m/z, skim1 was 15.0 volt and capillary exit was 55.0 volt. In HPLC analysis column oven was held at 25 °C with 1 % acetic acid in water or acetonitrile as the mobile phase over the course of the 20-min sequence under the following conditions: 5–15% organic (v/v) for 5 min, 15 to 100% organic (v/v) for 8 min, 100% organic (v/v) for 2 min, 100 to 5% organic for 2 min followed by 5% organic for 3 min. The constant flow rate was set at 0.2 mL min^{-1}. A standard curve was prepared using 98.0% purity L-DOPA (3,4-dihydroxy-L-phenylalanine) from Sigma-Aldrich. ELM-EC-LDOPA constructs were washed with LB, placed in new culture tubes, and cultured in fresh LB media (50 μg mL^{-1} spectinomycin, 50 μg mL^{-1} kanamycin, 10 mM Vitamin C) in each day. Cylinder-shaped

BSA-PEGDA constructs (x=10.5 mm, y=10.5 mm, z=7 mm) were used as negative control and cylinder-shaped ELM-EC-WT constructs (x=10.5 mm, y=10.5 mm, z=7 mm) were used as positive control which were cultured in the same conditions for 5 days.

2.5.11 *Naringenin production*

Cylinder-shaped ELM-EC-NGN constructs (x=10.5 mm, y=10.5 mm, z=7 mm) constructs were placed in 15 mL sterile culture tubes after 3D printing. 3mL of LB media (30 μg mL^{-1} chloramphenicol, 100 μg mL^{-1} ampicillin, 50 μg mL^{-1} spectinomycin and 50 μg mL^{-1} kanamycin) were added and constructs were cultured in a shaking incubator with 225 rpm, at 30 °C for 5 days. In each day samples were collected from cultured media, centrifuged at 4400 rpm for 10 min, filtered with 0.2-μm nylon syringe filters (Wheaton Science). Filtered samples were mixed with 100% ethanol (1:1 v/v) to dissolve the naringenin. Ethanol treated samples were analyzed in Bruker Esquire LC - Ion Trap Mass Spectrometer with Agilent HPLC. Mass spectrometer was operated in positive mode, scan range was between 50.00 m/z to 1100.00 m/z, skim1 was 15.0 volt and capillary exit was 55.0 volt. To identify naringenin in HPLC, same parameters were used that are described in the L-DOPA production section. A standard curve was prepared using ≥ 95% purity naringenin ((±) - 2, 3 – Dihydro - 5, 7 – dihydroxy – 2 - (4 - hydroxyphenyl) - 4H – 1 – benzopyran – 4 - one, 4′, 5, 7 -Trihydroxyflavanone) from Sigma-Aldrich. ELM-EC-NGN constructs were washed with LB, placed in new culture tubes, and cultured in fresh LB media (30 μg mL^{-1} chloramphenicol, 100 μg mL^{-1} ampicillin, 50 μg mL^{-1} spectinomycin and 50 μg mL^{-1} kanamycin) in each day. Cylinder-shaped BSA-PEGDA constructs (x = 10.5 mm, y = 10.5 mm, z = 7 mm) were used as negative control and cylinder-shaped ELM-EC-WT constructs (x = 10.5 mm, y = 10.5 mm, z = 7 mm) were used as positive control which were cultured in the same conditions for 5 days.

2.5.12 *Degree of swelling (q) and Mechanical Characterization*

Cylindrical shaped ELM constructs (x = 10.5 mm, y = 10.5 mm, z = 7 mm) were cultured for 5 d in the appropriate liquid culture media and conditions according to the microbial strain that they have. Constructions were removed from culture media after culturing and vacuum-dried overnight. Dried constructs were rehydrated in DI water overnight. Degree of swelling was calculated according to following equation (Equation 2.1):

$$q = \frac{Rehydrated\ volume - Dried\ volume}{Dried\ volume} \quad (2.1)$$

These cultured, dried, and rehydrated samples were subjected to the compression test. For compression test, Newton Test Machine electromechanical test frame with 1 kN load cells and crosshead rates of 1.3 mm/min was used. The compressive modulus was calculated by the slope of the stress (kPa)- strain(mm/mm) curve. We formulated three control groups to examine the effects of *in-situ* L-DOPA production on mechanical properties of BSA-PEGDA networks. BSA-PEGDA constructs (without cell) were used as a negative control. ELM-EC-WT was studied to understand the effect of metabolic activity of incorporated cells on the BSA-PEGDA network. Finally, we treated the BSA-PEGDA constructs with the commercially available standard of L-DOPA (positive control-2) to compare the effect of L-DOPA production within the BSA-PEGDA network with the effect of providing this compound externally. To do that, 3D printed BSA-PEGDA constructs were treated with 200 mg/ml L-DOPA solution which is the amount that was produced from ELM-EC-LDOPA constructs after 5 d culturing (Figure 3b). All control samples were printed in cylinder-shape (x = 10.5 mm, y = 10.5 mm, z = 7 mm).

2.5.13 *Biodegradation of ELM constructs*

Biodegradation of ELM constructs were followed by measuring the wet mass over time. The structural changes of constructs were determined by taking pictures of samples over time.

2.5.14 *UV-vis Absorption and CD-Spectroscopy*

Varian Cary 5000 UV-Vis-NIR Spectrophotometer was used to measure UV-vis spectroscopy in a quartz cuvette at room temperature. Circular dichroism (CD) spectroscopy was carried out on a Jasco 720 Circular Dichroism Spectrophotometer by using a quartz cell of path length 0.1 cm. To understand the effect of bioactive compounds produced from metabolically engineered cells on the BSA-PEGDA network, possible interactions between bioactive components and BSA were evaluated with UV-absorbance measurements. 100 mg/ml NGN stock solution was prepared in ethanol and diluted in water to 0.5 mg/ml. BSA+NGN sample contained 0.5 mg/ml for each component and prepared in DI water. 0.01 mM of ProK, 0.01 mM L-DOPA, and 0.01 mM NGN were prepared for CD spectroscopy analysis.

2.5.15 *Statistical analyses*

To compare the statistical difference Igor Pro (Version 8.04) software was used. Differences were analyzed by One-way ANOVA, Welch Test. p value of < 0.05 was chosen to determine significant differences. The standard deviations (± S.D.) of replicates were calculated in Excel.

CHAPTER 3. GENETICALLY PROGRAMMED ENGINEERED LIVING MATERIALS AS HIGH-PERFORMANCE BIOPLASTICS

3.1 ABSTRACT

Engineered Living Materials (ELMs) are artificial living systems wherein genetically modified microorganisms are encapsulated into a polymer network, forming functional objects with unique material properties. Despite the potential for ELMs, there are limited means to fabricate ELM bioplastic materials with arbitrary 3D shapes and requisite physical properties for mechanical performance. Herein, we showcase how mechanical stiffness and proteolytic degradation of protein-based ELMs can be tuned through programmed bioproduction. Using genetically engineered *S. cerevisiae* strains, it is possible to enable the production of betaxanthins and proteinase A in response to copper ions and galactose, respectively. This programmed bioproduction enables bio-augmentation of the mechanical properties of the bioplastic during the manufacturing process, as well as its end-of-use bio-degradation. Specifically, the betaxanthins served to enhance the modulus of the bioplastic materials and also to reduce the degradative activity of native proteolytic enzymes of *S. cerevisiae*, whereas proteinase A was produced for the rapid on-demand degradation of the ELM bioplastic. This bio-manufacturing approach provides the means to fabricate ELMs with arbitrary 3D shapes and bio-augmented mechanical properties that can also address demands for sustainability.

3.2 INTRODUCTION

The synergy of synthetic biology and materials science yields innovative strategies for fostering environmental sustainability and improved functionality. Among these approaches, engineered living materials (ELMs) stand out as a promising platform. ELMs are a distinctive class of smart materials that result from the integration of synthetic or non-synthetic living cells into a polymer network. Recent studies highlight ELMs as alternative bioproduction platforms for chemical[1] and energy[11-13] production. Besides bioproduction capabilities, ELMs can also be designed for self-healing[17,93], shape-morphing[38], or bio-augmented stiffness[5,94]. Despite the future potential of ELMs in areas like smart packaging, textiles, soft robotics, and biosensor devices, a persistent challenge lies in the design and manufacturing of ELM bioplastics that can address the future needs for sustainability and chemical circularity.

Synthetic polymers and biopolymers are susceptible to acid- and base-catalyzed hydrolysis, particularly when the polymers possess ester or amide bonds[95] , and non-enzymatic hydrolysis can be a slow process to achieve complete degradation[96]. Synthetic strategies have also been used to develop polymer networks that can be easily degraded via thiol-ester exchange or contain nano-dispersed embedded enzymes that catalyze degradation during the recycling process[96,97]. Biopolymer-based plastics (i.e., formed from proteins, cellulose, etc.) are more easily degraded than their petroleum-based counterparts, but still require external inputs such as heat or enzymes to degrade[16–18]. We previously reported two different biodegradable protein-based resin formulations, namely methacrylated bovine serum albumin (MABSA)[19] and poly(ethylene glycol)diacrylate modified bovine serum albumin (BSA-PEGDA)[20,21] , for use as resins for vat photopolymerization. 3D printed samples from these formulations exhibited plastic behavior when dried, making them promising candidates for bioplastic applications.

ELMs that utilize a native or easily bio-mimicked biological extracellular matrices such as polysaccharides and proteins can utilize natural enzymes for the degradation of the matrices at the end of its life cycle of utility. While biodegradability is a benefit of biopolymer-based ELMs, temporal control over when the biodegradation takes place presents a barrier for the implementation of such materials, especially in the built environment. During the lifetime of an ELM material, the native proteases and esterases of the encapsulated microorganisms can degrade the extracellular matrix, except in instances of heated and cell-deactivated ELMs, which effects the performance of these materials while in use[9,22]. Ideally, these enzymes should not affect the degradation of the ELM until the end of its life cycle of utility.

ELM hydrogels can utilize metabolic products from engineered microorganisms to bio-augment the mechanical properties of the hydrogel matrix[9]. For instance, L-DOPA production within BSA-PEGDA ELMs improved the stiffness of the hydrogel matrix, while betaxanthins production significantly reduced the rate of enzymatic degradation. Additionally, we reported input-responsive ELMs using genetically modified *S. cerevisiae* with multiple gene circuits wherein the cells produced betaxanthins or proteinase A in response to copper ions or galactose, respectively[2]. This approach showcased a method for temporal control over dynamic gene expression, as well as the long-term genetic expression capabilities of these systems in continuous cultures.

Herein, we demonstrate the additive manufacturing of ELMs that utilize inducible gene production to program the ELM's stiffness and temporal control of degradation (**Figure 3.1**). The 3D printed ELMs comprised BSA-PEGDA polymer matrices that encapsulated *S. cerevisiae* cells genetically engineered for the inducible production of betaxanthins or proteinase A. The betaxanthins served to enhance the modulus of the bioplastic materials and also to reduce the

degradative activity by native proteolytic enzymes of *S. cerevisiae*, while proteinase A was produced for the rapid on-demand degradation of the ELM bioplastic. Thus, the manufacturing and end-of-use degradation of these mechanically functional bioplastic ELMs are genetically programmed. To highlight the practical utility of these ELM compositions, a functional wall hook was fabricated and kept in operation for 60 days, after which time the preserved microorganisms were induced to produce proteinase A for the degradation of the material. Thus, this approach demonstrates an advanced biomanufacturing scheme that utilizes additive manufacturing and genetic control to produce high-performance bioplastics.

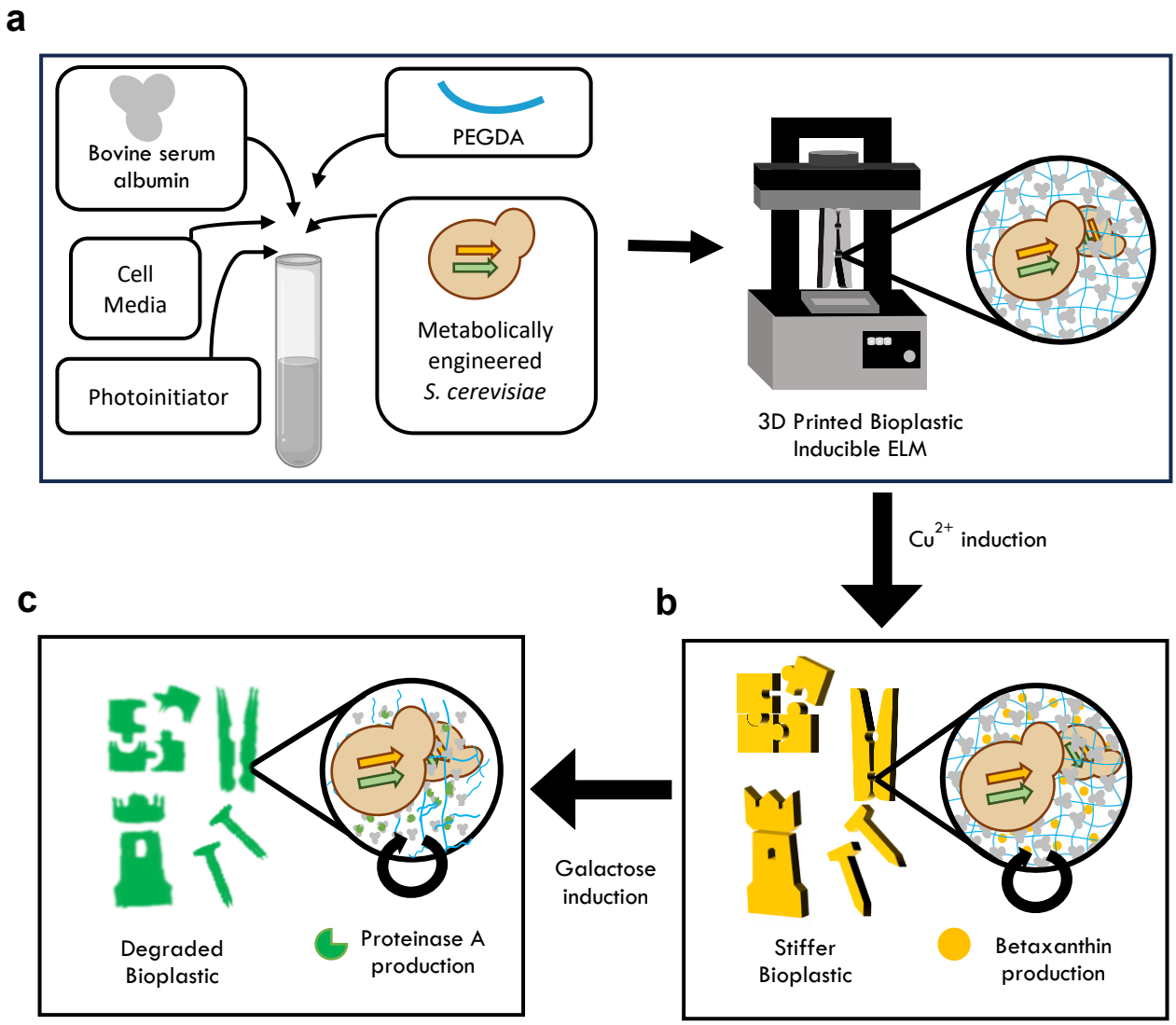

Figure 3.1. Schematic representation of biomanufacturing of inducible ELM. a) Protein-based bio-resin as feedstock for genetically programmed bioaugmented manufacturing. b) ELM differentiates into a stiffer material with the Cu^{2+} inducer to allow for use and reuse of bioplastic construct. c) ELM differentiates into degradable ELM with the galactose inducer for genetically programmed biodegradation.

3.3 RESULT AND DISCUSION

3.3.1 *Multi - input genetic programs in S. cerevisiae ELMs*

This section of Chapter 3 is adapted with permission from Sugianto, W., Altin-Yavuzarslan, G., Tickman, B. I., Kiattisewee, C., Yuan, S. F., Brooks, S. M., Wong, J., Alper, H. S., Nelson, A. & Carothers, J. M. Gene expression dynamics in input-responsive engineered living materials programmed for bioproduction. *Materials Today Bio, 20*, 100677. Copyright 2023, Elsevier, Online Library.

Yeast hydrogel-based ELMs using bovine serum albumin (BSA) - polyethylene glycol diacrylate (PEGDA) bioconjugates to encapsulate *S. cerevisiae* spk05 cells were fabricated by SLA 3D printing (**Figure 3.2**). The *S. cerevisiae* cells were programmed to express two different proteins, each under the control of a different inducible promoter. Expression of secreted proteinase A enzyme from the scPEP4 gene was placed under the control of a galactose-inducible promoter. Copper (II)-inducible expression of a dioxygenase enzyme (mjDOD gene) combined with constitutively expressed P450 enzyme (CYP76AD5 gene) catalyzes the production of secreted betaxanthin pigment molecules (**Figure 3.2 b**). With this design, inducers can be selectively added or withdrawn from the media to schedule increases or decreases, respectively, in production of the target molecules (**Figures 3.2 c, d - top**). In the experiments that follow, the relative production levels of proteinase A and betaxanthins were monitored over the course of 27 days under continuous cultivation (**Figures 3.2 c, d - bottom**). Two different dynamic induction cycles were performed, each consisting of three phases: Phase 1 = 7 days, Phase 2 = 8 days, and Phase 3 = 12 days. In the first dynamic induction cycle, copper (II) was added in the first phase, withdrawn and replaced with galactose in the second phase, and added again in the third phase while galactose was withdrawn (**Figure 3.2 c**). The second dynamic induction cycle was carried out in a similar manner, where galactose was added in the first phase, replaced with copper (II) in the second phase, and then re-added to the third phase where copper (II) was withdrawn (**Figure**

3.2 d). In the first induction cycle, galactose-induced proteinase A production in Phase 2 was 1.5-2.1 fold higher than the levels measured in the absence of galactose (Phases 1 and 3) (**Figure 3.2 c, bottom**). The production of betaxanthins in Phase 3, induced with the addition of copper (II) on the 15th day of the experiment, reached 84% of the maximum level of induced betaxanthins production observed in Phase 1. In the second induction cycle, relatively large differences in proteinase A production were observed, and 65% of the maximum Phase 1 expression was also achieved by Day 27 in Phase 3 (**Figure 3.2 d, bottom**). The transitions between the phases for betaxanthins production were less distinct in the second induction cycle compared to the first induction cycle. Nonetheless, clear variations in the levels of measured betaxanthins could be seen at the endpoints of the phases. Thus, as with the *E. coli* ELMs, the *S. cerevisiae* ELMs retain the capacity to express multiple genes in multi-week continuous cultures. Moreover, these results constitute a proof-of-concept demonstration that multi-input, multi-output gene expression programs can be implemented in ELMs to permit switching between multiple bioproducts.

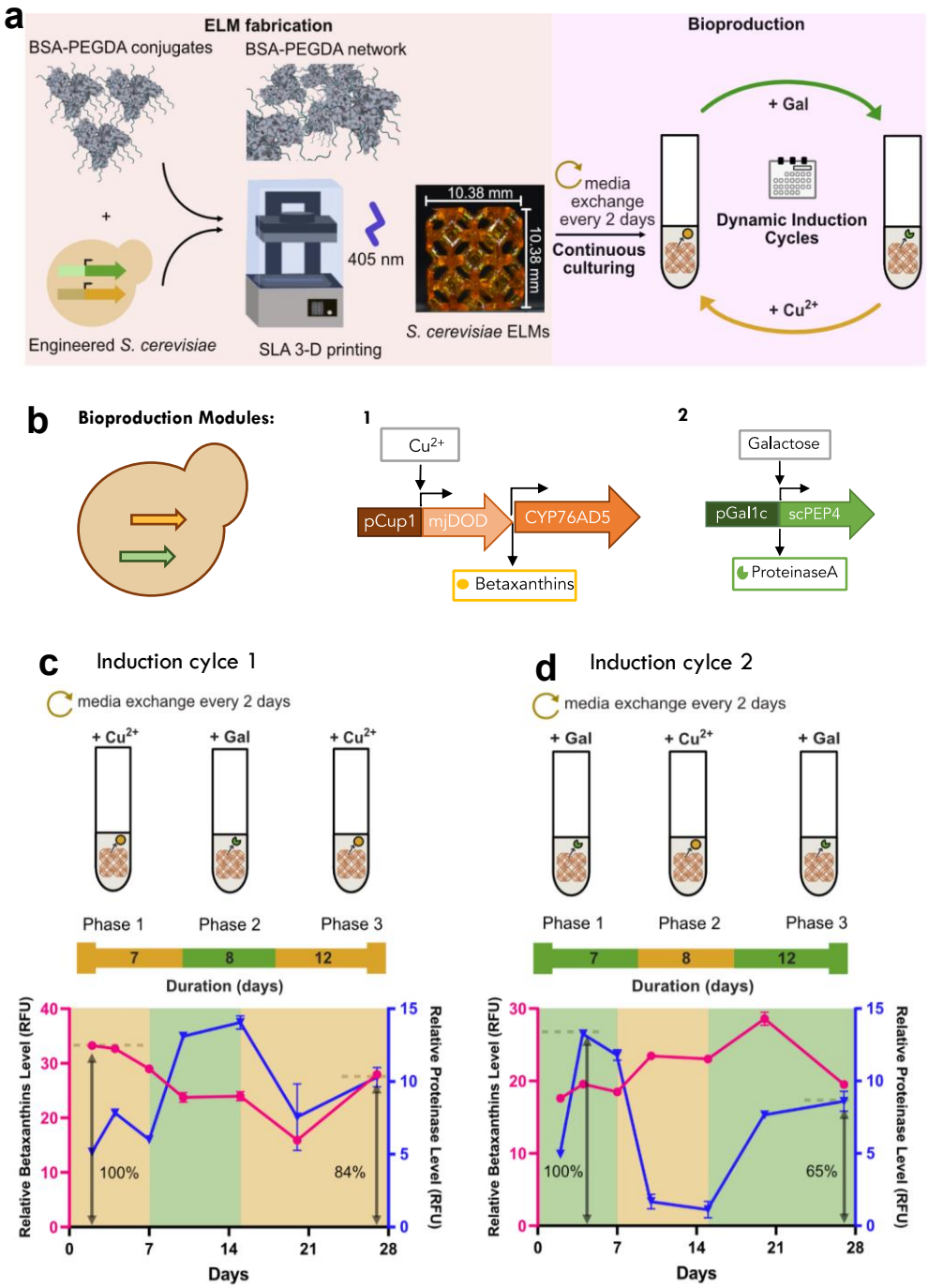

Figure 3.2. Dynamic inducible bioproduction in *S. cerevisiae* ELMs a) These ELMs are fabricated by seeding BSA-PEGDA hydrogels with engineered *S. cerevisiae*. The ELMs are printed using a SLA 3-D printer and continuously cultured with media exchange every 2 days. For scheduled bioproduction, ELMs were dynamically induced to control expression of native and heterologous enzymes. b) Multi-input genetic programs in *S. cerevisiae* ELMs for multi-product biosynthesis: 1) Cu^{2+}-inducible expression of dioxygenase enzyme with constitutive expression of P450 enzyme for betaxanthins production, and 2) galactose-inducible expression of secreted proteinase A enzyme c) Induction cycle 1 consists of 3 phases (Phase 1 = 7 days, Phase 2 = 8 days, Phase 3 = 12 days). Top: Alternating induction by selective addition of Cu^{2+} inducer (orange) in Phases 1 and 3, and galactose inducer (green) in Phase 2. Bottom: Time-dependent betaxanthins and proteinase A production levels. d) Bioproduction Induction cycle 2 with 3 phases (phase lengths are identical to c). Top: Alternating induction by selective addition of galactose inducer (green) in Phases 1 and 3, and Cu^{2+} inducer in Phase 2. Bottom: Time-dependent betaxanthins and proteinase A production levels. Values represent the mean ± standard deviation from n = 3 technical replicates.

3.3.2 *Effects of inducible bioproduction on polymer network*

Inducible ELM constructs were fabricated by genetically engineered *S. cerevisiae* which has multi-input genetic programs (**Figure 3.2 b**). This microorganism was engineered to produce different products namely betaxanthin and Proteinase A with the presence of different inducers, Cu^{2+} and galactose, respectively. By using BSA-PEGDA bioconjugates and genetically engineered *S. Cerevisiae*, SLA 3D printed ELM constructs in cylindrical shape (x =10.5 mm, y = 10.5 mm, z = 7 mm) were fabricated and performed their inducible bioproduction capacity over 15 days by culturing them with different inducers.

In the presence of the Cu^{2+} inducer, ELM constructs consistently produced betaxanthins (**Figure 3.3 a**), while a continuous production of Proteinase A was sustained by culturing the construct in media containing galactose inducer (**Figure 3.3 b**). Upon introduction of both Cu^{2+} and galactose inducers into the culture media, the ELMs exhibited simultaneous production of both betaxanthins and proteinase A. However, the quantity of product detected was lower when both betaxanthins and proteinase A were produced concurrently, in comparison to the product obtained under single inducer conditions (**Figures 3.3 a, b**). Notably, a limited production was observed when ELMs were cultured in basal media devoid of inducers (**Figures 3.3 a, b**).

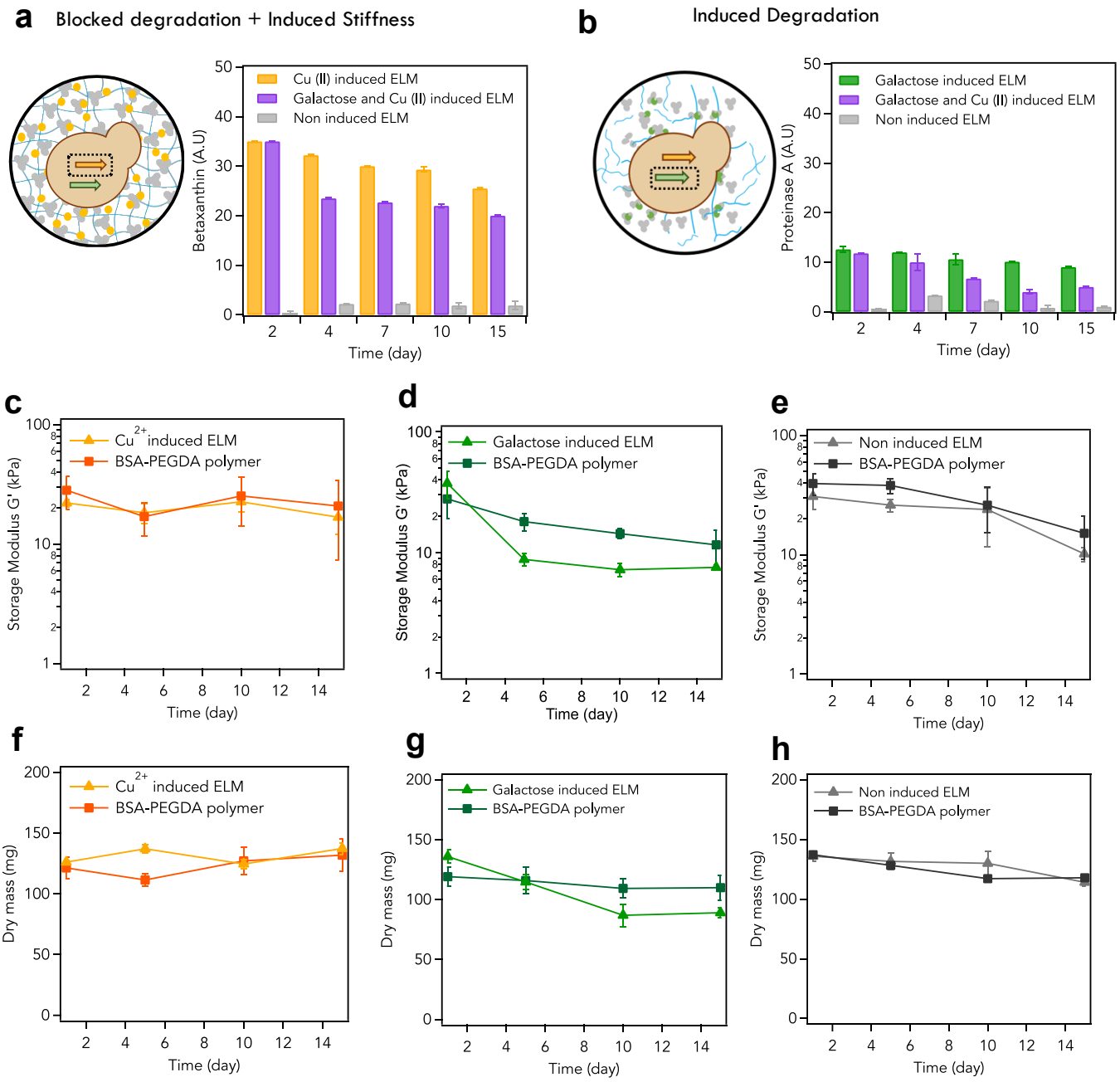

Figure 3.3. Inducible bioproduction and effects on mechanical properties of ELM. a) Betaxanthins bioproduction with Cu^{2+} inducer over 15 days. b) Proteinase A bioproduction with galactose inducer over 15 days. c-d) Change of storage modulus (G') over time by betaxanthins production with the presence of Cu^{2+} inducer and by proteinase A production with the presence of galactose inducer, respectively. e) Change of storage modulus (G') over time without genetically induced metabolite production. f-g) Dry mass change over 15 days with inducible bioproduction of betaxanthins and proteinase A, respectively. h) Dry mass change of ELM without inducible bioproduction. Control group (acellular BSA-PEGDA) was cultured with the same inducing conditions as ELM samples.

Rheometric characterization techniques are commonly used for synthetic polymeric materials to understand network properties, degradation, and viscoelastic characteristics[96], which is reflected in the storage and loss moduli of the material[103]. Here, we used the direct relationship between the plateau storage modulus (G′) of a polymer network and its crosslinking density (Equation S1)[103] to investigate the effects of inducible bioproduction on the ELM matrices (**Figures 3.3 c-e**). We prepared samples by photocuring disks (x = 20 mm, y = 20 mm, z = 1 mm) at 405 nm to match the dimensions of the parallel plate geometry. Additionally, the dry mass loss over time for each of these samples was also measured (**Figures 3.3 f-h**). We quantified these changes over the course of 15 days in response to induced expression of betaxanthins or proteinase A. To understand the extent of degradation due to hydrolysis of peptide and ester bonds in the BSA-PEGDA network, control samples without cells – the acellular BSA-PEGDA matrix – were subjected to the same culturing conditions as the inducible ELMs.

Our rheological investigations show that Cu^{2+}-induced production of betaxanthins significantly retarded the microbial degradation of BSA-PEGDA ELMs, which is consistent with our previous report[5] using *S. cerevisiae* for the constitutive production of betaxanthins. The continuous Cu^{2+}-induced production of betaxanthins over the 15-day period had a negligible effect on the storage modulus of the ELM matrix compared to the acellular BSA-PEGDA matrix (**Figure 3.3 c**), as the G′ values for both matrices were similar throughout the experiment. Thus, there was no significant difference between the BSA-PEGDA sample incubated in Cu^{2+} media and the Cu^{2+}-induced ELM on day 15 ($p=0.4479$). In addition, there was no significant difference among the G′ of the Cu^{2+}-induced ELM sample ($p=0.8834$) from days 1 to 15. We also observed minimal changes to the dry mass over this period of time, which is consistent with the rheological results (**Figure 3.3 f**). These results show that betaxanthins do not affect the mechanical properties of

these water-swollen ELM networks, and that the mechanical properties do not change despite the constitutive production of proteolytic enzymes by the cells. Betaxanthins has previously been reported to retard microbial degradation of BSA-PEGDA ELMs by interacting with the BSA and altering its secondary structure[5]. In contrast, the control experiments on non-induced ELMs shows a decrease in the G′ values over time (**Figure 3.3 e**) with a concomitant decrease in the dry mass over the same period (**Figure 3.3 h**). Thus, in the absence of betaxanthins, the endogenously expressed proteolytic enzymes are capable of degrading the network slowly over time.

To facilitate the rapid degradation of the BSA-PEGDA ELM, galactose can be used to induce the production of proteinase A by the engineered microbes. Rheometric characterization showed a significant difference in the G′ of galactose-induced BSA-PEGDA ELMs versus the acellular BSA-PEGDA matrix (**Figure 3.3 d**) over time. The acellular BSA-PEGDA matrix in media containing galactose had a G′ of 27.8 ± 8.6 kPa on day 1 that decreased to 11.6 ± 4.4 kPa (*p=0.0567*) after 15 days. For the galactose-inducible ELMs, there was a more significant decrease in the G′ from 37.5 kPa ± 9.6 kPa on day 1 to 7.5 kPA ± 0.3 kPa on day 15 (*p=0.0276*). Overall, the fastest rate of decrease was observed for the galactose-induced ELMs (0.0458 kPa/day), which was over 6 times the magnitude of the degradation rate for Cu^{2+}-induced ELMs. These results are supported by the extensive dry mass loss for galactose-induced ELMs that decreased from 135.9 ± 6.7 mg to 89.0 ± 5.4 mg after 15 days (**Figure 3.3 g**) which show that genetic programming provides a viable strategy for on-demand degradation of BSA-PEGDA ELM matrices induced by the presence of galactose. Moreover, these changes can be monitored rheometrically over time.

Many proteases are known to have a higher activity in lower pH environments[103], therefore, we investigated the cell viability and degradation rate of galactose-induced ELMs in more acidic media (pH 4). Live/dead stains were used to evaluate the cell viability at pH 7 and pH 4 (**Figures**

3.4 a, and **3.4 b**, respectively). While the cell viability decreased from 99% at pH 7 to 79% at pH 4 (**Figure 3.4 c**), we observed a net increase in the proteinase A activity between these conditions (**Figure 3.4 d**). Concurrently, a notable decrease in both G' and dry mass was observed in samples cultured for 15 days in galactose containing media at pH 4.

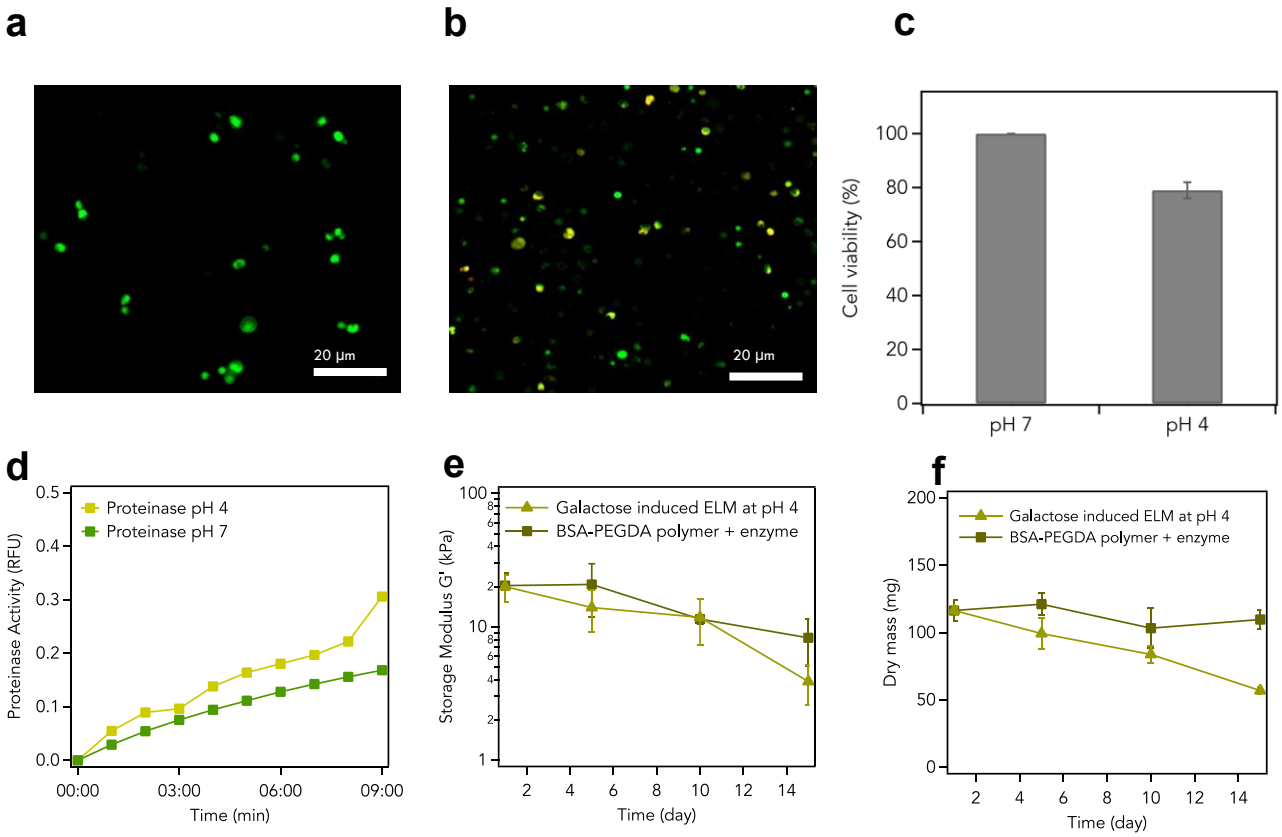

Figure 3.4. The performance of galactose induced ELM at pH 4. a-c) Cytotoxicity evaluation of inducible *S. cerevisiae* (spK05) in different pH conditions. a) *S. cerevisiae* (spK05) cells incubated at pH 7. b) *S. cerevisiae* (spK05) cells incubated at pH 4. Live cells represented in green and dead cells represented in orange - yellow. c) Live and dead cell ratio of *S. cerevisiae* (spK05) cells at pH 7 and pH 4. d) Proteinase A activity in pH 7 and pH 4 environments. e) Effect of Proteinase A bioproduction on storage modulus at pH 4 over 15 days. f) dry mass change (%) of galactose induced ELM at pH 4 over 15 days. BSA-PEGDA polymer exogenously treated with pepsin was used as a control group.

Specifically, the G' of galactose-induced ELM cultured at pH 4 (3.9 ± 1.3 kPa) was lower than at pH 7 (13.1 ± 4 kPa) after 15 days ($p = 0.0162$). The extent of mass change of galactose-induced ELMs is also notably higher under more acidic conditions (**Figures 3.3 g, and 3.4 f**). To ensure that the pH of the media did not have an effect on the BSA-PEGDA network, we incubated the acellular BSA-PEGDA samples in galactose-containing media at pH 4 (**Figure 3.5**). After 15 days of incubation, the G' slightly decreased from 34.0 ± 21.3 kPa to 30.9 ± 3.8 kPa ($p = 0.5993$).

One advantageous feature of cell-laden ELMs is their *in situ* production of proteolytic enzymes that are more effective than the exogenous addition of enzymes for biodegradation. To demonstrate this, we compared the continuous production of proteinase A (a pepsin-like aspartic proteinase[103]) within an ELM to an acellular BSA-PEGDA sample incubated with pepsin (500 U/mL). Interestingly, the treated acellular BSA-PEGDA matrices at pH 4 and 7 exhibited minimal mass reduction. In contrast, the galactose-induced ELMs with *in situ* production of the protease showed a mass loss of 51.3 ± 2.6 % and 34.5 ± 4.0 % at pH 4 and 7, respectively.

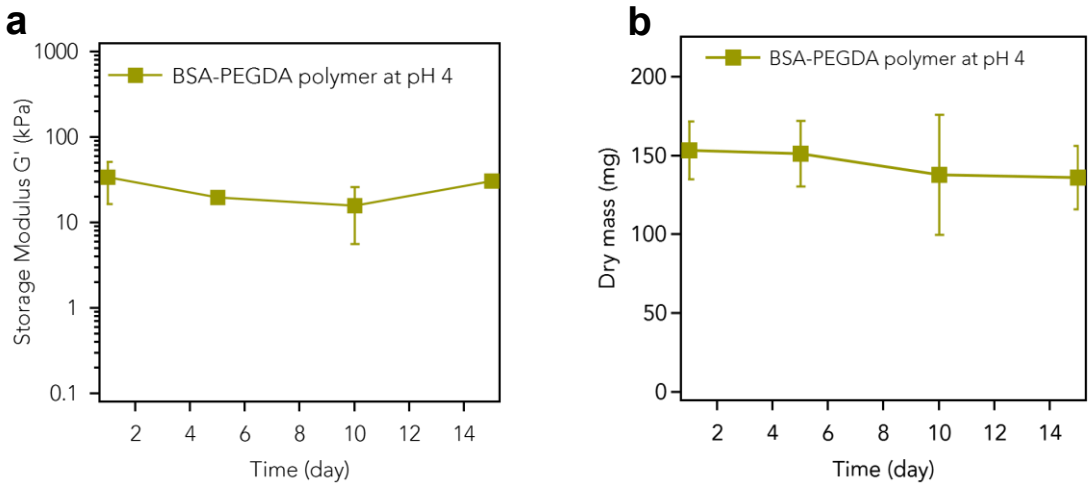

Figure 3.5. Storage modulus and dry mass change in BSA-PEGDA polymer at pH 4 over 15 days. a) Storage modulus at pH 4 over 15 days. b) Dry mass change of samples over 15 days.

3.3.3 *Additive Manufacturing of Inducible ELMs*

We next investigated the additive manufacturing of BSA-PEGDA ELMs and inducible bioproduction within the 3D printed ELM hydrogels. Vat photopolymerization with a stereolithographic apparatus (SLA) 3D printer was used to fabricate the lattice constructs shown in **Figure 3.6 a**. These constructs were submersed in media that contained Cu^{2+} for betaxanthins production, galactose for proteinase A production, or both inducers for simultaneous production of betaxanthins and galactose. After 30 days of culturing, the Cu^{2+}-induced ELM decreased in size, but in general, maintained its initial lattice shape. In contrast the lattice construct induced by galactose broke apart into smaller fragments due to degradation of the network by proteinase A. Simultaneous induction with both inducers demonstrated a better shape integrity compared to the galactose-induced ELM but exhibited slightly less stability than the Cu^{2+}-induced ELM. To investigate the changes in material properties via inducible metabolite production, we assessed the compressive modulus of induced ELM. To investigate the changes in material properties via inducible metabolite production, we assessed the compressive modulus of induced ELM samples following a 30-day culture with the different inducers. The ELM samples were 3D printed in a cylindrical disk shape (x = 10.5 mm, y = 10.5 mm, z = 7 mm) and cultured under four conditions: culture media without any inducing agent, culture media with galactose, culture media with Cu^{2+}, and culture media with both galactose and Cu^{2+}. The compressive moduli for these ELM hydrogels were 357 ± 30 kPa, 248 ± 20 kPa, 415 ± 18 kPa, and 328 ± 10 kPa, respectively (Figure 4B). These results were consistent with the mass changes expected in the presence of betaxanthins or proteinase A (**Figure 3.6 c**). CD spectroscopic analysis suggests that betaxanthins can interact with proteins such as BSA[5] and proteinase A (**Figure 3.6 d**) to disrupt their secondary and tertiary

conformations. These interactions can have consequences for the mechanical properties and degradation rates of the BSA-PEGDA matrix.

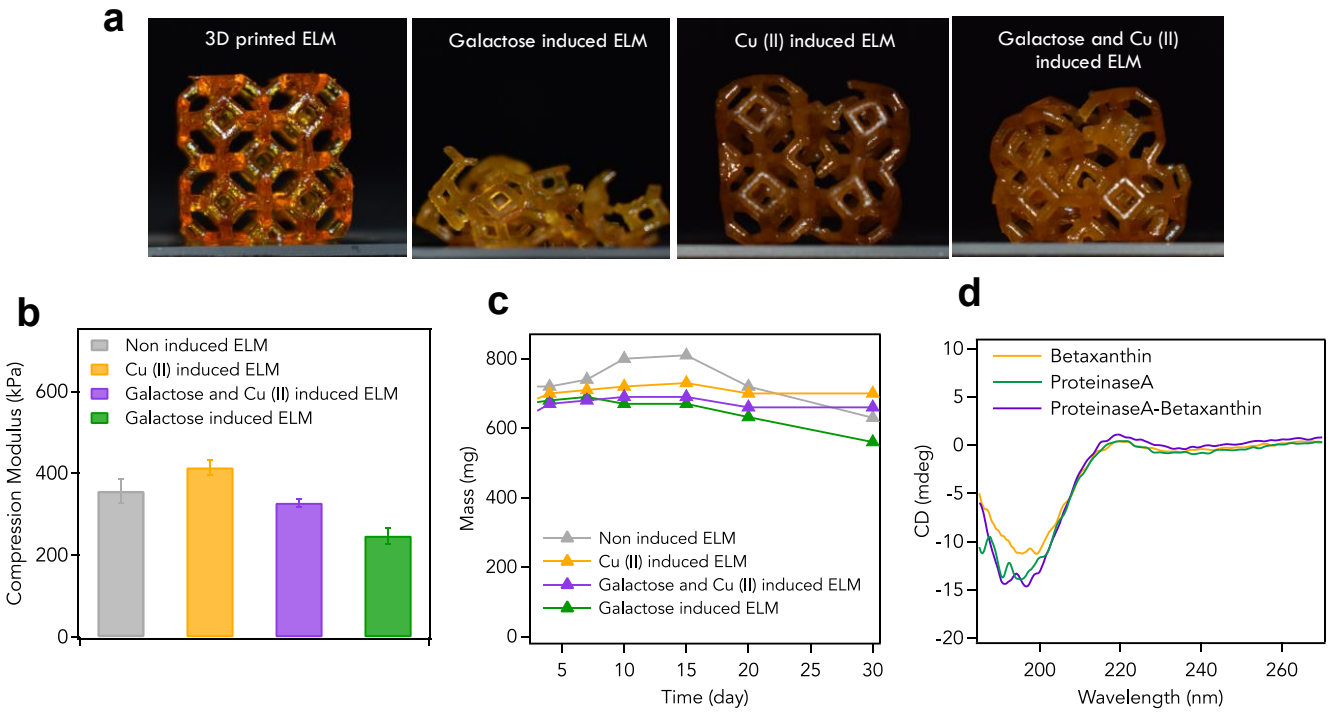

Figure 3.6. Changes in material properties by long-term inducible bioproduction of ELMs (30 days). a) optical images of 3D printed ELM in lattice forms which were cultured with different inducers to produce different products for 30 days. b) uniaxial compression experiments were performed to obtain the compressive moduli of inducible ELMs which were cultured in 30 days; Cu^{2+} induced ELM for betaxanthin production, galactose induced ELM for proteinase A production, Cu^{2+} and galactose production for both betaxanthin and proteinase A production, non-induced ELM cultured in inducer free media as control group. c) Mass changes of samples over 30 days. d) CD spectra of Proteinase A, betaxanthin and Proteinase A-Betaxanthin at pH 7.

3.3.4 *Sequential induction of genetic expression within the ELM matrix*

In a scheme for bio-augmented manufacturing of ELMs as high-performance materials, the as-printed constructs must first undergo the bio-enhancing step prior to the end-of-use biodegradation. Once it had established that the inducible expression of betaxanthin and Proteinase A changes the mechanical properties of the BSA-PEGDA polymer matrix (**Figure 3.6**, **Figure 3.7**), it was investigated if the inducers could be changed in series to allow for programmable use and degradation of material (**Figure 3.7**). For this aim, storage modulus (G') and dry mass of the

materials were monitored over 3 different phases using the same rheological methods employed in **Figure 3.3.**

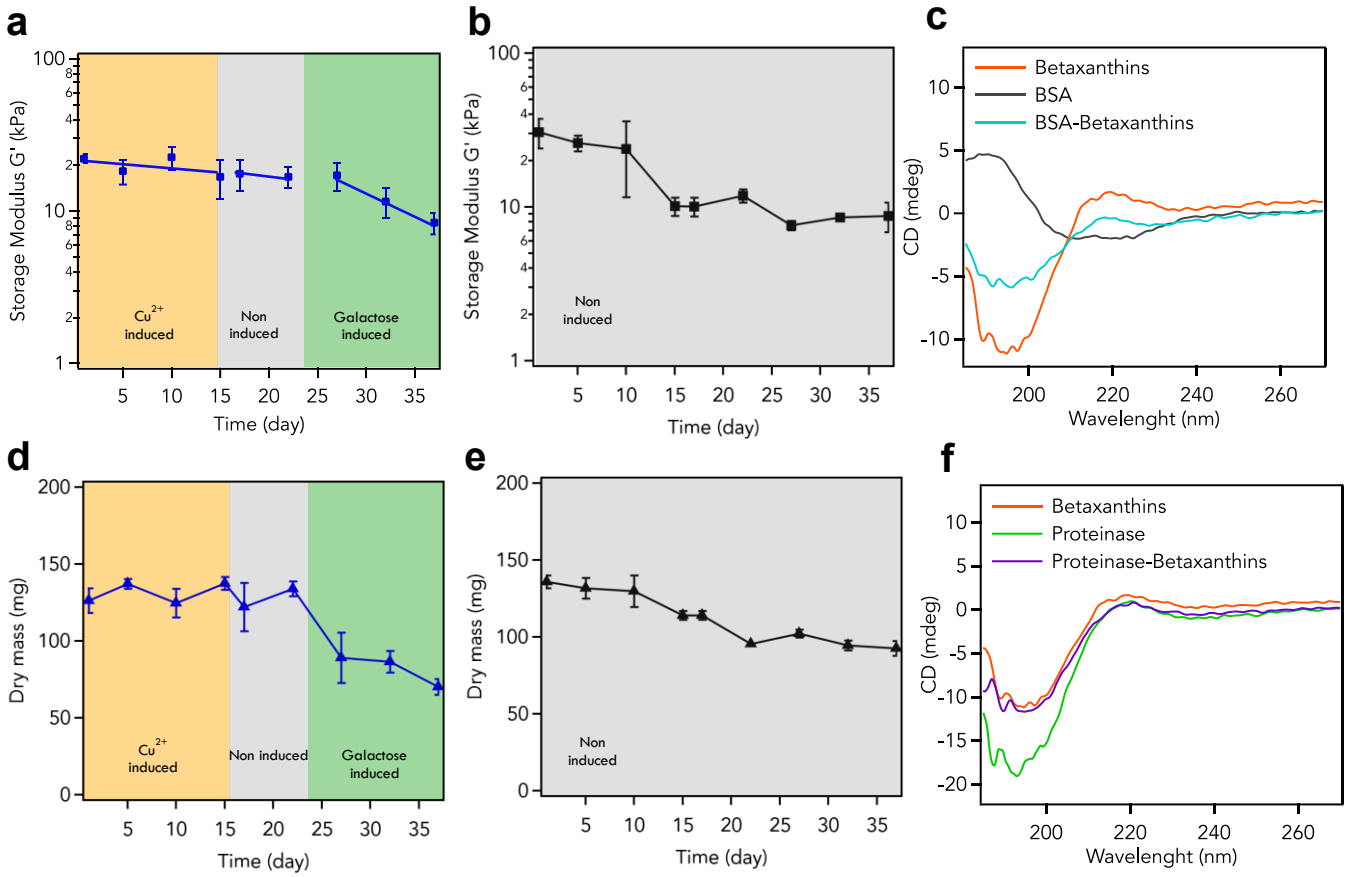

Figure 3.7. Effects of long-term switchable inducible bioproduction on ELM polymer network. Inducible ELM samples cultured in the following phases: Betaxanthins bioproduction with Cu^{2+} inducer media over 15 days, inducer free media for 7 days, proteinase A bioproduction with galactose inducer media at pH 4 for 15 days. a) Change of storage modulus (G') over inducible bioproduction. b) Change of storage modulus (G') in inducer free culturing. c) CD spectroscopy of BSA and betaxanthins and BSA-Betaxanthins complex at pH 4. d) Change of dry mass over inducible bioproduction. e) Change of dry mass in inducer free culturing. f) CD spectroscopy of proteinase A and betaxanthins and proteinase A-Betaxanthins complex at pH 4.

Phase 1 (15 days, days 1-15) was designed to allow for sustained use of the material without degradation via production of betaxanthin from Cu^{2+} induction. Phase 2 (7 days, days 16-22) was designed as switching period in inducer free media to remove Cu^{2+} from the media and cease betaxanthin production. Phase 3 (15 days, days 23-37) was designed to sustainably degrade the ELM based on the most effective degradation system, galactose-containing media at pH 4 induced

for Proteinase A production. Control ELM samples were cultured in inducer free media for the same length of time as a comparison. When assessing degradation rates, the correlation between storage modulus and time for each phase was examined, aiming to comprehend the degradation kinetics. This involved analyzing the slopes of linear graphs.

In phase one that ELM samples cultured in Cu^{2+} inducer media m found that -0.006. The G' of Cu^{2+} induced ELM changed as follows 22.1 ± 1.5 kPa, 18.3 ± 3.4 kPa, 22.6 ± 3.4 kPa, 16.8 ± 4.8 kPa in day 1, 5, 10 and 15, respectively. Upon switching Cu^{2+} containing media to inducer free media, G' modulus remained fairly constant at day 17 where G' was 17.6 ± 4 kPa and 16.8 ± 2.7 at day 22. This may be due to betaxanthin remaining bound to the BSA molecules in the polymer matrix and prevent hydrolysis even in the absence of betaxanthin bioproduction. Switching into Phase 3 and inducing the ELM with galactose at pH 4 resulted in higher reduction of G' over time and m was calculated -0.03. After 10 days Proteinase A bioproduction, G' of ELMs reduced to 11.6 ± 2.6 kPa and it continued to reduce to 8.4 ± 1.4 kPa at day 37. By comparing the slope of the linear graphs of different phases, it was found that the rate of degradation in Phase 3 was 5-fold faster than in Phase 1 (**Figure 3.7 a**) For the control ELM samples which were incubated in inducer free media, it was observed a faster change in terms of G' over 15 days, and m of this period was found that -0.03 (**Figure 3.7 b**), which the results compatible with **Figure 3.3 f**. This reduction may be attributed to the metabolic activity of embedded *S. cerevisiae* cells rather than their engineered metabolite bioproduction. On the other hand, starting from day 27, G' of this control group did not continue to decrease. Indeed, m found that +0.006, with G' measuring 7.6 ± 0.6 at day 27, 8.6 ± 0.4 at day 32, 8.7 ± 1.9 at day 37 (**Figure 3.7 b**). Likewise, dry mass change of ELM samples over switchable induction period showed similar trend with G' change. In Phase 1, there was no mass reduction during betaxanthin bioproduction with Cu^{2+} induction. Moreover,

the mass change behavior remained same (*p=0.1673*) in Phase 2, where Cu^{2+} containing media was replaced with inducer free media. However, the dramatic mass loss was observed in Phase 3 with Proteinase A production by galactose induction. Compared to Phase 1, the mass change in Phase 3 was found significantly different (*p =0.0013*) (**Figure 3.7 d**).

Galactose induced ELM samples showed more rapid degradation compared to non-induced ELM, even the BSA-PEGDA matrix was exposed to betaxanthin on phase 1. There are likely two drivers for the rapid and consistent degradation in induced ELM group in Phase 3 which are higher proteinase activity at pH 4 than pH 7 (**Figure 3.4 d**), and pH-responsive interactions between betaxanthin and the BSA-PEGDA matrix. It was observed potential structural changes in BSA-betaxanthin and Proteinase A–betaxanthin complexes at pH 4 (**Figure 3.7 c and f**).

3.3.5 *Additive manufacturing and bio-augmentation of ELMs as high-performance bioplastics*

We next demonstrated the manufacturing, bio-augmentation, and bio-degradation life-cycle for ELM bioplastics that serve as functional components. To showcase the versatility of the additive manufacturing process, we fabricated several items that included spoons, and interlocking puzzle pieces. All of these ELMs were then subjected to Cu^{2+}-induced betaxanthins production and then dried to remove the water and afford the ELM bioplastic. These objects underwent isotropic de-swelling during the drying process.

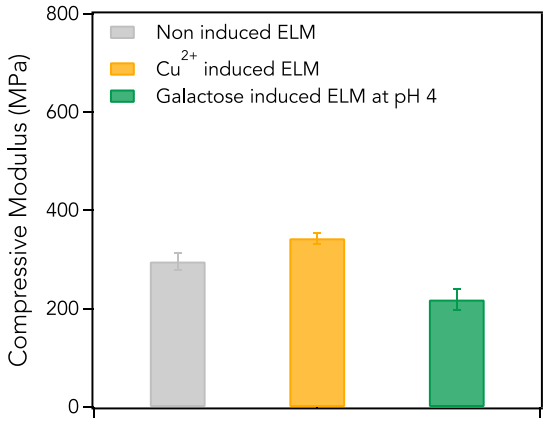

Figure 3.8. Effects of inducible bioproduction on mechanical stiffness of bioplastic ELMs.

The compressive modulus of the Cu^{2+} induced bioplastic ELMs after 5 days of culturing was 343 ± 11 MPa, exceeding that of the non-induced ELM (296 ± 17 MPa) and the acidic galactose-induced ELM (218 ± 22 MPa, $p = 0.0016$) (**Figure 3.8**). Thus, the improvement in the mechanical stiffness of the ELM bioplastics in the presence of betaxanthins produced *in situ* demonstrates the successful bio-augmentation of these materials. The ELM bioplastic objects were stable over indefinite periods of use. For example, we demonstrated the versatility and usability of the inducible ELM system by 3D printing wall hooks that could be further assembled via a dovetail joint. After printing, the hooks were easily assembled and left to dry in the bioplastic state for 7 days (**Figure 3.9 a**). One of the many advantages of 3D printing is the versatility—we printed the hooks in two sizes (14 mm and 20 mm once dried) without any changes to our existing printer hardware. We cultured the hooks in Cu^{2+} containing media to improve their bioplastic stiffness via betaxanthins production as demonstrated in our compression experiments (**Figure 3.8**). After

drying into the stiffened bioplastic form, the hooks could be attached to walls and support objects such as sweaters, scissors, wrenches, and keychains up to 40 times their weight (**Figure 3.9 b**).

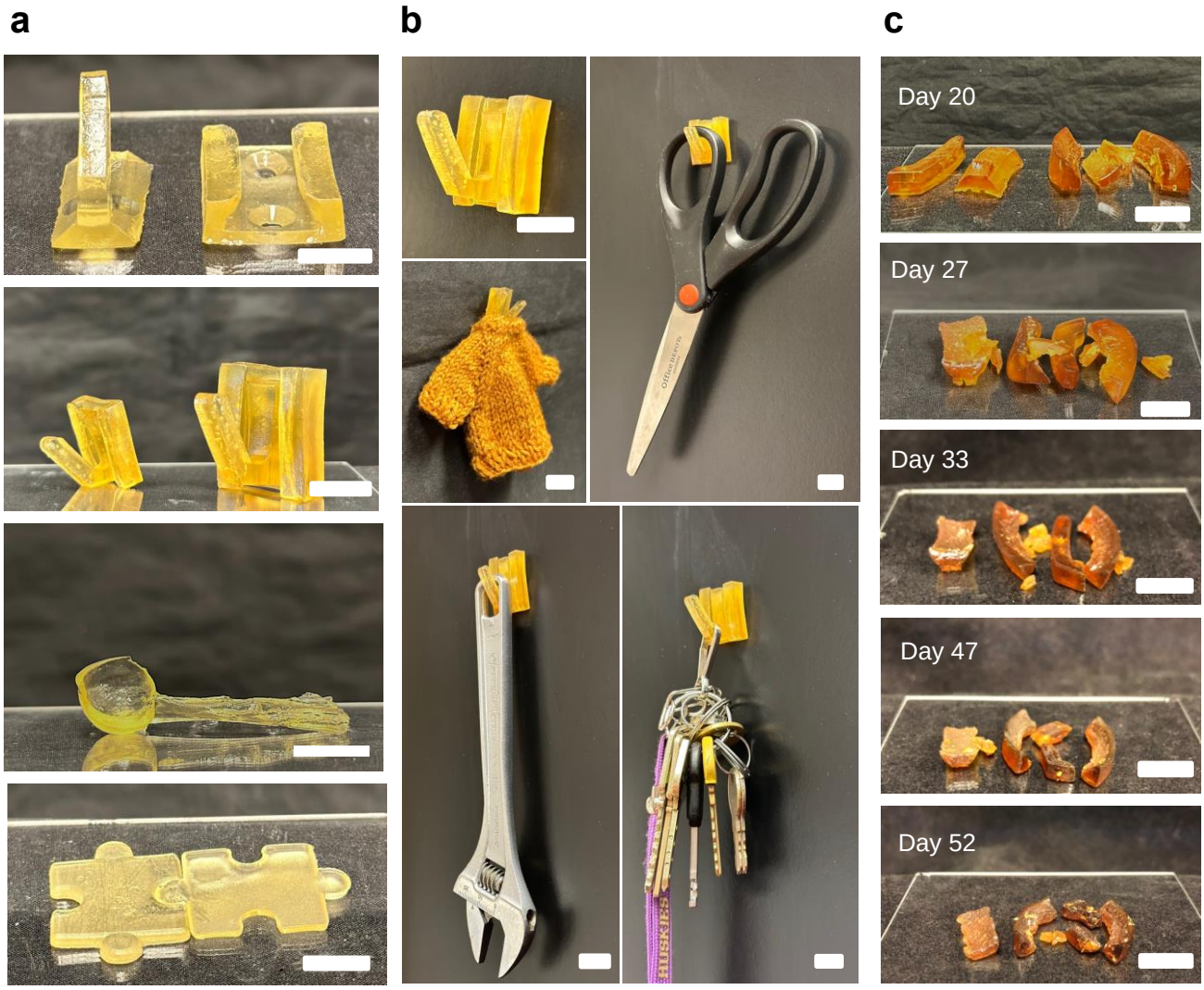

Figure 3.9. 3D printed inducible ELMs structures are in bioplastic form in dried state. a) 3D printed inducible ELM in wall hook form assembled after obtaining 3D wall hooks pieces. 3D printing allows fabrication in customized size. Wall hooks induced with Cu^{2+} for betaxanthin bioproduction to improve mechanical stiffness for a day. B) Examples of how wall hook can carry different items of varying masses (scissors: 58 g, wrench: 128 g, keychain: 108 g) C) At the end of usage period, wall hooks induced with galactose at pH 4 for proteinase A production to start degradation.

ELMs can preserve encapsulated microorganisms under dehydrated conditions for extended periods of time, and these cells can be reactivated upon rehydration with media[2,6]. We investigated the preservation and reactivation of ELM bioplastics after 60 days of use under

ambient conditions in the bioplastic state. We observed that the engineered *S. cerevisiae* in the 3D printed hooks were reactivated upon introduction to culture media, and the bioproduction of the samples remained responsive to the inducer type in the culture media (**Figure 3.10**).

At the end of their usage period as a bioplastic, the samples were first incubated with non-inducing media for 7 days before being transferred to galactose-containing media at pH 4 to induce Proteinase A expression to accelerate degradation (**Figure 3.9 c**). After 5 days, the hooks lost their structural integrity, and after 19 days of galactose induction at pH 4, the hooks lost 72% of their mass (**Figure 3.11**). Similar results were observed for 3D printed interlocking puzzle pieces and spoons (**Figures 3.9-11**).

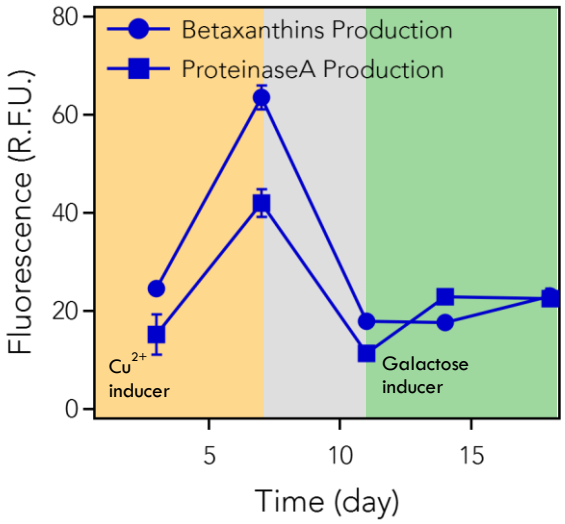

Figure 3.10. Betaxanthins and Proteinase A bioproduction of 3D printed ELMs after 60 day extended dehydration. Sample was stored in the bioplastic state for 60 days at ambient conditions before being induced with Cu^{2+} (orange) for 7 days, transferred to non-inducing media (gray) for 4 days, and 7days in galactose-containing media at pH 4 (green).

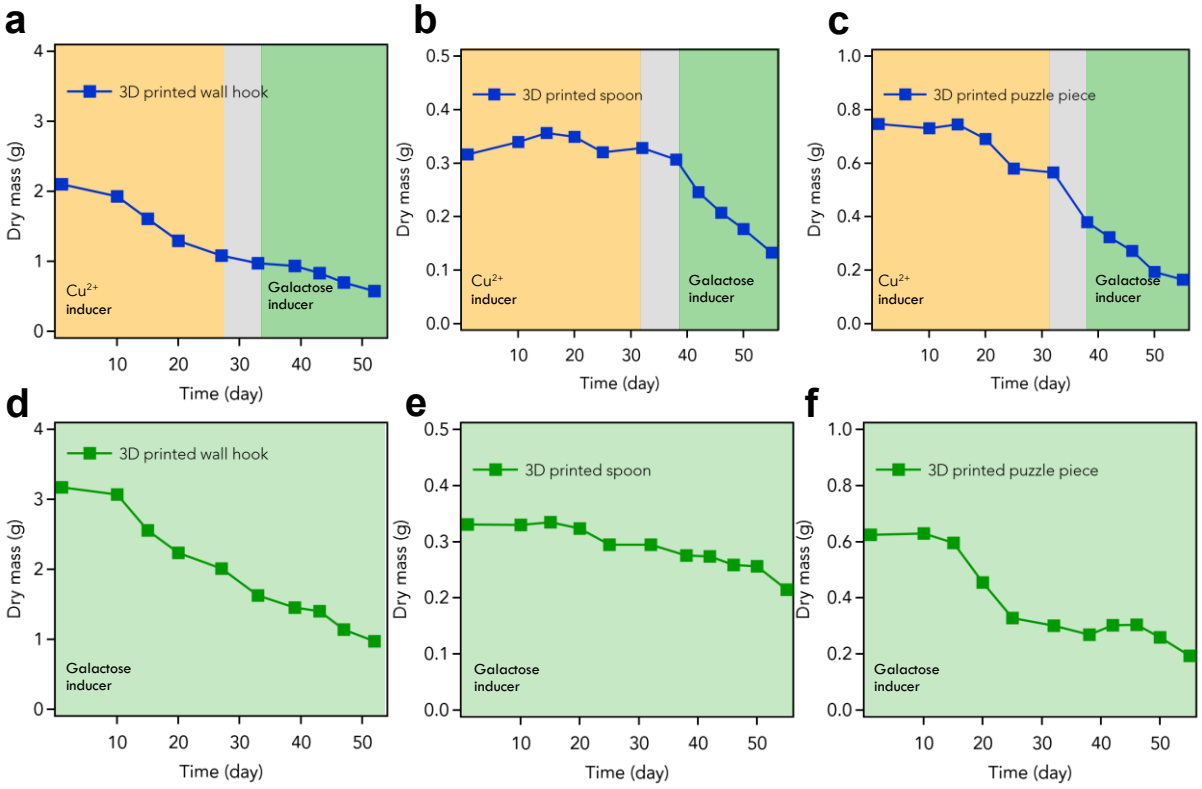

Figure 3.11. Dry mass change of 3D printed inducible ELMs in different inducers (yellow-Cu^{2+}, gray – no inducer, green-galactose at pH 4). a) 3D printed wall hook incubated with Cu^{2+} inducer for 27 days, 7 days in non-inducing media, and 19 days with galactose inducer at pH 4. b) 3D printed spoon incubated with Cu^{2+} inducer for 32 days, 7 days in non-inducing media, and 16 days with galactose inducer at pH 4. c) 3D printed puzzle piece incubated with Cu^{2+} inducer for 32 days, 7 days in non-inducing media, and 16 days with galactose inducer at pH 4. d) 3D printed wall hook incubating with galactose inducer at pH 4. e) 3D printed spoon incubated with galactose inducer at pH 4. f) 3D printed puzzle pieces incubated with galactose inducer at pH 4.

3.4 CONCLUSION

In this study, we developed the bio-augmented additive manufacturing of ELMs as high-performance bioplastics with end-of-use biodegradation. The materials were genetically programmed to undergo mechanical stiffening with the Cu^{2+}-induced production of betaxanthins and proteolytic degradation with galactose-induced production of proteinase A. Betaxanthins

enhanced the modulus of the bioplastic materials and also reduced the degradative activity of native proteolytic enzymes of *S. cerevisiae*, while proteinase A enabled the rapid on-demand degradation of the ELM bioplastic. The ELMs were 3D printed using a vat photopolymerization process, which afforded different objects that included spoons, wall hooks, and puzzle pieces. 3D printed ELMs not only provide a new approach toward bio-manufacturing, but they also represent a new strategy toward the hybrid manufacturing wherein the encapsulated cells can augment the native properties of the material. Additional genetic program enables the incorporation of other material functions that can include biodegradation as we have shown. These smart materials have the potential to significantly contribute to a more environmentally conscious and sustainable solutions for the plastics economy.

3.5 EXPERIMENTAL SECTION

3.5.1 *Materials*

Bovine serum albumin purchased from (Nova Biologics). Polyethylene glycol diacrylate (M_w 700 g/mol), and sodium persulfate, were supplied from Sigma-Aldrich. Tris(2,2′-bipyridyl) ruthenium (II) chloride hexahydrate ($Ru(bpy)_3Cl_2$), yeast extract, peptone, glucose and geneticin were obtained from Thermo Fisher Scientific.

3.5.2 *Strains, plasmids, media*

All plasmids used in this study are listed in Table 1. PCR fragments for assembly were amplified using Q5 High-Fidelity DNA Polymerase (New England BioLabs) for cloning using Q5 High-Fidelity 2X Master Mix (New England BioLabs). The assembled plasmids were transformed into electrocompetent *E. coli* DH10B cells (Thermo Fisher Scientific) and selected on LB agar plates supplemented with antibiotics (100 μg/ml Ampicillin or 50 μg/ml Kanamycin). Plasmids

were purified using a GeneJET Plasmid Miniprep Kit (Thermo Fisher K0502) according to the manufacturer's protocol. Plasmid concentrations were quantified via spectrophotometry (Nanodrop 2000c, Cat. ND-2000C). Constructs were confirmed by Sanger sequencing, and sequencing results were analyzed using Benchling. For proteinase A production, the plasmid PlTy3-GAL1-ScPEP4 was digested with XhoI for integration into the delta region and transformed into *S. cerevisiae* BY4741 cells via the Frozen EZ Yeast Transformation II Kit (Zymo Research). Successful transformants were selected on YPD agar plates supplemented with G418 (200 µg/ml) and confirmed via colony PCR. For betaxanthins production, the plasmid p415-UraInt-pCup1-MjDOD-CYP76AD5 was linearized using NotI for integration into the Ura locus and transformed into protease-producing *S. cerevisiae* BY4741 cells via the Frozen EZ Yeast Transformation II Kit (Zymo Research) to yield strain spk05. Successful transformants were selected on SC agar plates lacking Leucine and confirmed via colony PCR as well as by the presence of fluorescence.

Table 3.1. Plasmids used in this study.

Plasmid or Integrative Cassette	Promoter	Minimal Promoter	CDS	gRNA	Terminator	Marker	Ori	Description
PlTy3-GAL1-ScPEP4 (integrative cassette)	pGal1	X	ScPEP4	X	tPRM9	G418 (*S. cerevisiae*), Kan (*E. coli*)	ColE1	pITy3 backbone protease-production plasmid for integration into *S. cerevisiae*
P415-UraInt-pCup1-MjDOD-CYP76AD5 (integrative cassette)	pCUP1 (gene 1) pTDH3 (gene 2)	X	Gene 1: MjDOD (T261N) Gene 2: CYP76 AD1	X	tTDH1	Leu (*S. cerevisiae*), Amp (*E. coli*)	ColE1	P415 Mumberg Backbone betaxanthins-production plasmid for integration into *S. cerevisiae*

3.5.3 *3D printing of Inducible ELM Constructs*

Inducible ELM constructs were prepared encapsulation of S. cerevisiae spk05 cells with protein-based polymer matrix during vat photopolymerization 3D printing. To prepare protein-based polymer matrix BSA-PEGDA conjugates were used which were formulated according to a protocol described in Chapter 2[8]. Briefly, 20 grams of BSA-PEGDA conjugate solution, 10 wt% PEGDA was dissolved in 11.2 culture media. Then 30 wt% BSA in powder form was added to the PEGDA solution in small portions and vortexed for a minute to let react PEGDA with BSA. The BSA-PEGDA conjugate solution was stored overnight at 4 ^{o}C. The day after, freshly grown S. cerevisiae spk05 cells, which were incubated overnight at 30 C with orbital shaking at 220 RPM in 4 mL YPD media (10 g/L yeast extract, 20 g/L peptone, 20 g/L glucose) with 50 g/mL geneticin (G418), were added to BSA-PEGDA conjugate solution. Cell density was measured by OD_{600} and 1 mL of cell suspension that contains $3x10^7$ cell/mL was added to 20 grams of resin. Then, a photo initiator system, 0.075 wt% $Ru(bpy)_3Cl_2$ and 0.24 wt % sodium persulfate, was introduced to the formulation. An SLA 3D printer (Formlabs Form 2) was used to fabricate ELM objects. The 3D printer operated in Open Mode using a layer height of 100 μm and photocured using a 405 nm violet laser (250 mW) with 140 μm laser spot size. Autodesk Fusion 360 was used to create the 3D models, or they were downloaded from Thingiverse.

3.5.4 *Induction systems and bioproduction*

3D printed ELM constructs were prepared by *S. cerevisiae* spk05 cells in non-induced state. Different inducers were used to start different products as follow; *Betaxanthin production:* ELM constructs cultured with YPD media contains 0.5 mM $Cu_2SO_4.5H_2O$ inducer. *Proteinase production:* ELM constructs cultured with 2 wt% galactose containing culture media (10 g/L yeast extract, 20 g/L peptone and 50 g/mL geneticin*). Control group*: ELM constructs cultured with

YPD, no inducer. To determine the bioproduction samples collected from culture media every 48 h, centrifuged at 4400 rpm for 10 min, supernatants were collected and stored at -20 ^{o}C until analysis performed. Betaxanthin bioproduction was determined by fluorescence intensity measurement at excitation/emission: 485 nm/520 nm using a Fluoroskan Ascent FL Fluorescence Microplate Reader from Thermo Labsystems. Amplite® Universal Fluorimetric Protease Activity Assay Kit (AAT Bioquest) was used to quantify the amount of functional proteinase A. Assay was performed according to the procedure provided by the manufacturer.

3.5.5 *Florescence microscopy imaging*

EVOS Fluorescent Imaging Microscopy was used to image *S. cerevisiae* spk05 cells before and after induction. Cell viability was also calculated from florescence microscopy images of stains cells. Biotium Live/Dead Yeast staining kit was used to cell staining according to the procedure provided by the manufacturer.

3.5.6 *Monitoring the effect of different induction cycles on mechanical properties*

In order to examine how induction cycles affect mechanical properties, we measured compressive modulus, storage modulus, loss modulus, mass, and volume changes in ELM constructs.

Measurement of compressive modulus: 3D printed ELM constructs were fabricated as a cylindrical disk (x = 10.5 mm, y = 10.5 mm, z = 7 mm) shape. Then, they were dried in room temperature for a week. Dried ELM constructs were incubated in different culture medias which are media contained $Cu_2SO_4.5H_2O$ inducer, media contained galactose inducer, media contained both $Cu_2SO_4.5H_2O$ inducer and galactose inducer. As a control group ELM construct culture in inducer free media. A Newton Test Machine electromechanical test frame with 1 kN load cell and

a crosshead rate of 1.3 mm/min was used to assess compression experiment. The compressive modulus was calculated based on the slope of the stress (kPa)-strain(mm/mm) curve where 0.05 (mm/mm) - 0.1 (mm/mm) of strain region.

Measurement of loss and storage modulus: ELM constructs were prepared by casting the resin in cylindrical disks (x = 20 mm, y = 20 mm, z = 1 mm) under 405 nm for 12 minutes. Samples were removed from their mold and placed in appropriate cell culture media and incubated at 30°C with orbital shaking at 220 rpm. After a specified number of data, constructs were removed from culture media and rinsed twice with distilled water and swelled to equilibrium overnight in distilled water to mitigate electrostatic interactions affecting material properties. A TA Instruments Rheometer was used to perform the testing. Before testing, samples were trimmed to match the rheometer's 20 mm parallel plate geometry (x = 20 mm, y = 20 mm) and weighed to obtain their wet mass. Samples were loaded onto a Peltier plate set at 21°C with the aforementioned geometry and compressed at 2N axial force until stable storage and loss moduli values were obtained (0.5% tolerance, 5 consecutive points). Samples were measured in triplicate at 0.2% strain, 1 Hz for 180 seconds to obtain storage and loss moduli values. To obtain the dry mass, samples were left to dry overnight at ambient conditions.

3.5.7 *Statistical analysis*

One-way ANOVA, Welch Test (p value of < 0.05) were used to calculate statistical differences by Igor Pro (Version 8.04) software. For multi-group comparisons, Tukey HSD, (p value of < 0.05) were used to calculated statistical differences by JMP Pro (Version 16.0) software. The standard deviations (± S.D.) of replicates were calculated in Excel.

CHAPTER 4. ENGINEERED LIVING MATERIAL BIOREACTORS WITH TUNABLE MECHANICAL PROPERTIES USING VAT PHOTOPOLYMERIZATION

This Chapter is adapted with permission from Altin-Yavuzarslan, G., Sadaba, N., Brooks, S. M., Alper, H. S., & Nelson, A. Engineered Living Material Bioreactors with Tunable Mechanical Properties using Vat Photopolymerization. *Small*, 2306564. Copyright 2023, Wiley, Online Library.

4.1 ABSTRACT

3D-printed engineered living materials (ELMs) are promising bioproduction platforms for agriculture, biotechnology, sustainable energy, and green technology applications. However, the design of these platforms faces several challenges, such as the processability of these materials into complex form factors and control over their mechanical properties. Herein, we present ELMs as 3D printed bioreactors with arbitrary shape geometries and tunable mechanical properties (moduli and toughness). Poly(ethylene glycol) diacrylate (PEGDA) was used as the precursor to create polymer networks that encapsulated the microorganisms during the vat photopolymerization process. A major limitation of PEGDA networks is their propensity to swell and fracture when submersed in water. We overcame this issue by adding glycerol to the resin formulation to 3D print mechanically tough ELM hydrogels. While polymer concentration affects the modulus and reduces bioproduction, ELM bioreactors still maintain their metabolic activity regardless of polymer concentration. These ELM bioreactors have the potential to be used in different applications for sustainable architecture, food production, and biomedical devices that require different mechanical properties from soft to hard.

4.2 INTRODUCTION

Engineered living materials (ELMs) have received significant interest as bioreactors for the on-demand production of high value chemicals[2,3,56,58104,105]. ELM bioreactors are constructed by embedding genetically engineered microorganisms in polymer networks to produce a broad range of high value bioactive compounds including antioxidants, polyphenols, betalains, terpenoids, alkaloids, and peptides[2,3,5,106]. While the cells serve as microscale bio-factories for chemical production, the polymer matrix serves to ensure structural integrity, protect the incorporated cells from adverse environmental conditions, and enable the processability of ELMs into the desired form factors.

Additive manufacturing is a powerful strategy to fabricate 3D-printed ELMs with arbitrary designs and form factors[1,3,5]. The most important considerations for selecting the appropriate polymer matrix are the biocompatibility toward the encapsulated cells and the viscoelastic properties of the material to be 3D printed. It has been reported F127-based hydrogels for microbial encapsulation and extrusion 3D-printing into ELM bioreactors[2,3,6]. These hydrogels are advantageous for their reversible temperature-responsive behavior, wherein the gels become liquid at ~5 °C, which facilitates the homogeneous incorporation of cells prior to returning to the gel state. These cell-laden hydrogels are also shear-thinning and self-supporting at ambient temperature, which is ideal for direct ink write 3D printing (DIW 3DP). While F127-based materials have been successful as a platform for on-demand production and cell preservation[3], DIW 3DP is limited in its ability to create complex object geometries and other user-defined form factors.

Vat photopolymerization 3D printing uses light to photo-pattern liquid resins into 3D objects and produce complex 3D constructs with a high resolution[64]. To date, there are few

examples of ELMs produced using light-based vat photopolymerization methods. The requirements for vat photopolymerization resins are (i) a low viscosity (<10 Pa·s) and (ii) a fast-photocuring rate at the appropriate wavelength of irradiation[66,67]. For ELM bioreactors, the engineered cells should be incorporated into the liquid resin and incorporated into the polymer matrix during the printing process. Binelli *et al.* reported DLP 3D printing ELMs using a methacrylated hyaluronic acid (HAMA) and a methacrylated PEO-PPO-PEO copolymer to print *Photobacterium kishitanii*[107]. A BSA-based resin was also reported for the vat photopolymerization with *E. coli* or *S. cerevisiae* to create bioaugmented ELMs[5]. Both of these approaches use a biopolymer for the polymer matrix, which can be susceptible to biofouling and enzymatic degradation that can potentially affect the long-term production of bioreactors.

Aqueous solutions of polyethylene glycol diacrylate (PEGDA) can be photocured in the presence of a photo-radical generating system to afford polymer network hydrogels. These synthetic materials have been 3D patterned by casting into molds or 3D printing via vat photopolymerization for tissue engineering applications[62,108-113]. Mammalian cells can be highly sensitive to the mechanical and chemical features of the polymer matrix, whereas yeast cells, such as *S. cerevisiae* are more tolerant of these conditions. To the best of our knowledge, there has not been an investigation of how the mechanical stiffness and toughness of the matrix can affect the behavior of *S. cerevisiae* within these photopatterned matrices, particularly in the context of ELMs for bioproduction.

Herein, we utilize vat photopolymerization to 3D print ELM bioreactors with arbitrary shape geometries and tunable mechanical properties (modulus and toughness) (**Figure 4.1**). The resin formulations comprised aqueous solutions of poly(ethylene glycol) diacrylate (PEGDA, 700 g/mol) with genetically engineered *S. cerevisiae* and a photoradical generator to initiate the

polymerization. Glycerol was an essential additive in these formulations that enhanced the resolution of the printed features and overall improvement of mechanical properties in terms of stiffness and toughness of the hydrogels, particularly as the concentration of PEGDA was increased in the formulation. Once this formulation was established, *S. cerevisiae* cells were encapsulated within a PEGDA extracellular matrix, and their growth, metabolic production, and ELM mechanical properties were investigated.

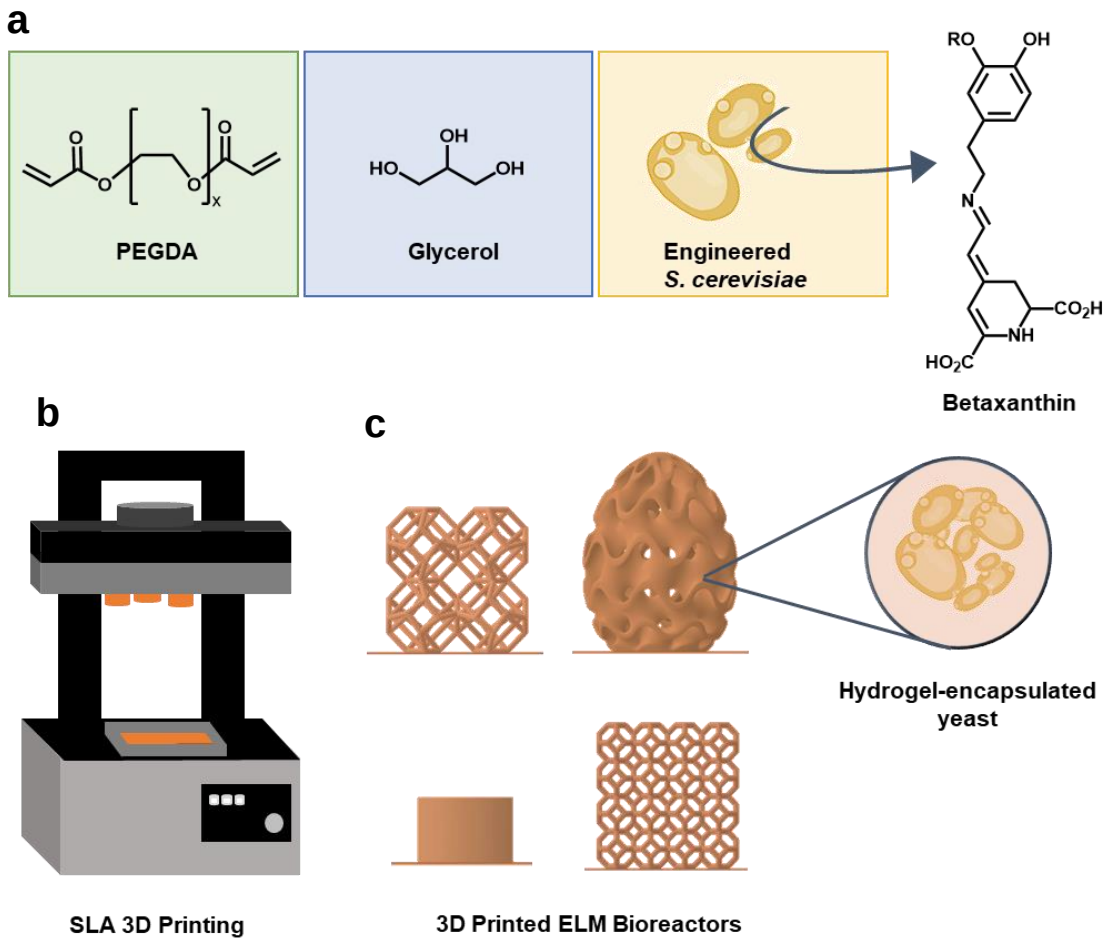

Figure 4.1. General scheme of the study. a) Engineered living material (ELM) resin includes an aqueous solution of PEGDA (M_w 700 g/mol), glycerol, metabolically engineered *S. cerevisiae* that produces betaxanthin, and photo initiating system (not shown). b) The resins were SLA 3D printed c) to form hydrogels as ELM bioreactors with a range of different geometries. The cells are encapsulated within the polymer matrix of the hydrogels.

4.3 RESULT AND DISCUSSION

4.3.1 *Glycerol improves the 3D printing resolution and mechanical properties of PEGDA networks.*

Despite the commercial availability and biocompatibility of PEGDA, to the best of our knowledge, PEGDA has not been reported for the bioprinting of ELMs using a vat photopolymerization process. Hissam and co-workers reported[114] the vat photopolymerization of PEGDA to fabricate cell-free hydrogels. The primary limitation of using PEGDA as a primary component in an aqueous resin formulation is the mechanical brittleness of the PEGDA polymer network at concentrations above 20 wt%. As the concentration of PEGDA in the resin formulation increased, the hydrogels became stiffer with concomitant increase in their fragility. More specifically, when submerged in water, the printed hydrogels expanded to the point of breaking apart as a consequence of the osmotic flow of water into the hydrogel networks. Thus, PEGDA on its own does not provide a mechanically robust matrix for bioprinting with cells.

The addition of glycerol has been shown to improve the mechanical properties of synthetic and biological hydrogels. The physical properties of polyacrylamide,[115] gelatin,[116] and cellulose[117] hydrogels were all improved by the addition of glycerol. Thus, we hypothesized that glycerol could be used as an additive for 3D printing mechanically robust ELM hydrogels via a vat photopolymerization process. We first investigated the printability of aqueous PEGDA and PEGDA-glycerol formulations using polymer concentrations of 20, 40, and 60 wt%. The composition of the resin formulations investigated here (with and without 5 wt% glycerol) is summarized in **Table 4.1**.

Table 4.1. Rheological characterization of resin formulations. Each data point represents the mean (n = 3) and error bars represent standard deviation.

Sample Name	PEGDA wt (%)	Glycerol wt (%)	Viscosity μ (Pa·s)	Loss Modulus G'' (MPa)	Storage Modulus G' (kPa)
20PEGDA	20	-	1.6 ± 0.2	0.07 ± 0.001	1.2 ± 0.2
20PEGDA-5Gly	20	5	2.8 ± 0.2	0.1 ± 0.01	3.4 ± 0.5
40PEGDA	40	-	9.2 ± 0.2	1.4 ± 0.06	59.9 ± 12.1
40PEGDA-5Gly	40	5	10.3 ± 0.2	1.2 ± 0.05	106.0 ± 4.9
60PEGDA	60	-	31.1 ± 0.3	1.9 ± 0.12	284.3 ± 54.3
60PEGDA-5Gly	60	5	33.9 ± 0.4	2.4 ± 0.23	640.3 ± 63.1

The sample name for each resin identifies the concentration of PEGDA and whether or not glycerol is present in the resin. For example, 20PEGDA comprises 20 wt% PEGDA without glycerol, whereas 20 wt% PEGDA-5Gly has the same PEGDA content with 5 wt% glycerol. A commercial stereolithographic apparatus (SLA) 3D printer used in this study, and 0.075 wt% $Ru(bpy)_3Cl_2$ with 0.24 wt% sodium persulfate was used as the photo initiating system that could be activated using 405 nm light. Resins for vat photopolymerization require a low viscosity (< 5 Pa·s) to have sufficient reflow (re-coating of the next photopolymerizable layer) during the printing process.[64,66,67] As expected, the viscosity of the resin increased with increasing amounts of PEGDA, but their values were well below the 5 Pa·s limit (**Table 4.1, Figure 4.2 a**). The rate of resin photocuring was evaluated via photorheology by monitoring the change in storage modulus

(G') with time of irradiation with 405 nm light. All formulations showed fast photocuring and reached their maximum storage moduli within 10 s (**Figure 4.2 d**).

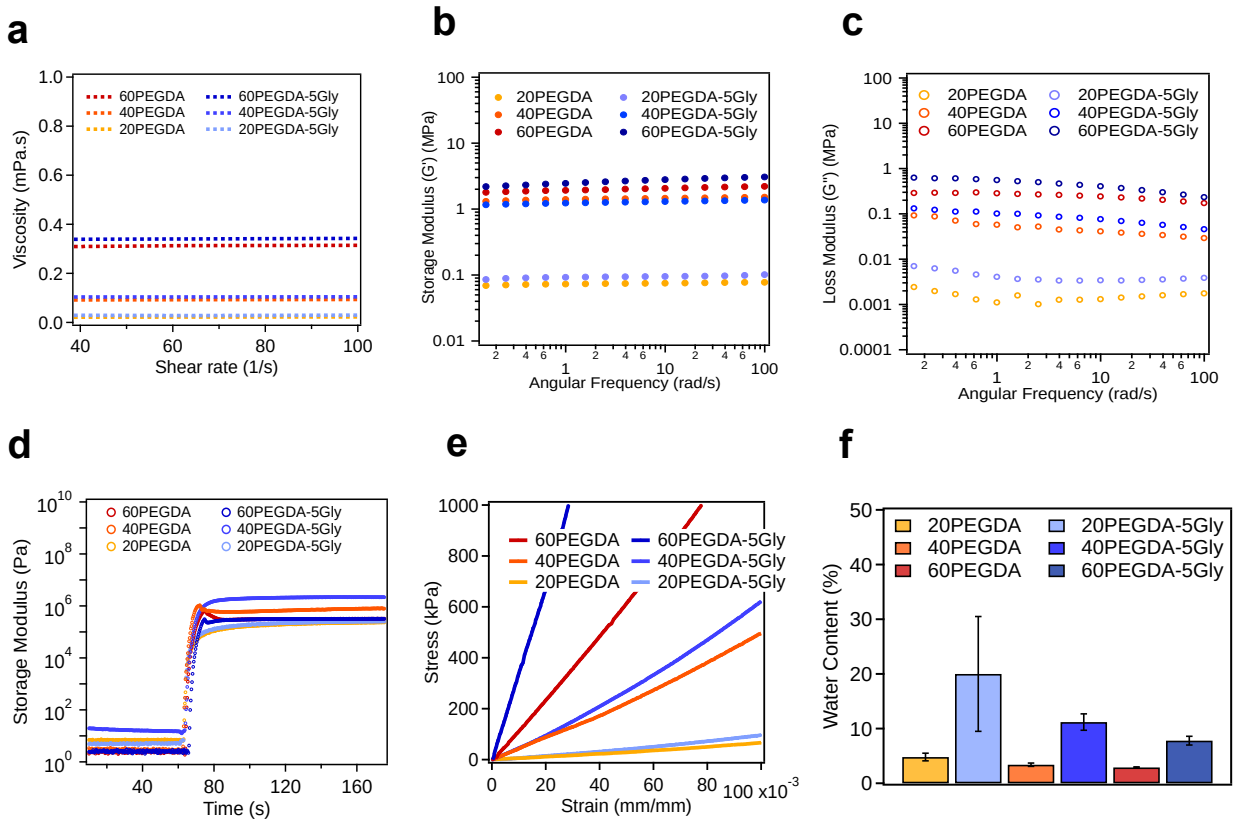

Figure 4.2. Effect of concentration and presence of glycerol on material properties of PEGDA. a) Effect of PEGDA concentration and presence of glycerol on viscosity. b) Effect of PEGDA concentration and presence of glycerol on storage modulus. c) Effect of PEGDA concentration and presence of glycerol on loss modulus. d) Effect of PEGDA concentration and presence of glycerol on photocuring behavior. e) Stress-strain curve of 3D printed PEGDA resin formulations with and without glycerol. f) Water content of 3D printed PEGDA and PEGDA-Glycerol samples.

Figure 3 a-c shows the differences in resolution between the printed lattice constructs using resin formulations in Table 1. The features were better resolved as the concentration of PEGDA in the resin was increased from 20 wt% to 60 wt% (**Figures 4.3 a-c, 4.4**). The 20PEGDA resin printed with poorly resolved features, but interestingly, the addition of 5 wt% glycerol to this formulation significantly improved the resolution (**Figure 4.3 a**).

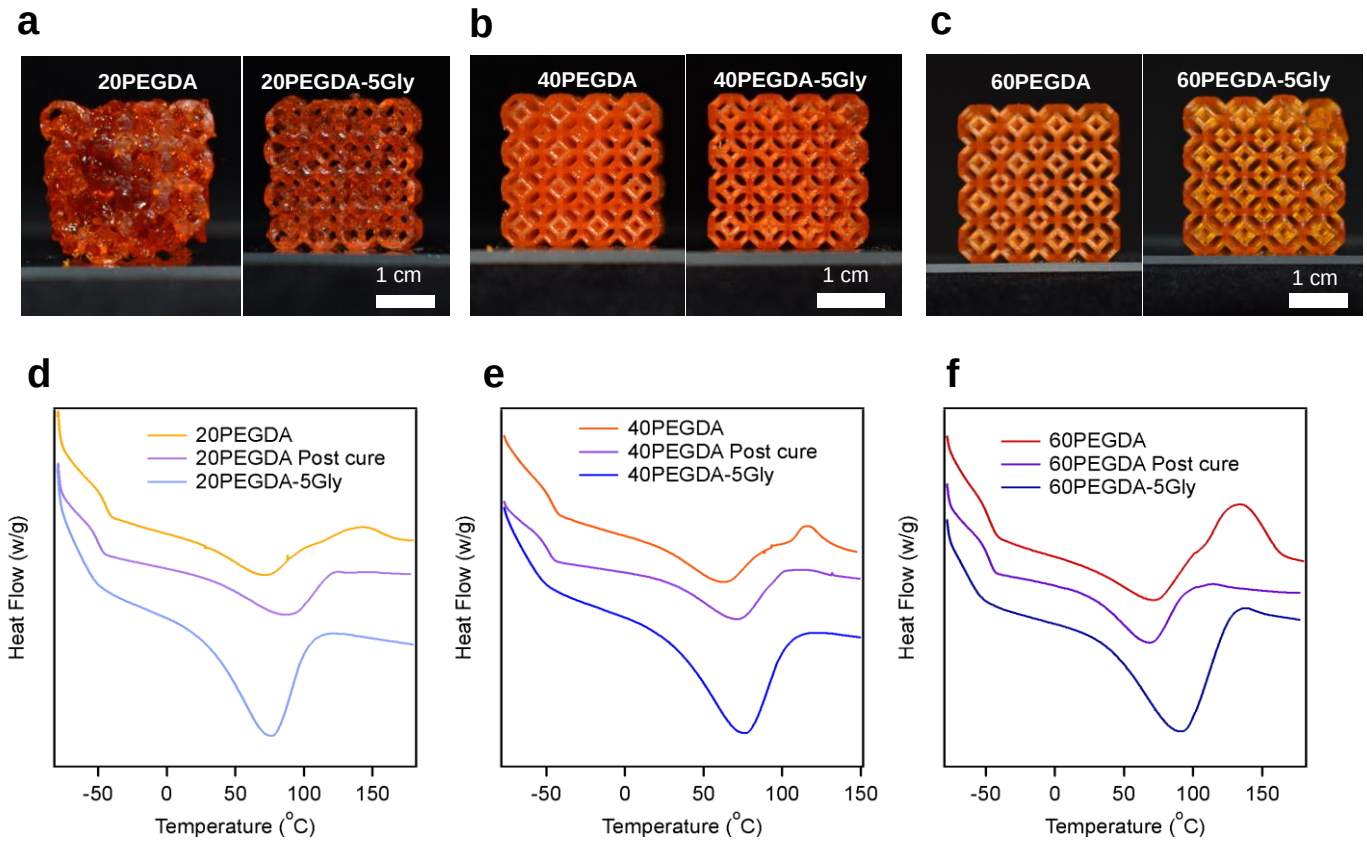

Figure 4.3. Effect of glycerol and PEGDA concentration on printability and thermal polymer properties of resin formulation. a-c) SLA 3D printed lattice structures formulated with a) 20PEGDA and 20PEGDA-5Gly, b) 40PEGDA and 40PEGDA-5Gly, c) 60PEGDA and 60PEGDA-5Gly. d-f) Differential scanning calorimetry data for samples formulated with d) 20PEGDA and 20PEGDA-5Gly, e) 40PEGDA and 40PEGDA-5Gly, and f) 60PEGDA and 60PEGDA-5Gly.

The formation of hydrogen bonds between glycerol and PEGDA could be responsible for the enhanced features. The interaction between glycerol and PEGDA is evident in the DSC thermograms for photocured PEGDA and PEGDA-glycerol resins. The glass transition temperature (T_g) for PEGDA is ~ -45 °C and becomes less defined in the presence of glycerol (**Figure 4.3 d-f, Table 4.2**). Thus, glycerol can interact with the PEGDA chains via hydrogen bonding interactions, and during the printing process, it may serve to noncovalently aggregate

PEGDA chains in a manner that facilitates network formation and improve the resolution of the printed construct.

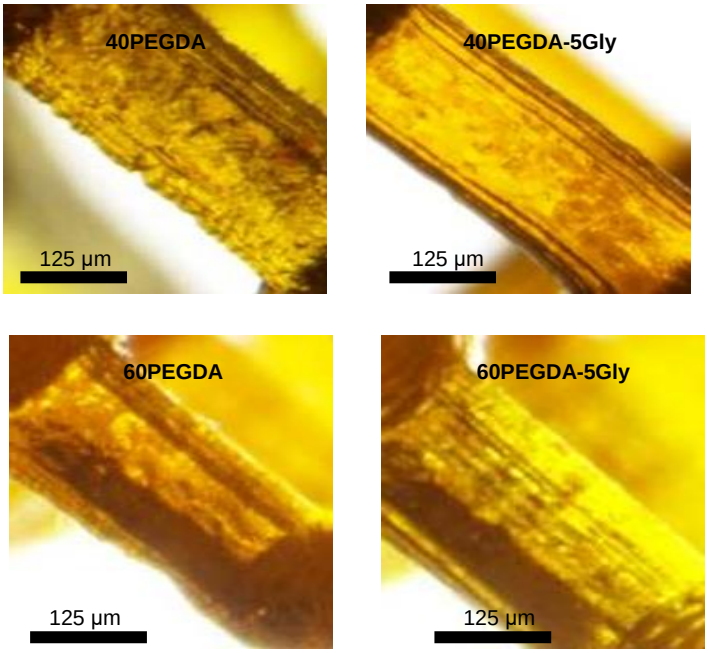

Figure 4.4. Optical microscopy images of 3D printed PEGDA-glycerol formulations.

The presence of glycerol also improves the incorporation of PEGDA into the polymer network, as evidenced by the consumption of the acrylate groups. The DSC for PEGDA shows the presence of an exothermic peak at 120 °C that increases as the PEGDA concentration increases. This exotherm arises from the thermal polymerization of unreacted acrylates in the samples[118,119]. However, when these samples are treated with a post-print cure, wherein the constructs are irradiated with 400 nm in a custom photocuring chamber (Quans, 400 nm, 1 mW cm^{-2}) for 60 min, the exothermic peak was not present for any of the samples (**Figure 4.3 d-e**). When glycerol was present in the resin formulation this endothermic peak was not present, which suggests that glycerol may promote efficient network formation by aggregating the PEGDA chains to facilitate the reaction of the chain ends.

Table 4.2. Effect of glycerol on thermal properties of PEGDA

Sample	T_g (°C)	T_m(°C)	ΔH_m (Jg^{-1})	T_c(°C)	ΔH_c (Jg^{-1})
20PEGDA	-45.10±0.36	71.48±0.05	43.79±4.48	127.62±14.38	18.51±1.76
40PEGDA	-44.87±0.10	72.93±2.44	53.35±4.54	114.93±4.00	21.95±3.27
60PEGDA	-46.67±0.62	74.91±2.68	59.42±5.75	121.37±12.41	52.33±0.66
20PEGDA post cure	-48.72±1.59	81.66±5.38	89.03±6.23	-	-
40PEGDA post cure	-47.31±1.90	75.58±4.11	54.96±1.17	-	-
60PEGDA post cure	-47.55±0.09	72.31±2.86	45.09±7.83	-	-
20PEGDA-5Gly	-55.89	97.08	144.2	-	-
40PEGDA-5Gly	-54.36±1.06	80.82±1.68	119.365±3.76	-	-
60PEGDA-5Gly	-53.86±0.07	75.98±0.23	89.29±1.92	-	-

4.3.2 *Characterization of 3D printed PEGDA and PEGDA-Glycerol hydrogels*

Bioreactors that are based on engineered living materials (ELM) must be submerged and incubated in aqueous culture environments during the production phase of the desired compound. To determine the possible usage of 3D printed PEGDA hydrogels for ELM bioreactors, we investigated their mechanical properties, shape integrity, and swelling ratio after submersion in aqueous media. We first investigated the effect of PEGDA concentration on compressive modulus in uniaxial compression experiments on 3D printed cylindrical samples (x = 10.5 mm, y = 10.5 mm, z = 7 mm). All of the resins tested afforded self-supporting hydrogels with moduli in the kPa to MPa range (736.5 ± 48.3 kPa, 5886.5 ± 326.5. kPa, 14808 ± 568.7 kPa for 20PEGDA, 40PEGDA, and 60PEGDA, respectively). As expected, the compressive modulus increased with PEGDA concentration in the formulation (**Figure 4.5 a**). Moreover, the addition of glycerol to the resin formulations increased the compressive moduli of the hydrogels 1.5, 1.2, and 2.5-fold relative to the 20PEGDA, 40PEGDA and 60PEGDA formulations, respectively.

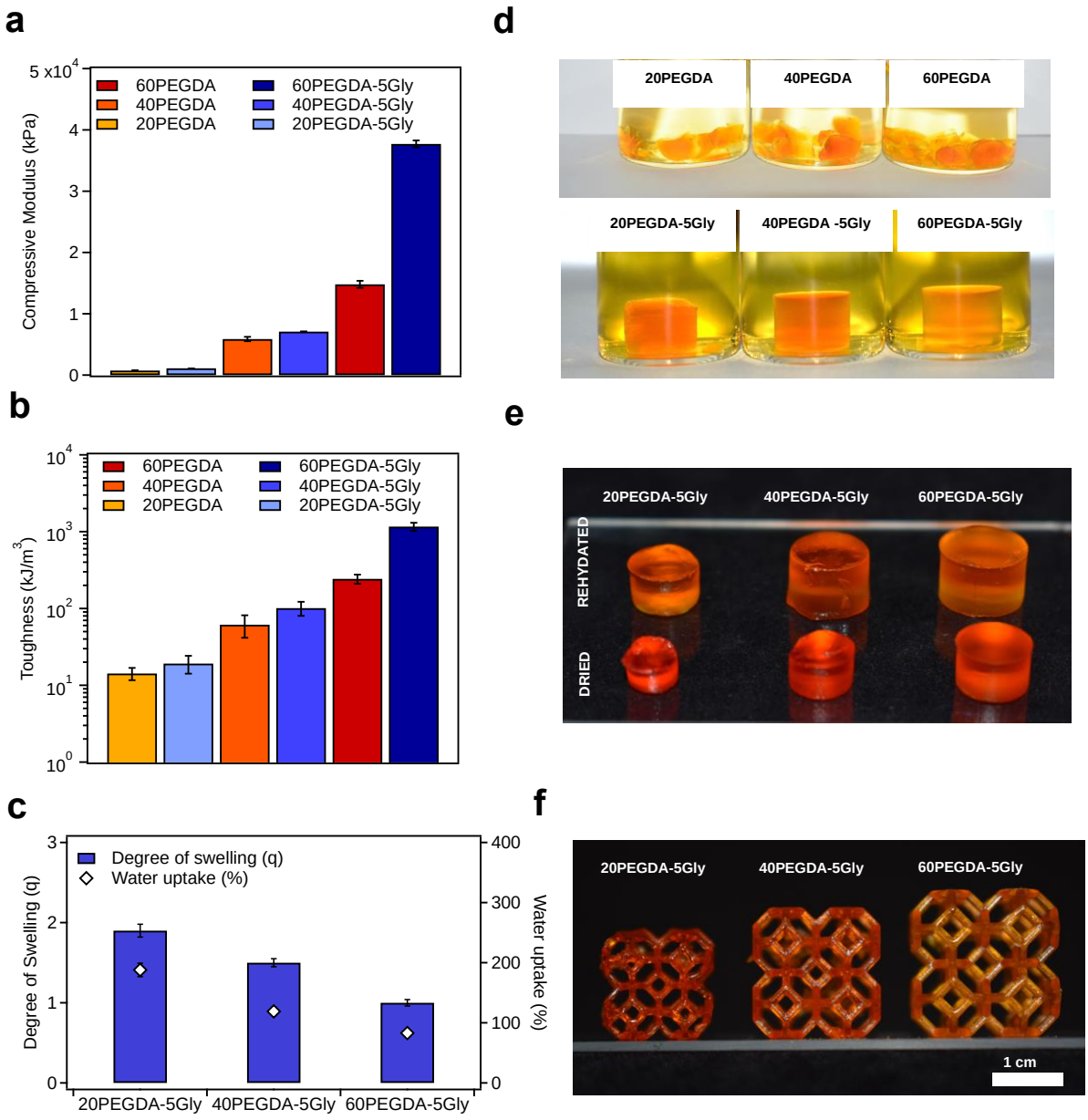

Figure 4.5. Characterization of mechanical properties of 3D printed formulations. a) Compressive modulus (kPa) values of 3D printed PEGDA resin formulations with and without glycerol. b) Toughness (kJ/m^3) values of 3D printed PEGDA resin formulations with and without glycerol. c) Degree of swelling and water uptake (%) of 3D printed samples formulated with PEGDA and glycerol. d) 3D printed samples in cylindrical pack shape incubated in water overnight. e) Optical image of 3D printed samples formulated with PEGDA and glycerol in dried and rehydrated state. f) Optical image of 3D printed PEGDA-glycerol samples in dried state. Each data point represents the mean (n = 3), and error bars represent standard deviation. Scale bar is 10 mm.

Moreover, the slope of the stress–strain curve increased with the presence of glycerol and increasing PEGDA concentration (**Figure 4.2 e**). Thus, the presence of glycerol in the resin formulation afforded hydrogel constructs that were mechanically stronger and tougher (**Figure 4.5 b**). Glycerol has the beneficial effect of enhancing the integrity of the hydrogels in their fully hydrated state. When 3D printed samples of the 20PEGDA, 40PEGDA and 60PEGDA resins were submerged in water, the osmotic flow of water into the sample caused the structures to swell and ultimately break into smaller pieces (**Figure 4.5 d upper**). In contrast, we observed that when the samples were prepared from resins with glycerol (20PEGDA-5Gly, 40PEGDA-5Gly and 60PEGDA-5Gly), they maintained their shape integrity (**Figure 4.5 d lower**) over the course of 8 days.

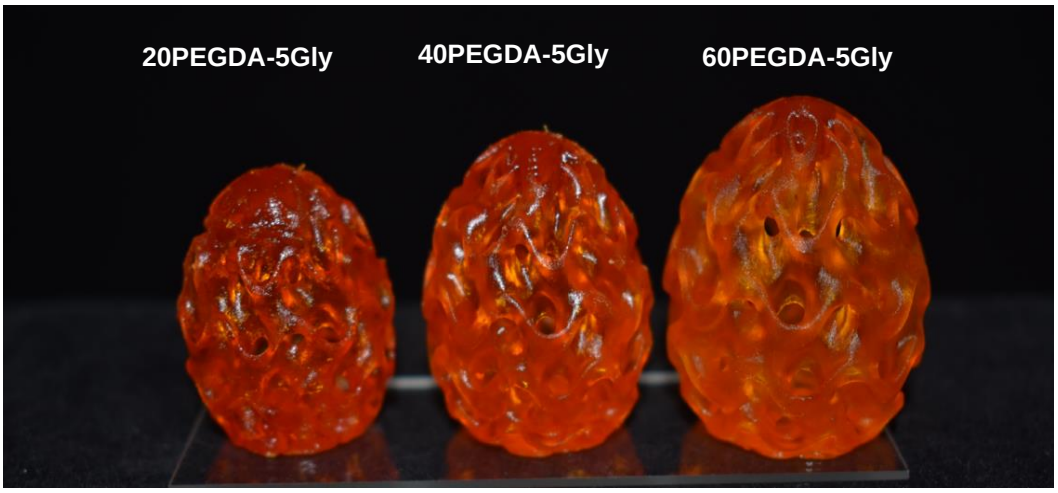

Figure 4.6. Optical images of SLA 3D printed ELM bioreactors in egg gyroid shape.

Optical images of 3D printed PEGDA-glycerol hydrogels in their dehydrated states are shown in Figure **4.5 e (lower), Figure 4.5 f** and **Figure 4.6**. As the polymer content in the resin formulation decreased, the 3D printed PEGDA-glycerol hydrogels isotopically decreased in size upon dehydration (**Figure 4.5 f, Figure 4.6**). The degree of swelling (q) and water uptake (%) were determined by immersion of dehydrated samples in water overnight (Figure **4.5 e**). The

swelling characteristics of the PEGDA-glycerol hydrogels were dependent upon polymer concentration, wherein the q and water uptake decreased as the PEGDA increased (**Figure 4.5 c**).

As a hygroscopic molecule, glycerol form hydrogen bonds with water molecules that limits evaporation of water during drying. We performed thermogravimetric analysis to calculate water and glycerol content of 3D printed hydrogels in dried state (**Figure 4.2 f, Figure 4.7**). Our results show that the water content of PEGDA-glycerol samples was significantly higher than samples prepared without glycerol (**Figure 4.2 f**). Peaks at 100 ^{o}C and ~200 ^{o}C in **Figure 4.7 b** represent water and glycerol content of samples, respectively. We detected slow leaking out of glycerol over time from 3D printed PEGDA-glycerol hydrogel samples which were incubated in water (**Figure 4.8**).

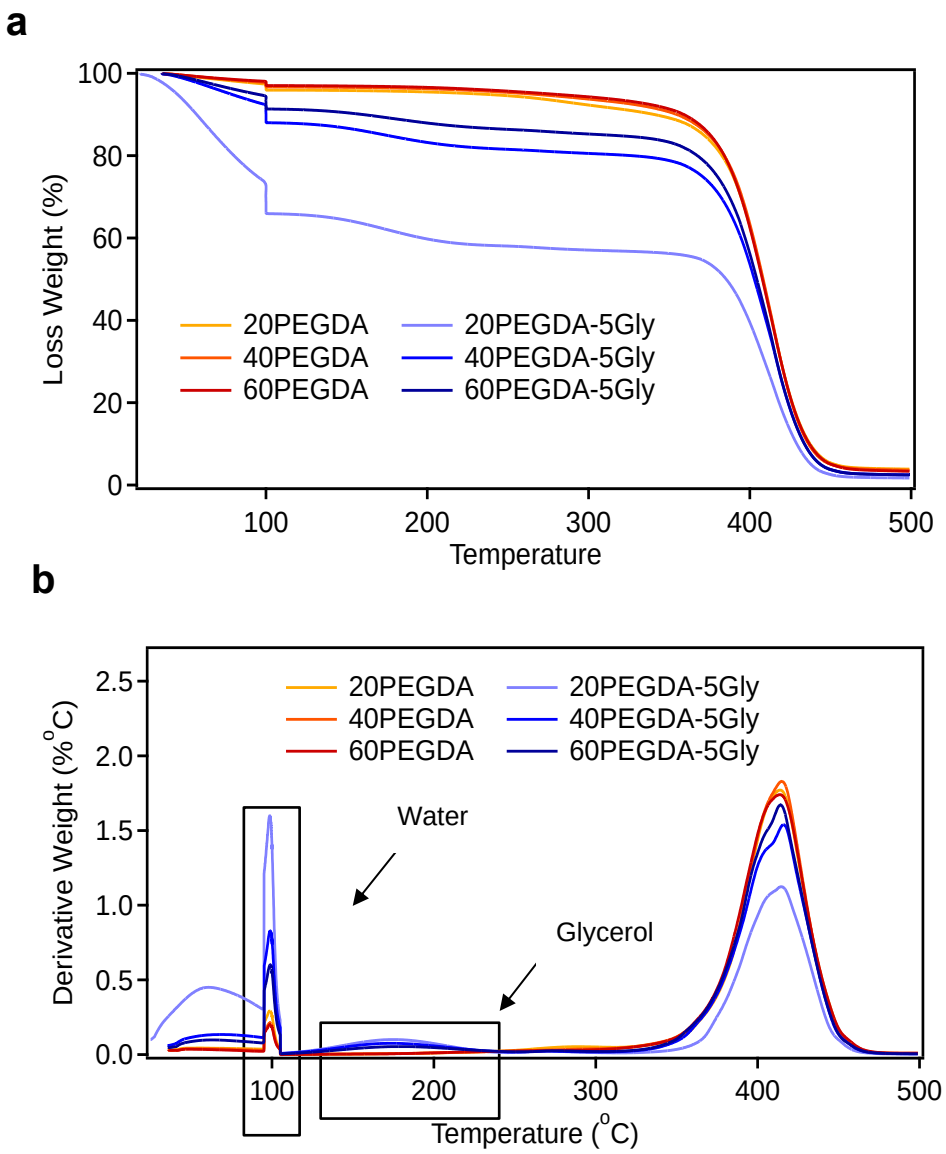

Figure 4.7. Thermograms of SLA 3D printed PEGDA and PEGDA-glycerol structures. a) Loss weight (%) of samples by heat increment. b) derivative weight (% ^{o}C) of samples by the increment of heat.

Still glycerol improves swelling induced cracking resistance of 3D-printed PEGDA hydrogels by affecting polymerization degree and water content of PEGDA hydrogels. Since glycerol-free 3D-printed samples became swollen and ultimately cracked in water, we concluded that these formulations were not suitable to formulate ELM bioreactors. Indeed, we observed same

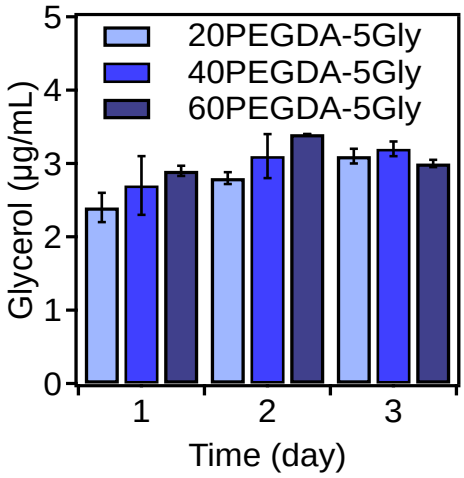

Figure 4.8. Leaking of glycerol from SLA 3D printed PEGDA-glycerol structures over time in water environment.

cracking issue when we formulated resins with *S. cerevisiae* and culturing them in YPD at 30 ^{o}C after 3D printing (**Figure 4.9**). Thus, PEGDA-glycerol formulations were used to prepare ELM samples.

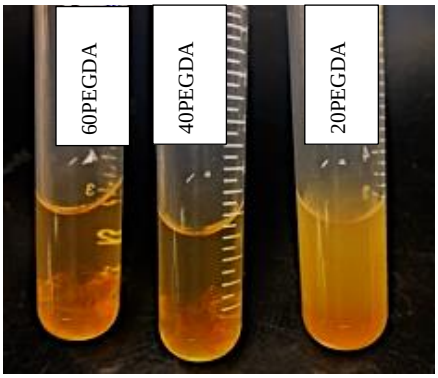

Figure 4.9. 3D printed PEGDA-ELM constructs, cultured in YPD at 30 ^{o}C for 1 day.

4.3.3 *3D printing of ELM and evaluation of polymer cytotoxicity toward S. Cerevisiae*

Previous investigations on ELMs have established that different species of microorganisms are viable in hydrogel matrices after photocuring[1,5,26,111]. However, these organisms have not been investigated for their viability in resins for vat photopolymerization. We 3D printed ELMs on a commercial Form 2 printer using an aqueous resin comprising PEGDA-glycerol, photo initiating

system, and *S. cerevisiae*. The time required to print a construct can be as long as 2 h, thus some of the cells reside in the resin vat for longer periods of time before they are incorporated into printed hydrogel construct. We investigated the toxicity of PEGDA-Gly resin against *S. cerevisiae* cells over this timeframe by using a live/dead assay. **Figure 4.10 a-c** shows live (green) and dead (orange to yellow) cells that remain in the resin after 2 h. *S. cerevisiae* cells showed excellent cell viabilities of 89.4 ± 4.8 %, 87.3 ± 2.3 %, and 87.9 ± 3.5 % for 20PEGDA-5Gly, 40PEGDA-5Gly, and 60PEGDA-5Gly, respectively (**Figure 4.10 d**). Thus, these PEG-based resins show low toxicity toward *S. cerevisiae* cells on the timescale of 3D printing.

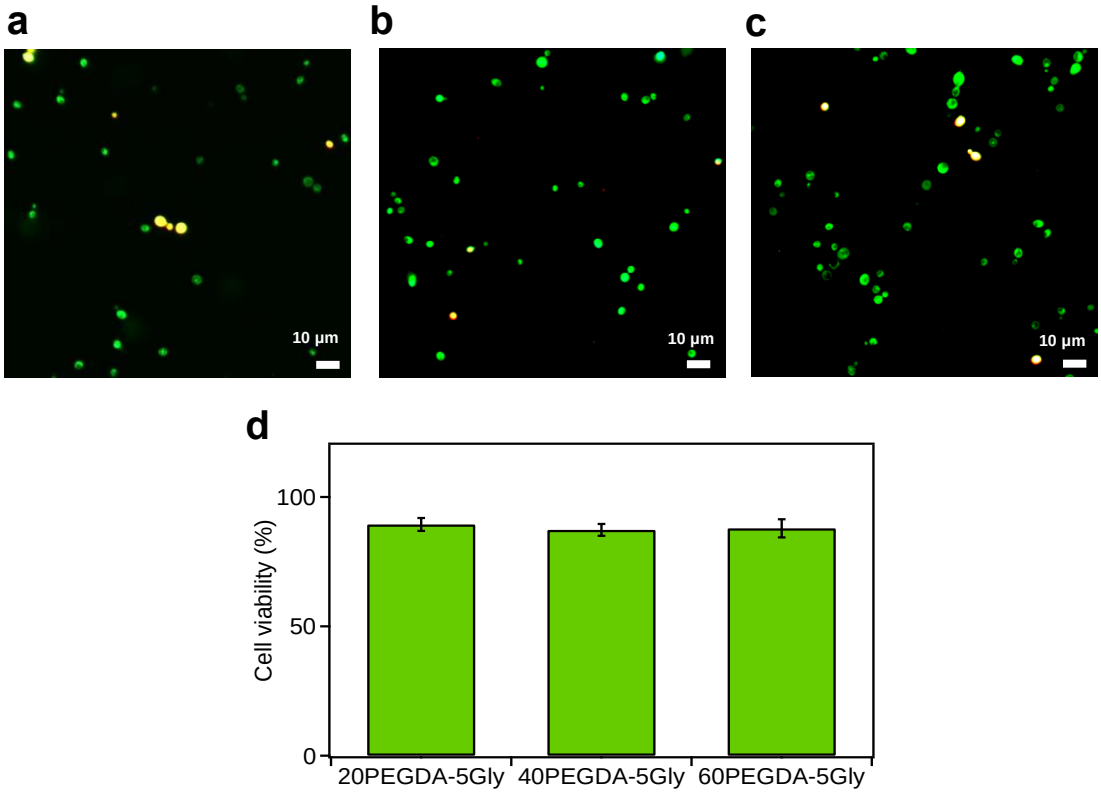

Figure 4.10. Cytotoxicity evaluation of PEGDA-glycerol resin toward *S. cerevisiae*. a-c) Fluorescence images for a) 20PEGDA-5Gly, b) 40PEGDA-5Gly, and c) 60PEGDA-5Gly. Live cells represented in green and dead cells represented in orange - yellow. d) Live and dead cell ratio of *S. cerevisiae* cells in 20PEGDA-5Gly, 40PEGDA-5Gly and 60PEGDA-5Gly formulations. Each data point represents the mean ($n = 3$) and error bars represent standard deviation. Total counted cells 116, 127, and 109 for 20PEGDA-5Gly, 40PEGDA-5Gly, and 60PEGDA-5Gly formulations, respectively.

The *S. cerevisiae* cells encapsulated within the printed hydrogel also exhibited high viability. Scanning electron microscopy (SEM) cross-sectional images of the ELMs showed *S. cerevisiae* cells encapsulated by the polymer matrix (**Figure 4.11 a-c**). Individual *S. cerevisiae* cells are 5 – 10 μm and form colonies via budding of daughter cells.[74] In addition to the presence of cells with a spherical morphology, ellipsoid-shaped cells with buds were also observed (**Figure 4.11 c**). The ovular gyroid shown in Figure 5d was cultured for 21 d. The culture media was changed daily, and the ELM bioreactor was washed with culture media to remove escaped cells. We postulate that the cells closest to the surface of the hydrogel can either escape or bud into the surrounding media. The escaped cells from PEGDA network maintained their viability over this time period as evidenced by the fluorescence microscopy performed after staining with Biotium Live/Dead Yeast staining kit (**Figure 4.11 e**) The viability of escaped cells was found 88% ± 5 with 107 cells counted in different image areas (250 μm^2), sample number, n=4.

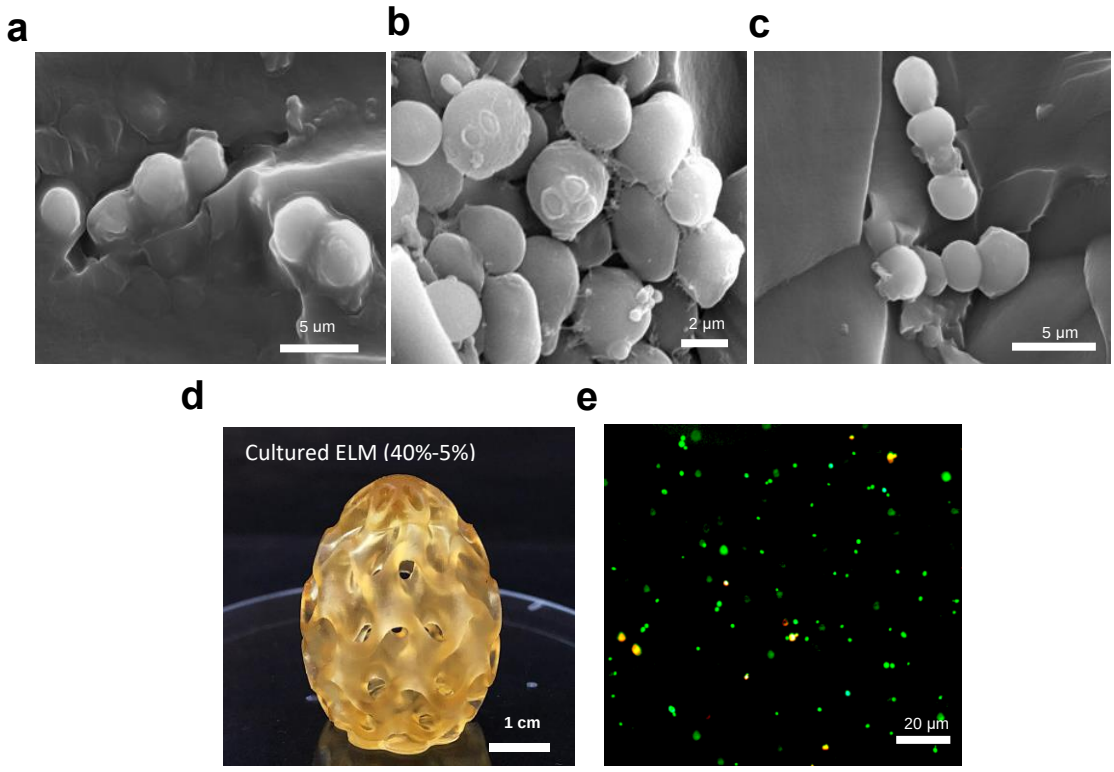

Figure 4.11. *S. cerevisiae* cells in 3D printed ELM bioreactors. a-c) Scanning electron microscopy images of *S. cerevisiae* cells in a) 20PEGDA-5Gly, b) 40PEGDA-5Gly, and c) 60PEGDA-5Gly. d) Optical image of an ELM bioreactor 3D printed in the shape of an ovular gyroid; this ELM was continuously cultured over the course of 21 d. e) fluorescence microscope images of live and dead cells escaped from ELM bioreactor at day 21; live cells represented in green and dead cells represented in orange-yellow.

4.3.4 *Production of betaxanthin from 3D printed ELM bioreactors with different moduli*

The yeast strains were engineered to produce the fluorescent molecular betaxanthins as a marker for cell viability and metabolic potential. As such, we investigated metabolic production of betaxanthin from 3D printed ELMs with varying moduli (**Figure 4.12**). Betaxanthin is an ideal model compound because it is a fluorescent molecule that can be easily detected in the media. The modulus of an extracellular matrix has been reported to affect cellular phenotypes of confined yeast cells in Pluronic F127-based hydrogels[120,121]. To investigate the effect of matrix stiffness on cell proliferation, the 20PEGDA-Gly5, 40PEGDA-Gly5, and 60PEGDA-Gly5 resins were inoculated with identical quantities of betaxanthin-producing *S. cerevisiae* (20 µL of $3x10^4$ cells/mL suspension) and photocured in a well plate. The samples

were cultured for 8 d and then analyzed by confocal microscopy (Figure 12f-h). We observed that *S. cerevisiae* cells encapsulated within PEGDA-Gly matrices exhibited different proliferation behaviors that correlated with the matrix stiffness. A larger number of colonies were formed in the 20PEGDA-5Gly where the modulus was the lowest. As the modulus of the matrix increased (40PEGDA-5Gly and 60PEGDA-5Gly), the number and density of colonies decreased (Figure **4.12 c-h**).

All of the ELMs produced betaxanthin, and the production level was dependent on the cell density. Each of the 3D printed ELMs were cultured for 8 d by submerging the hydrogels in growth media and daily quantifying the betaxanthin present in the media. Since the three different ELM compositions were seeded with the same cell density, the level of betaxanthin production was identical after 1 d. However, the differences in the moduli of the hydrogel matrices led to different levels of production based on the growth and proliferation of the cells. The production levels for each of the ELM formulations was higher at day 8 relative to day 1. 20PEGDA-5Gly, which had the lowest modulus and highest population of yeast colonies produced the most betaxanthin after 8 d.

While the presence of the yeast cells in the PEGDA matrices did not alter the initial compressive moduli, there was a slight decrease after several days of culture (**Figure 4.12 a**). After 8 d of culturing, the compressive modulus of 60PEGDA-5Gly was 9.3 ± 0.5 MPa, 40PEGDA-5Gly was 5.3 ± 0.8 and 20PEGDA-5Gly was 0.7 ± 0. We attribute this change in the matrix stiffness to the hydrolysis of the ester linkages present in the polymer network. It is possible that this hydrolysis can be mediated by peptidases or esterase produced by the yeast cells. Despite the changes we observed in the moduli, the ELM matrices were still mechanically self-supporting and functional as bioreactors.

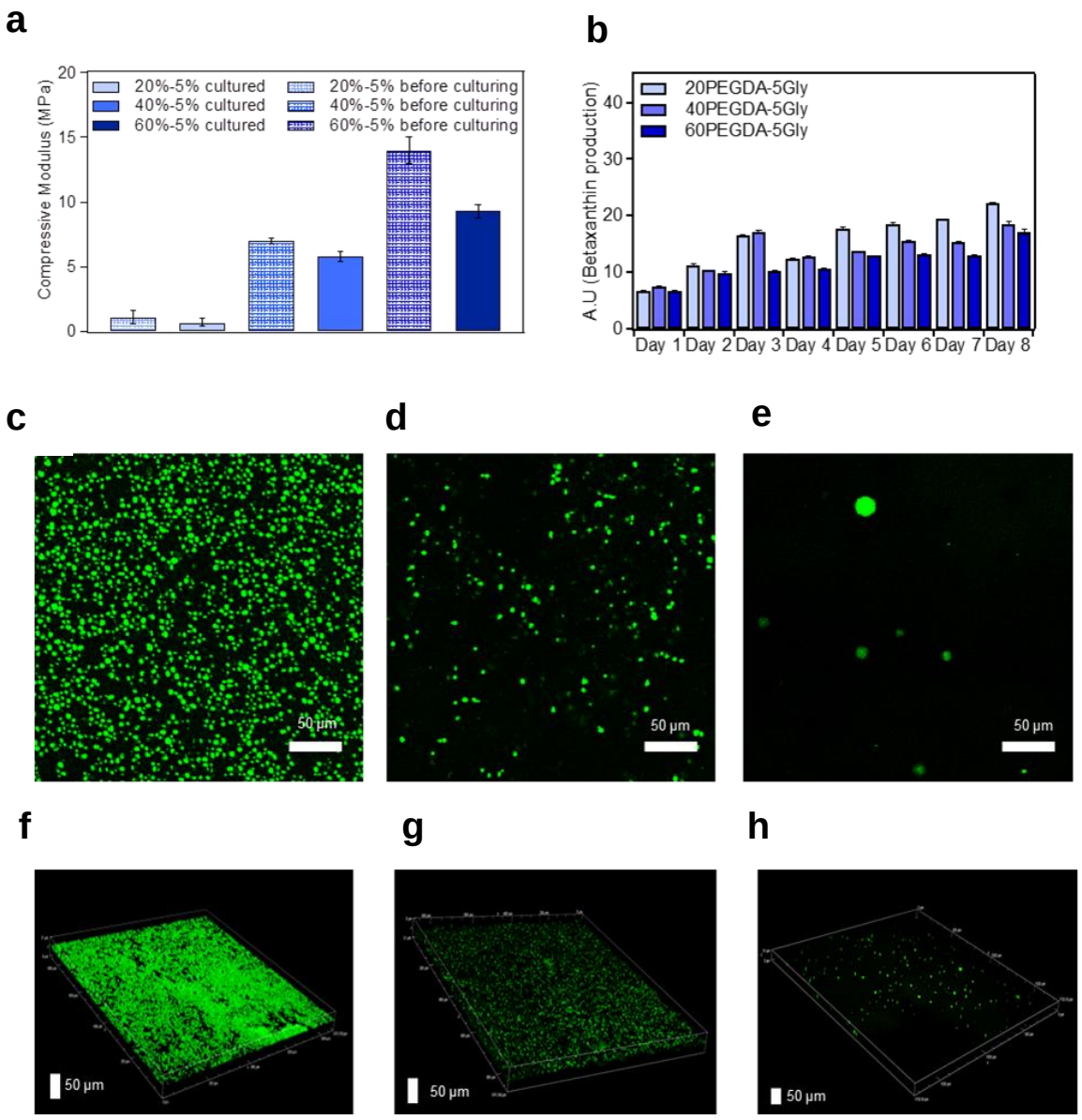

Figure 4.12. Metabolic activity in 3D printed ELM bioreactors. a) Changes of compressive modulus of ELM bioreactor after 8 d production. b) Production of betaxanthin over time for each of the ELM bioreactors. Confocal image of betaxanthin produce *S. cerevisiae* cells in c) 20PEGDA-5Gly, d) 40PEGDA-5Gly, e) 60PEGDA-5Gly after 8 d culturing. 3D visualization of z-stack images of betaxanthin produce *S. cerevisiae* cells in f) 20PEGDA-5Gly, g) 40PEGDA-5Gly, h) 60PEGDA-5Gly after 8 d culturing.

4.4 CONCLUSION

Mechanically stable 3D printed ELM bioreactors were fabricated via vat photopolymerization. We demonstrated that glycerol can toughen PEGDA hydrogels and prevent the brittleness that evolves from osmotic expansion of the hydrogels. ELMs comprising *S. cerevisiae* were fabricated with form factors that were determined by the CAD design. In addition to improving the mechanical characteristics, the presence of glycerol can enhance the resolution of the printed features. The moduli of the printed ELM matrix were determined by the concentration of PEGDA in the resin formulation. The *S. cerevisiae* exhibited excellent viability in the resin formulation and in the printed ELMs. All of the ELM bioreactors maintained betaxanthin production over the course of 8 d. The level of production was determined by the polymer concentration of the matrix, which dictated the growth and proliferation of the cells within the ELM constructs. Taken together, these results open new opportunities for the fabrication of next generation bioreactors for the food, drug, biomedical, and cosmetic industries.

4.5 EXPERIMENTAL SECTION

4.5.1 *Materials*

Polyethylene glycol diacrylate (M_w 700 g/mol), glycerol, sodium persulfate, glutaraldehyde, were purchased from Sigma-Aldrich. Tris(2,2′-bipyridyl) ruthenium(II) chloride hexahydrate, LB broth powder, LB agar powder, yeast extract, peptone, and glucose were obtained from Thermo Fisher Scientific.

4.5.2 *Strains, plasmids, media*

All strains, plasmids, and primers used in this chapter has been explained in Chapter 2.

4.5.3 *Resin formulations*

The resin formulations were prepared with different concentrations of poly(ethylene glycol)diacrylate (PEGDA, M_w 700 g/mol), which included 20 wt%, 40 wt% and 60 wt% with and without glycerol (5 wt%) in aqueous media (water or YPD media). ELM resins were formulated by adding genetically modified *S. cerevisiae* (betaxanthin producing) to the resin. 1 mL of cell suspension contains $3x10^7$ cells/mL was introduced to 20 grams of a resin formulation. A $Ru(bpy)_3Cl$ (0.748 mg/g of resin) - sodium persulfate (2.38 mg/g of resin) photo-initiating system was included in the resin to initiate the polymerization during the printing process. We provide the 20 wt% formulations here with and without glycerol as representative examples.

Preparation of 20 grams of 20PEGDA. 4 grams PEGDA, 1 gram glycerol, 14.2 grams aqueous media (water or YPD media), 400 µl $Ru(bpy)_3Cl$ solution prepared in DI water (0.01496 g $Ru(bpy)_3Cl$ in 400 µl DI water), 400 µl sodium persulfate solution prepared in DI water (0.0476 g sodium persulfate in 400 µl DI water). *Preparation of 20PEGDA-5Gly*. 4 grams PEGDA, 15.2 grams aqueous media (water or YPD media), 400 µl $Ru(bpy)_3Cl$ solution prepared in DI water (0.01496 g $Ru(bpy)_3Cl$ in 400 µl DI water), 400 µl sodium persulfate solution prepared in DI water (0.0476 g sodium persulfate in 400 µl DI water).

4.5.4 *Rheological characterization*

All rheological experiments were performed on a TA Instruments Discovery Hybrid Rheometer-2. To measure the viscosity of each resin, a viscosity versus shear rate experiment was performed using shear rates ranging from 1 to 100 s^{-1}. A 40 mm cone and plate geometry with a cone angle of 1.019°, a solvent trap, and a gap height of 26 µm were used during the analysis. The *in situ* photorheology experiments were performed using acollimated light source (λ = 400 nm, 10 mW cm^2, Thorlabs) that was turned on 120 s after the data accumulation started. The storage and

loss moduli were monitored for a total of 150 s at 1% strain and 6.28 rad/s by using a 20 mm parallel plate and a gap height of 1000 μm. TRIOS software (TA Instruments) was used to collect and analyze data.

4.5.5 *SLA 3D printing of ELM bioreactors*

The constructs were 3D printed in the Open Mode using a Formlabs Form 2 printer with a layer height of 100 μm. CAD models were designed in Autodesk Fusion or downloaded from Thingverse. The printed samples were removed from the build plate, rinsed with DI water, then transferred to culture tubes that contained YPD media (10 g L^{-1} yeast extract, 20 g L^{-1} peptone and 20 g L^{-1} glucose) and cultured in a shaking incubator (225 rpm at 30 °C).

4.5.6 *Thermal analysis*

Thermal analyses were performed in a Mettler Toledo DSC 3+ differential scanning calorimeter (DSC) and TA Instruments Q5000 IR thermogravimetric analyzer (TGA). The DSC scans were performed in the temperature range of –80 to 200 ºC with a scan rate of 10 ºC min^{-1}. All scans were conducted under a N_2 atmosphere, in hermetically sealed aluminium pans. 3D printed constructs were dried at room temperature and 5 and 7 mg of samples were taken from them to conduct DSC and TGA analysis, respectively. The TGA was performed under a N_2 atmosphere over the temperature range from 25 to 600 ºC with a scan rate of 10 ºC min^{-1}. At 100 ºC, a 30 min isotherm was performed to analyze the samples' water content, followed by a temperature increase to 600 ºC to monitor their decomposition temperature.

4.5.7 *Scanning electron microscopy imaging*

A cylindrical disk (x = 10.5 mm, y = 10.5 mm, z = 7 mm) shaped 3D printed ELM constructs were cultured in YPD at 30 ºC for 3 days before taking SEM images of encapsulated

cells. Prior to SEM imaging, samples were fixed, and imaging surfaces were coated with platinum. The samples were incubated in 8 % glutaraldehyde (Sigma-Aldrich) solution for 48 h at room temperature to fix the cells. Then, they were dried by stepwise ethanol dehydration with concentrations of 10, 20, 30, 40, 50, 60, 70, 80, 90 and 100 % (10 min at each concentration). A Leica EM ACE600 was used to coat imaging surface of samples with 4 nm platinum. Images were taken by Sirion XL30 scanning electron microscope with high vacuum and 15 kV an accelerating voltage.

4.5.8 *Live and dead cell analysis*

Live and dead cells were imaged under fluorescence microscopy (EVOS Fluorescent Imaging Microscopy) after staining with Biotium Live/Dead Yeast staining kit according to the procedure provided by the manufacturer.

4.5.9 *Confocal imaging*

The effect of matrix stiffness on cell proliferation was investigated by inoculating S. cerevisiae (20 µL of $3x10^4$ cells/mL suspension) with 200 µL of 20PEGDA-Gly5, 40PEGDA-Gly5 and 60PEGDA-Gly5 resins. S. cerevisiae loaded resins placed in Ibidi 6-well plate and photocured for 5 min under 405 nm. Then 300 µL culture media added to photocured formulations and samples were cultured for 8 days at 30 ^{O}C. Culture media was changed every day. Before confocal imaging, culture media removed form photocured samples and samples washed with PBS at 3 times. Nikon A1R HD25 laser scanning confocal microscope was performed to take cell images.

4.5.10 *Metabolic activity of S. cerevisiae in ELM constructs*

Metabolic activity of ELM samples was determined by monitoring the betaxanthin production over time. 3D printed ELM samples were incubated in YPD media (10 g L^{-1} yeast extract, 20 g L^{-1} peptone and 20 g L^{-1} glucose) with 225 rpm at 30 °C for 8 d. Samples collected from culture media and prior to measurement they centrifuged at 4400 rpm for 10 min, supernatants were collected and placed in a microplate. Thermo Labsystems Fluoroskan Ascent FL Fluorescence Microplate Reader was used to determine betaxanthin fluorescence intensity at excitation/emission: 485 nm / 520 nm. The culture media was refreshed each day.

4.5.11 *Degree of swelling (q) and water uptake (WU) (%)*

The degree of swelling was determined by monitoring the volume change of dried samples after overnight incubation in DI water. Samples were printed as cylindrical disks (x = 10.5 mm, y = 10.5 mm, z = 7 mm) and dried in the vacuum oven overnight. The dried samples were then incubated in DI water overnight, and the change in volume of hydrated and rehydrated states were calculated using measurements made with a digital caliper. The degree of swelling was calculated using the following equation 4.1:

$$q = \frac{(Rehydrated\ volume - Dried\ volume)}{(Dried\ volume)} \quad (4.1)$$

To determine the water uptake capacity (%), cylindrical disks (x = 10.5 mm, y = 10.5 mm, z = 7 mm) were dried in a vacuum oven overnight, and then submersed in water overnight. The mass change of hydrated and rehydrated states was compared to calculate water uptake (WU) (%) using the following equation 4.2:

$$WU\ (\%) = \frac{(Rehydrated\ mass - Dried\ mass)}{(Rehydrated\ mass)} x100 \quad (4.2)$$

4.5.12 *Mechanical characterization*

The compressive modulus of each hydrogel was determined using a universal testing machine. Each resin formulation was 3D printed as a cylindrical disk (x = 10.5 mm, y = 10.5 mm, z = 7 mm) and the hydrogel samples were tested immediately after collecting from the build plate. A Newton Test Machine electromechanical test frame with 1 kN load cell and a crosshead rate of 1.3 mm/min was used during compression experiment. The compressive modulus was calculated based on the slope of the stress (kPa)-strain(mm/mm) curve where 0.05 (mm/mm) - 0.1 (mm/mm) of strain region.

4.5.13 *Statistical analysis*

Igor Pro (Version 8.04) software was used to compare statistical differences. Differences were analyzed by One-way ANOVA, Welch Test. A p value of < 0.05 was chosen to determine significant differences. The standard deviations (± S.D.) of replicates were calculated in Excel.

CHAPTER 5. SMART THERAPEUTIC ELMS: A NEW APPROACH TO TREAT INFLAMMATION IN THE GASTROINTESTINAL TRACT

5.1 ABSTRACT

Establishing long-term treatment approaches for Inflammatory Bowel Disease (IBD), where therapy is localized to the site of inflammation and conditionally activated during active phases, has transformative potential to improve patient's lives by improving safety and effectiveness compared to current options. Probiotics engineered by genetic reprogramming to release therapeutic compounds in response to inflammatory biomarkers hold significant promise for conditional therapeutic outcomes. The use of these probiotics in the fabrication of 3D printed engineered living materials such as medical stents offer a significant opportunity to enable long-term, localized delivery, but have yet to be developed. In this study, 3D printed probiotic-ELM constructs were fabricated to detect inflammatory biomarkers and respond through the secretion of anti-inflammatory small molecules. Clinically significant biomarker levels were successfully identified, with robust production observed in simulated intestinal and colonic environments. Furthermore, safety and efficacy were demonstrated in the treatment of inflammation within in vitro models by the engineered living materials (ELMs). Looking ahead, we envision the ELM device as a closed-loop therapeutic modality, aiming to initiate and sustain remission in IBD patients over extended durations, representing a transformative shift in IBD management.

5.2 INTRODUCTION

Inflammatory bowel disease (such as Crohn’s disease and ulcerative colitis), irritable bowel syndrome, and colorectal cancer pose significant public health concerns, impacting millions

of Americans annually[122,123,124]. Current treatments involve a combination of medication, dietary adjustments, and lifestyle management[124]. Although delivering drugs orally is typically the most convenient method for patients, oral therapeutics focusing on the intestines necessitate drug delivery systems that (i) avoid premature release in the upper gastrointestinal tract, (ii) incorporate a trigger mechanism for timely drug release, and (iii) ensure the prescribed dose is administered over the appropriate duration[125]. Approaches facilitating precise drug delivery to the intestine encompass the use of prodrugs, pH-responsive polymer coatings, selectively biodegradable polymers, timed release systems, and osmotic-controlled systems[126,127]. The distribution of affected sites in inflammatory bowel disease and other intestinal conditions varies both with the disease and among individuals. Moreover, orally administered drugs may result in undesired absorption into the systemic circulation, causing side effects. Consequently, there is a preference for implantable drug delivery devices for localized administration, such as stents, patches, and microneedle devices[127,128]. These devices can be positioned near affected areas to provide precise and targeted therapeutic delivery.

One of the main limitations of traditional polymeric-based drug delivery devices is the limited amount of drugs that can be loaded into these systems[127]. The other challenges related to maintaining the drug stability from manufacturing to shelf-lite to application and drug release from devices[129]. As artificial living systems, ELMs have a capability to be a programmable bioproduction platform. At this point, ELMs can be designed for therapeutic production in which this production can happen in disease areas *in situ* way by 3D-printed ELM medical devices for GI tract.

Probiotics are crucial to maintain a healthy gut environment[130,131]. Indeed, recent studies showed that probiotics can effectively help to treat inflammation diseases such as inflammatory

bowel disease[132,133], colorectal carcinogenesis[134], and ulcerative colitis[135]. Thus, there has been increasing focus on combining advancements in synthetic biology toolkits with genetically modifiable probiotic chassis. For instance, probiotic *E. coli* Nissle 1917 (EcN) is one of the engineered microorganisms for this aim[48,52,136]. Recent studies focused on managing Inflammatory Bowel Disease (IBD) have showcased EcN systems with the ability to detect transient IBD biomarkers in vivo, such as reactive oxygen species (ROS)[9] and nitric oxide (NO)[10]. On the other hand, probiotic diagnostic and therapeutic methods face notable limitations in achieving sustained delivery to diseased tissues. Strains administered as free cells encounter viability challenges in the harsh pH of the stomach and the high bile salt content of the small intestine[138]. Furthermore, EcN doesn't typically colonize the gut of adult humans without antibiotic pretreatment, thus frequent dosing of free cells is essential to maintain effectiveness[139].

Utilizing polymer matrices to encapsulate engineered probiotics and create Engineered Living Material (ELM) as a therapeutics platform provides a protective barrier against the harsh gut environment. Additionally, it may establish a synthetic niche, allowing living therapeutics to reside in the gut for extended periods without the need to outcompete native microbiome populations for colonization. Natural biopolymers like alginate, cellulose, and chitosan are prevalent in traditional probiotic-ELM formulations[47,48,50]. However, these polymer matrices are challenging to process in additive manufacturing techniques to obtain 3D form factors as ELM therapeutic medical devices without synthetic modification of the polymer components.

Here, a therapeutic ELM platform was fabricated to treat inflammation in intestine and colon area with *in situ* production and continuous delivery of anti-inflammatory agents via engineered probiotic release (**Figure 5.1 a**). ELM were formulated with genetically modified EcN and PEGDA-glycerol matrix. The mechanical characterization and compatibility of PEGDA-glycerol matrix in ELM formulations was discussed in Chapter 4. Two genetically modified EcN strains were engineered to produce tryptamine and β-carboline, both noted for anti-inflammatory activity in *in vitro* models (**Figure 5.1 b**). The probiotic delivery capacity, and antiinflammation

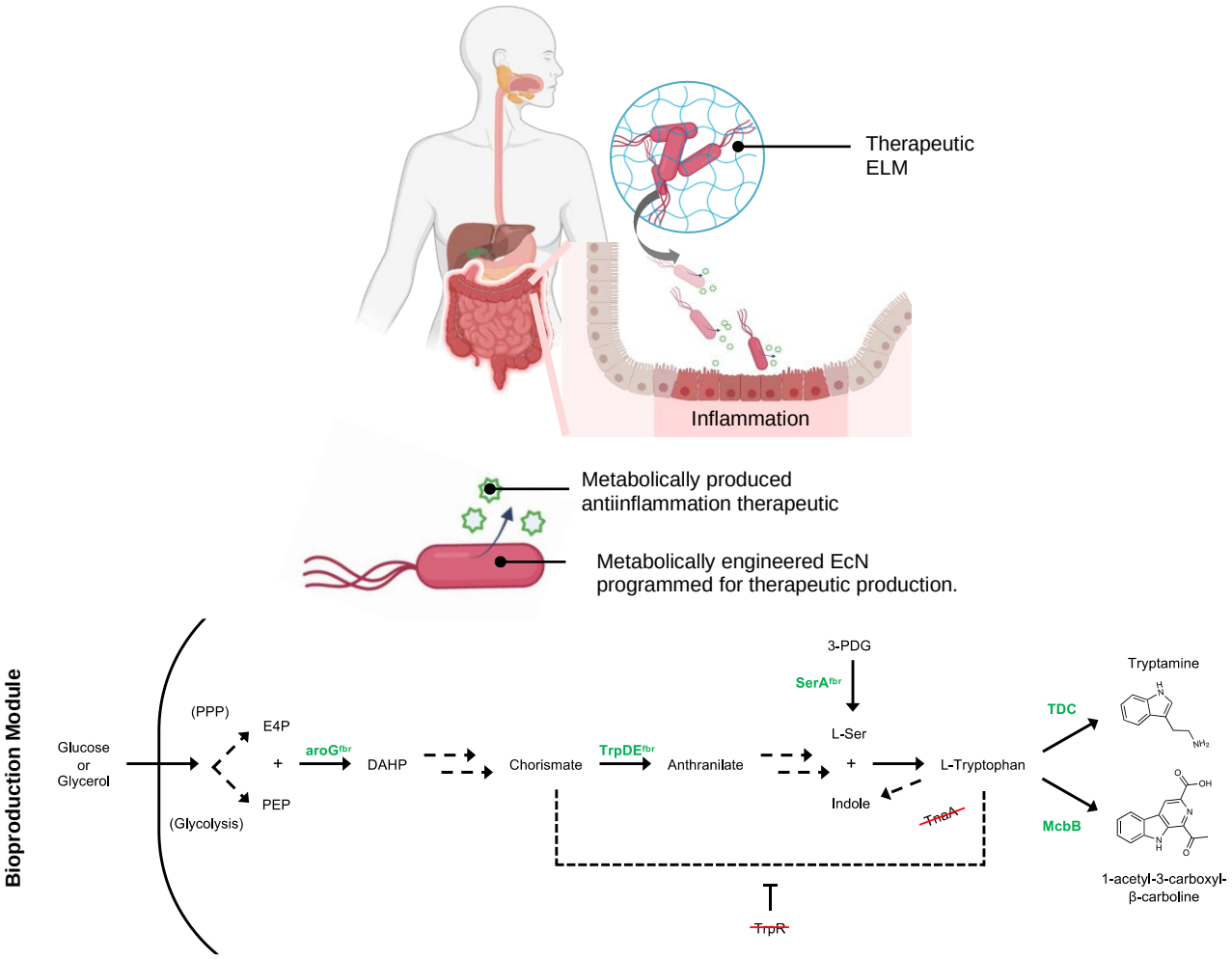

Figure 5.1. General scheme of probiotic ELM for treatment of inflammations in gut. a) probiotic ELM maintain therapeutic cell delivery, metabolically engineered EcN programmed for antiinflammation therapeutic production. B) Bioproduction module of metabolically engineered EcN.

bioproduction performance of probiotic-ELM form factors were evaluated in simulated gastrointestinal fluid models These models mimic the intestine and colonic fluids in feed and fasted state and incubated at 37 ^{o}C with shaking motion at 220 rpm (**Figure 5.2**). In the further step of this study, an inflammation-sensing probiotic ELM platform was fabricated. To do that, EcN engineered to sense the inflammatory biomarker nitric oxide (NO) and respond via secretion of anti-inflammatory small molecules, tryptamine and β-carboline. Bioproduction of this platform was also identified in different simulation fluids (**Figure 5.2**) with the presence of various NO

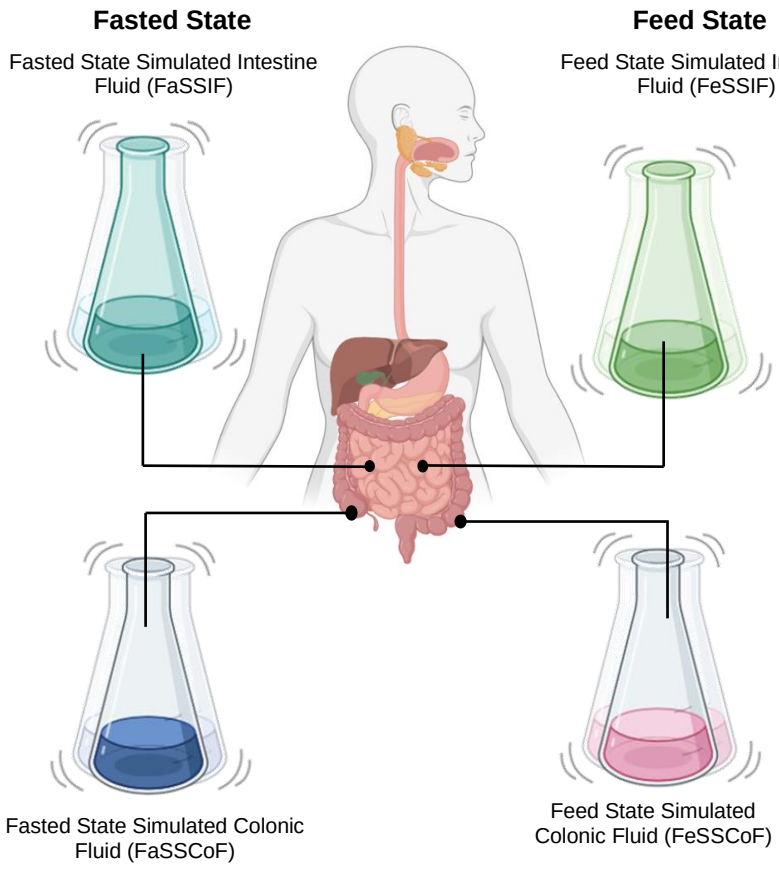

Figure 5.2. Simulated GI models studied in this chapter.

level which were reflected the level of inflammation. The antiinflammation performance of the NO-responsive probiotic platform was evaluated by *in vitro* cell models including RAW-2 and Caco-2 cell lines followed by the determination of cytokine levels including IL6 and IL8. The

findings present a proof-of-concept for a resilient ELM device with the capability for long-term, closed-loop sensing, and therapeutic delivery within the intestine. This holds promise for establishing and maintaining remission in patients with IBD.

5.3 RESULT AND DISCUSSION

5.3.1 *Cell Release from Probiotic-ELM device and Therapeutic Production Capacity in Simulated Gut Fluids*

Probiotic-ELM devices are intended to be administered at the end of the small intestine or within the colon, depending on the specific IBD application. Thus, it is crucial to evaluate the therapeutic performance of these devices in the intestine and colon. *In vitro* GI models including stability studies in biorelevant media are common methods that serve to facilitate our understanding of how therapeutics work and dissolve and potentially be absorbed in the fluid in the upper intestine and/or colon[140]. In this study, cell release capacity and therapeutic production performance of probiotic-ELM devices was identified in four different simulated gut fluids namely Fasted State Simulated Intestine Fluid (FaSSIF), Feed State Simulated Intestine Fluid (FeSSIF), Fasted State Simulated Colonic Fluid (FaSSCoF), Feed State Simulated Intestine Fluid (FeSSCoF) (**Figure 5.2**). We fabricated probiotic-ELM form factors by using genetically engineered EcN and PEGDA-glycerol matrix, then processed the formulation in an SLA 3D printer. Lithium phenyl-2,4,6-trimethylbenzoylphosphinate (LAP) was used as a photoinitiator. EcN cells embedded in PEGDA-glycerol matrix via vat photo-polymerization. **Figure 5.3** shows an example of a probiotic-ELMs that was printed in the shape of a stent shape. Then, the probiotic-ELM stents were placed in different simulation fluids to assess their therapeutic performance.

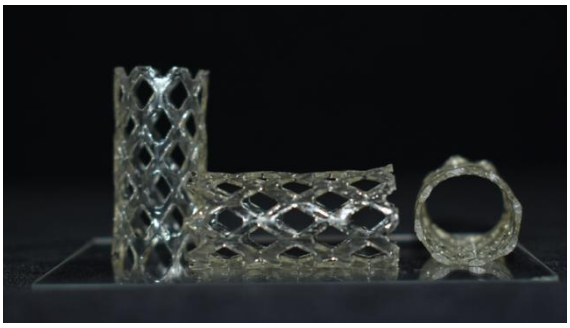

Figure 5.3. SLA 3D printed probiotic-ELM in stent shape.

First, we evaluated cell release and the viability of the released cells from probiotic-ELM constructs in FaSSIF and FeSSIF were evaluated. Constructs were also cultured in LB as control group (**Figure 5.4 a**). Then, the samples were collected from the media and seeded on agar plates to identify the released cells from probiotic-ELM constructs to simulation fluids (**Figure 5.4**). The poor survival rate of probiotics and colonization resistant in gut are main limitations to use probiotics as "therapeutic" agents[47,48,137-139]. Thus, probiotic-ELM devices have the potency to be a continuous probiotic release platform. Agar plating studies showed that EcN cells were released from LB and FaSSIF media from probiotic-ELM constructs. Their ability to colonize when seeded on agar plates shows that these cells can maintain their viability after being released from ELM structures (**Figure 5.4 a, b**, **d**). On the other hand, no cell growth was observed in samples placed in FeSSIF and FeSSCoF (**Figure 5.4 c**, **e**). Feed state simulation fluids representing the post-meal state of intestine and colon fluids indicate an elevation in surfactants, specifically bile salts, upon consuming a meal. Bile salts act as a biological detergent, comprising bile acids conjugated with glycine or taurine which are facilitating the emulsification and solubilization of lipids. This crucial function underscores their essential role in the digestion of fats. While probiotics exhibit bile salt hydrolase activity[141], they often possess low tolerance to elevated bile salt concentrations[138,139,142].

Consequently, in feed state simulation fluids, a high bile salt concentration led to the death of EcN cells if they were released from the probiotic-ELM construct. (**Figure 5.4 c, e**).

The viability of released EcN cells from probiotic-ELM to simulated intestine fluids have also been identified by imaging of live (represents as green) and dead (represents as red) cells by fluorescence microscopy. Results compatible with agar plating findings as high number of live cells were imaged in LB and FaSSIF. No cells, either live or dead cells, were imaged in the sample of probiotic-ELM formulated with tryptamine producing EcN incubated in FeSSIF (**Figure 5.5 c**) and a few live cells were imaged in the samples of probiotic-ELM formulated with beta-carboline producing EcN incubated in FeSSIF (**Figure 5.5 c, f**).

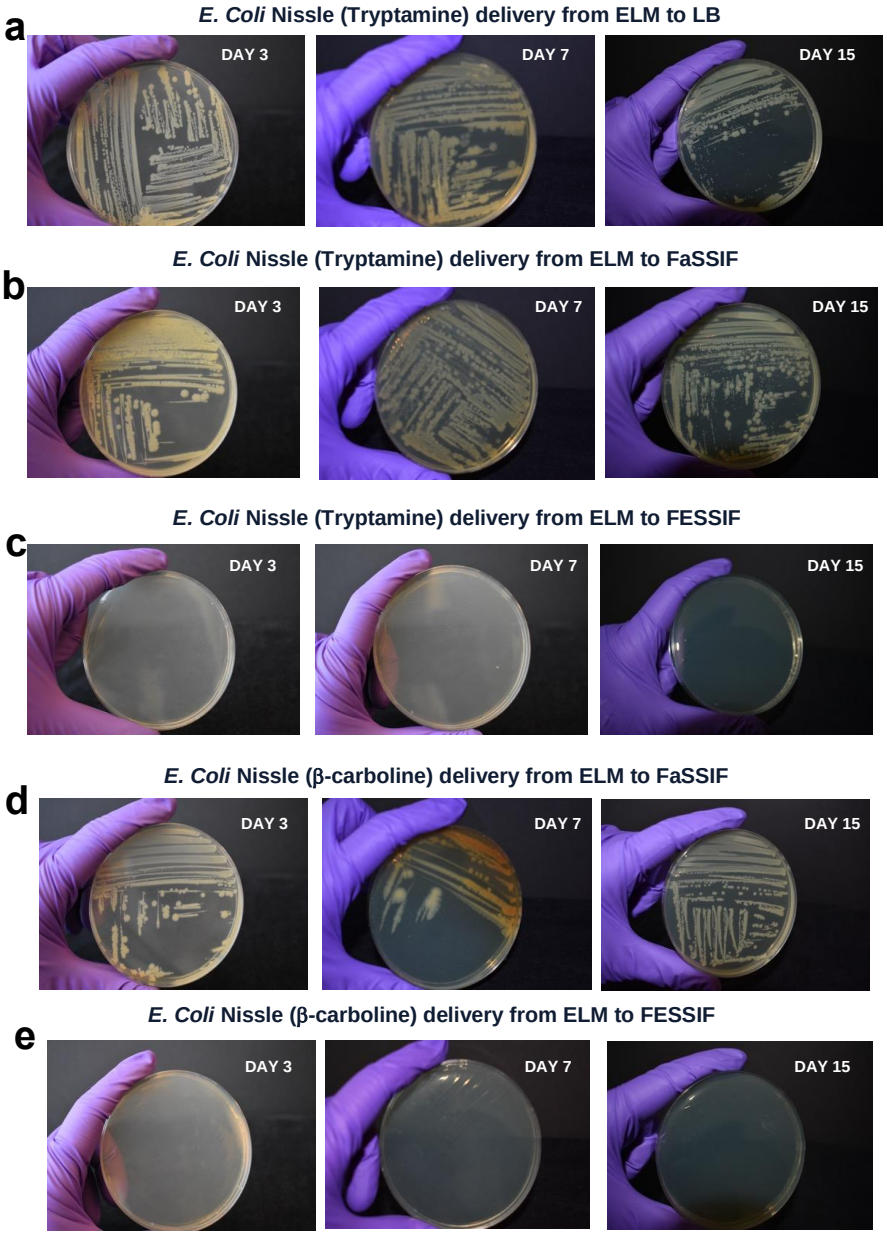

Figure 5.4. Agar plate images show EcN colonies which the cells release from probiotic-ELM devices to LB media and simulated intestine fluids and seed to agar plates. Samples were collected at different time points as follows probiotic-ELM cultured at 3 days, 5 days, and 15 days in simulated intestine fluids. a-c) EcN engineered for tryptamine production was used to fabricate probiotic-ELM, images show EcN delivery form ELM to LB, FaSSIF and FeSSIF, respectively. d-e) EcN engineered for β-carboline production was used to fabricate probiotic-ELM, images show EcN delivery form ELM to LB, FaSSIF and FeSSIF, respectively.

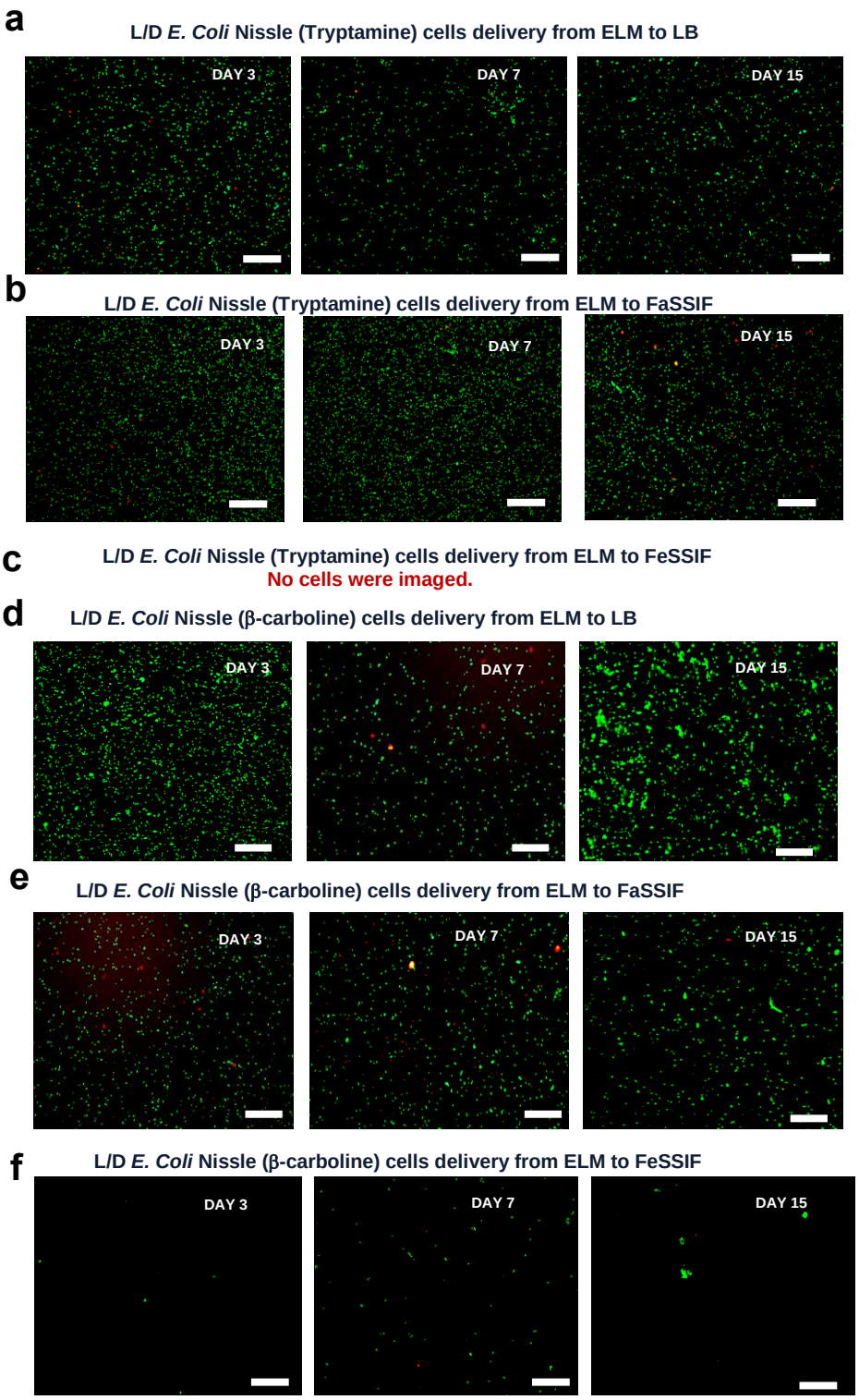

Figure 5.5. Fluorescence microscopy images of live (green) and dead (red) EcN cells which the cells release from probiotic-ELM devices to LB media and simulated intestine fluids. Samples were collected at different time points as follows probiotic-ELM cultured at 3 days, 5 days, and 15 days in simulated intestine fluids. a-c) EcN engineered for tryptamine production was used to fabricate probiotic-ELM, images show live and dead EcN cells delivery form ELM to LB, FaSSIF and FeSSIF, respectively. d-e) EcN engineered for β-carboline production was used to fabricate probiotic-ELM, images show live and dead EcN cells delivery form ELM to LB, FaSSIF and FeSSIF, respectively. Scale bar is 100 μm.

The therapeutic production performance of probiotic ELM in simulated intestine fluids over 7 days are shown in **Figure 5.6**. Due to the more favorable conditions in LB media for EcN,

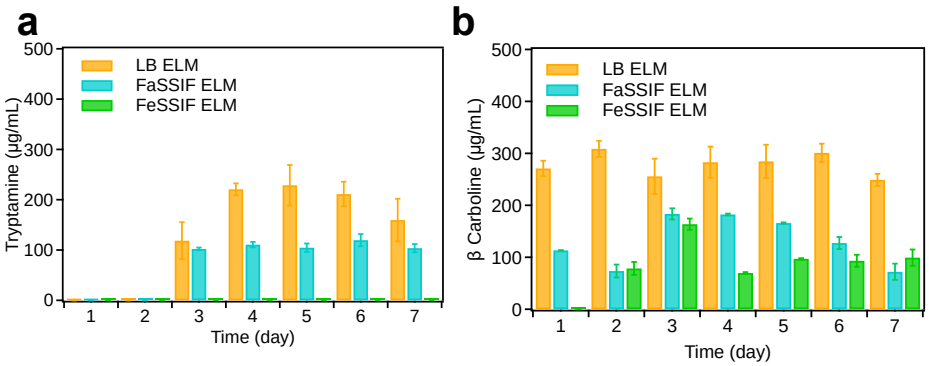

Figure 5.6. Therapeutic, tryptamine and β-carboline, production performance of probiotic-ELM constructs in LB, FaSSIF and FeSSIF over 7 days. Data are mean ± SD.; n=3 biological replicates.

the bioproduction level is higher compared to simulated gut fluids. Tryptamine production in probiotic-ELMs became detectable after 3 days of culturing in LB and FaSSIF. However, no tryptamine was observed in FeSSIF in these samples (**Figure 5.6 a**). β-carboline production started after 1 day culturing in LB and FaSSIF and continued for 7 days. Notably, starting from day 2, a substantial amount of β-carboline was also identified in probiotic-ELM samples cultured in FeSSIF (**Figure 5.6 b**). The continuous β-carboline production over 7 days in FeSSIF, with minimal cell leakage (**Figures 5.4 e, 5.5 f**), demonstrated the protective role of the polymer matrix for embedded EcN cells against adverse FeSSIF conditions. Additionally, it created a suitable environment for their proliferation, as evidenced by the onset of β-carboline production on day 2 (**Figure 5.6 b**), potentially linked to an increase in EcN cell numbers within the ELM polymer matrix. To confirm that, β-carboline producing EcN cells were imaged in ELM matrix which

incubated in FeSSIF for 2 days, free EcN cells incubated in same conditions were imaged as control (**Figure 5.7**).

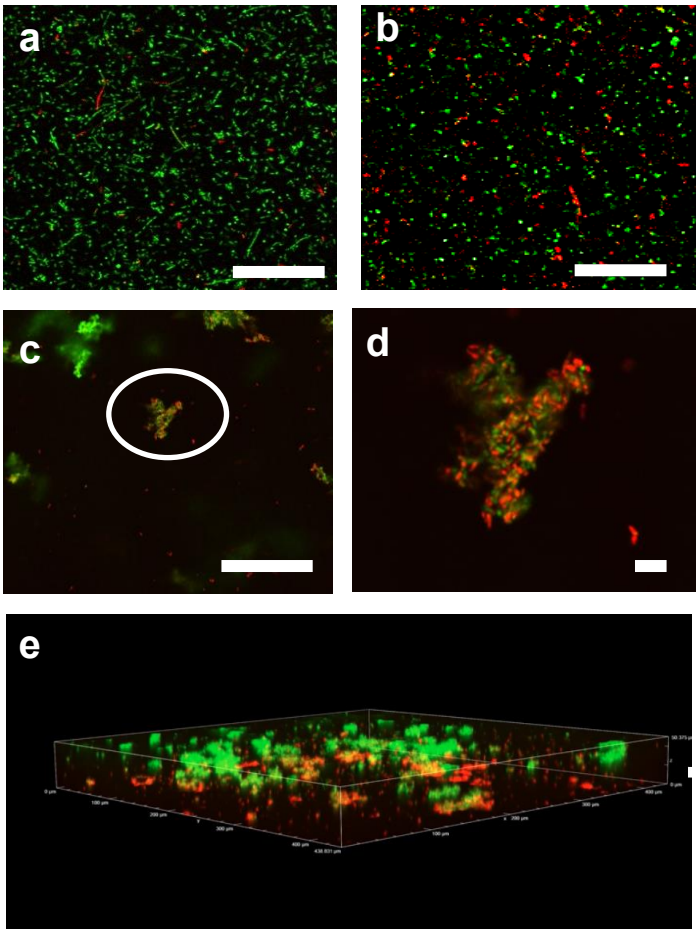

Figure 5.7. Confocal microscopy images of β-carboline producing EcN cells. a, b) Free EcN cells in FaSSIF and FeSSIF, respectively. c) β-carboline producing EcN cells in ELM hydrogel matrix (a tough hydrogel matrix formed by PEGDA-Glycerol). d) Higher magnification images of cell clustered marked with white circle in Fig 7c. e) 3D visualization of z-stack images of β-carboline producing EcN cells in ELM hydrogel matrix. Scale bar is 100 μm.

Z-stack imaging was performed starting at the bottom of the sample through the inner region up to 50 μm (**Figure 1.7 e**). Confocal images demonstrate that EcN cells form clusters in ELM polymer matrix, in **Figure 2.7 d** one of the cell clusters in ELM matrix is shown. Dead cell clusters were observed in areas close to the outer region, potentially due to the diffusion of bile salts in that

region. Conversely, a substantial number of live cell clusters were observed in the inner regions (**Figure 3.7 e**).

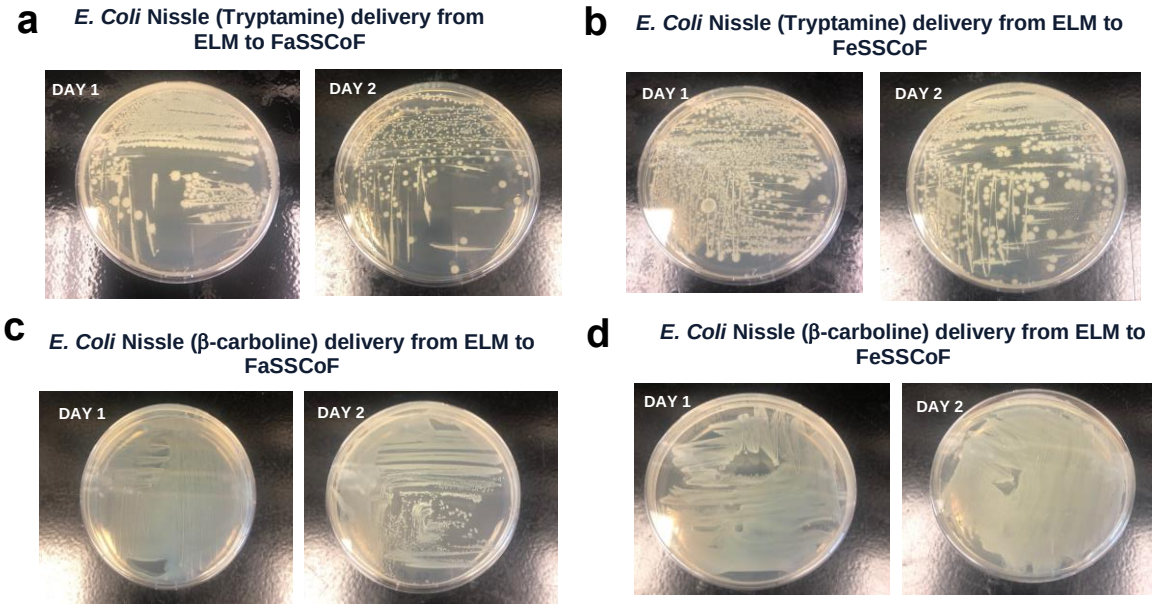

Figure 5.8. Agar plate images show EcN colonies which the cells release from probiotic-ELM devices to LB media and simulated colonic fluids and seed to agar plates. Samples were collected at different time points as follows probiotic-ELM cultured at 1 day and 2 days in simulated colonic fluids. a-b) EcN engineered for tryptamine production was used to fabricate probiotic-ELM, images show EcN delivery form ELM to FaSSCoF and FeSSCoF, respectively. c-d) EcN engineered for β-carboline production was used to fabricate probiotic-ELM, images show EcN delivery form ELM to FaSSCoF and FeSSCoF, respectively.

The viability of released cells from probiotic-ELM constructs and the therapeutic production by these constructs were also evaluated in feed and fasted state simulated colonic fluids. Colony formation of released EcN cells were confirmed by agar plating (**Figure 5.8**). Viability of EcN cells post-release was assessed using Live/Dead staining and fluorescence microscopy images (**Figure 5.9**). No dead cells were detected in either FaSSCoF or FeSSCoF. The elevated live cell ratio in these samples, as opposed to intestinal fluid, may be linked to lower bile salt concentration and higher pH in colonic fluids[138,139,142].

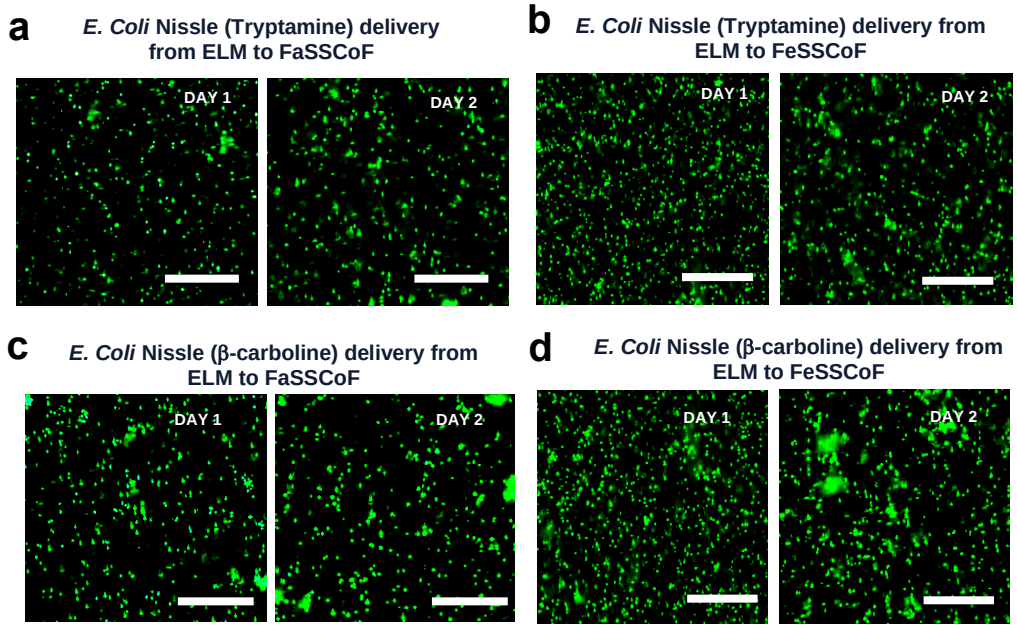

Figure 5.9. Fluorescence microscopy images of live (green) and dead (red) EcN cells which the cells release from probiotic-ELM devices to simulated colonic fluids. Samples were collected at different time points as follows probiotic-ELM cultured at 1 day, and 2 days. a-b) EcN engineered for tryptamine production was used to fabricate probiotic-ELM, images show live (green) and dead (red) EcN cells delivery form ELM to FaSSCoF and FeSSCoF, respectively. c-d) EcN engineered for β-carboline production was used to fabricate probiotic-ELM, images show live (green) and dead (red) EcN cells delivery form ELM to FaSSCoF and FeSSCoF, respectively. Scale bar is 100 μm.

Continuous therapeutic production performance of probiotic-ELM constructs in feed and fasted state colonic fluids are represented in **Figure 5.10 a, b**. Probiotic-ELM constructs showed at least 50 μg/mL therapeutic compound (tryptamine and β-carboline) production over 7 days in both feed and fasted state simulated colonic fluids (**Figure 5.10 a, b**). Tryptamine and β-carboline production level have also monitored in oscillated states between fasted and feed state simulated colonic fluids. Probiotic-ELM structures were incubated in FaSSCoF and the simulation media was alternated between fasted and fed state every 24 hours for 5 days. The oscillatory simulated model showed a similar trend as the stable simulated model as probiotic ELM constructs continued to produce therapeutics (**Figure 5.10 c, d**).

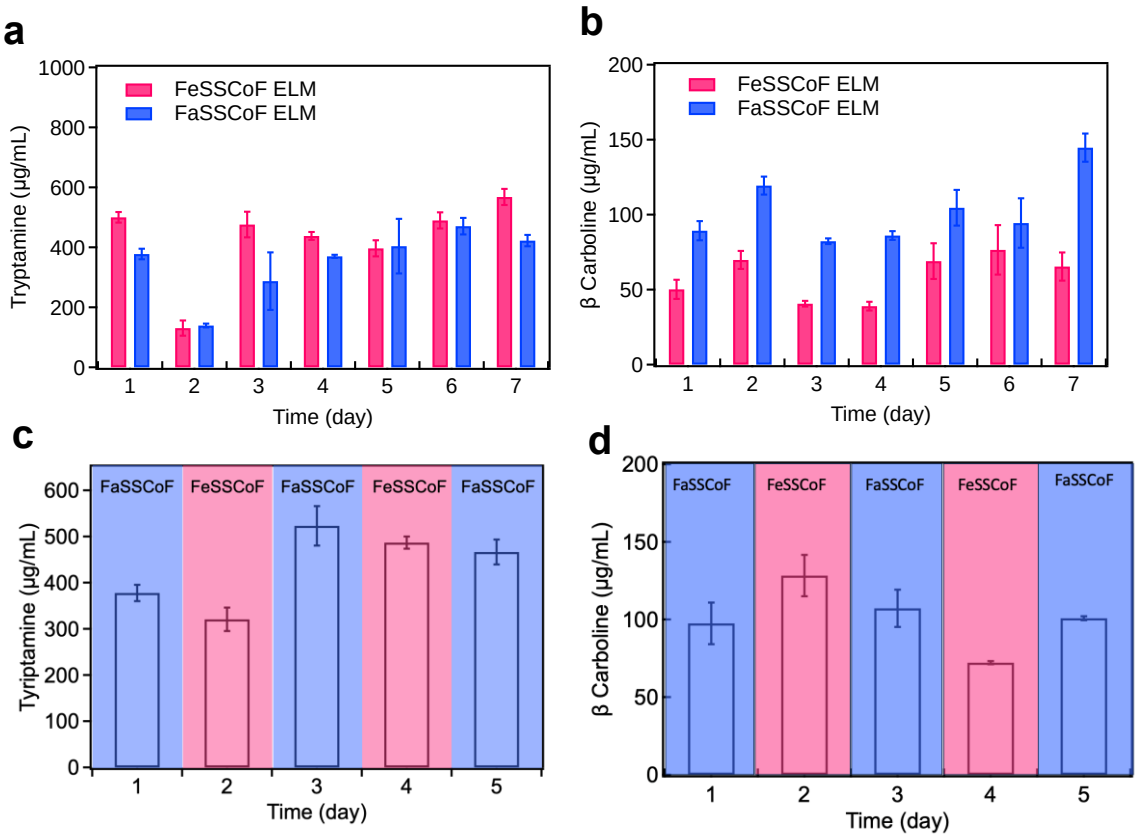

Figure 5.10. Therapeutic, tryptamine and β-carboline, production performance of probiotic-ELM constructs in colonic fluids. a-b) Tryptamine and β-carboline production levels in FaSSCoF and FeSSCoF over 7 days. c-d) Tryptamine and β-carboline production in oscillated states. Data are mean ± SD.; n=3 biological replicates.

In simulated conditions mimicking the intestine and colon fluids, robust production was observed in probiotic-ELM constructs, indicating their potential for effective *in vivo* deployment. Particularly under colonic conditions, where the ELM device was anticipated to be most likely utilized for IBD treatment, a minimum of ~50 µg/mL β-carboline and ~150 µg/mL tryptamine were consistently produced (**Figure 5.10 a, b**). These concentrations exceed the required levels for treating inflammation, as determined in *in vitro* macrophage models[143,144]. Furthermore, the structural integrity of PEGDA-ELM scaffolds persisted for a minimum of one month in SSIF (**Figure 5.11**), emphasizing their potential for use as a durable implantable device in the intestine.

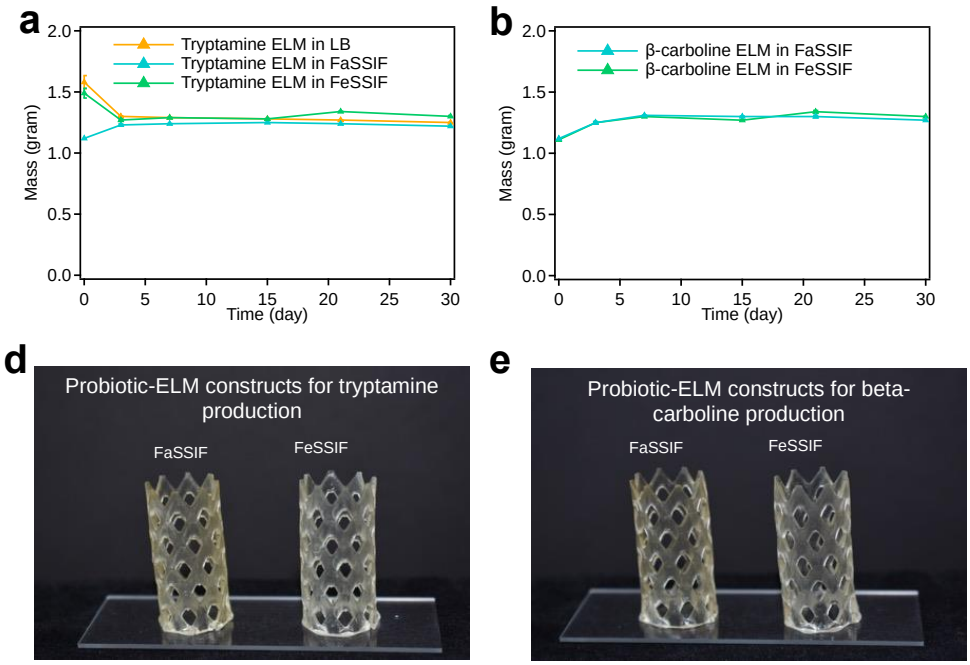

Figure 5.11. Mass change of probiotic-ELM constructs in LB, FaSSIF and FeSSIF over 30 days. a-b) Mass change of probiotic-ELM designed for tryptamine and β-carboline production, respectively. d-e) Optical images of probiotic-ELM constructs after one month incubation in FaSSIF and FeSSIF.

5.3.2 *Development of Probiotic-ELMs that Secrete Anti-Inflammatory Compounds in Response to Inflammatory Biomarkers*

Upon confirming that probiotic-ELM constructs which were formulated with engineered EcN strains could produce anti-inflammatory compounds in simulated gut media, these strains were further engineered for the production of these compounds in response to inflammatory

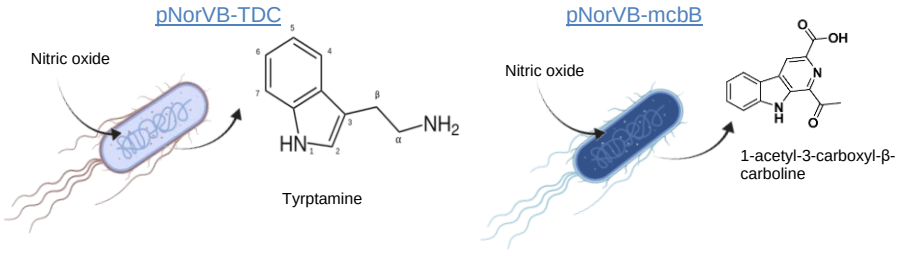

Figure 5.12. NO-responsive EcN strains which produce tryptamine and β-carboline as a response of NO.

biomarkers. Nitric oxide (NO) was chosen as inflammation biomarker and EcN strains were engineered to sense NO and produce either tryptamine or β-carboline in response (**Figure 5.12**) NO-responsive tryptamine producing EcN named with pNorVβ-TDC, and NO-responsive β-carboline producing EcN named with pNorVβ-McbB (**Figure 5.12**). The clinically relevant NO thresholds for IBD encompass >17.4 μM for active ulcerative colitis[143] and >14.0 μM for active Crohn's Disease[144]. Therefore, the therapeutic production performance of NO-responsive probiotic-ELMs was conducted in the presence of 15-100 μM NO. In colonic conditions, a correlation was observed between NO levels and the production of therapeutics in free pNorVβ-TDC, pNorVβ-McbB, and probiotic-ELMs containing these strains (**Figure 5.13 e-h**). Increased NO presence led to higher therapeutic production by EcN cells. However, this trend was not obsevered in intestinal fluids, particularly in FeSIF samples (**Figure 5.13 a-d**). These results align with the findings of constitutive therapeutic production in probiotic-ELMs (**Fig 5.10 a, b**), suggesting that high bile salt concentration and lower pH in fed-state intestinal fluids may impact the viability of engineered EcN strains and therefore therapeutic production performance.

5.3.3 *Evaluating the cytotoxicity, anti-inflammation response, and permeability of therapeutics produced by NO-responsive probiotic-ELMs by in vitro cell models*

Over the past decades, the Caco-2 cell line derived from human colon adenocarcinoma has served as a valuable model for studying toxicity, absorption, and metabolism in the context of the intestinal barrier. Through spontaneous morphological and biochemical differentiation during routine in vitro culture, Caco-2 cells develop features akin to intestinal cells, including a microvilli structure, brush border, tight junctions, and the ability to secrete hydrolases and synthesize carrier transport systems for various substances like sugar, amino acids, and drugs[145-148]. The alamar blue assay was utilized to evaluate the cytotoxicity of engineered EcN[149]. The assay utilizes the

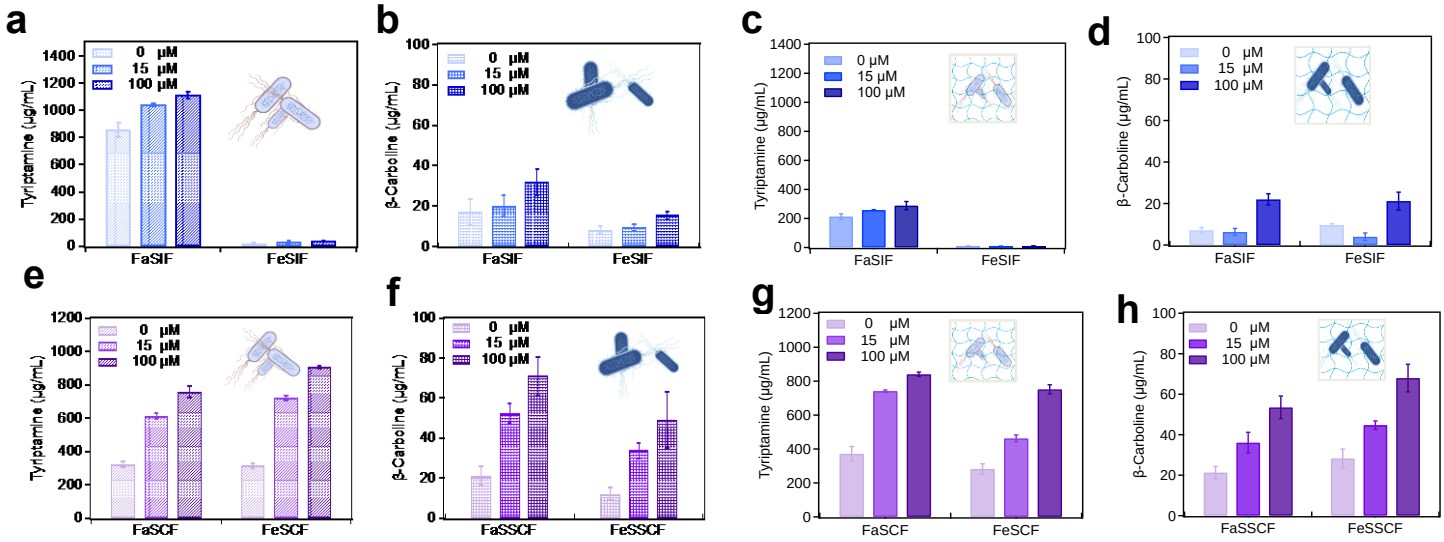

Figure 5.13. Therapeutic production performance of NO-responsive EcNs and probiotic-ELMs in simulated gut fluids. a-b) Tryptamine and β-carboline production levels of free pNorVβ-TDC and pNorVβ-McbB cells in simulated intestine fluids as a response of NO concertation, respectively. c-d) Tryptamine and β-carboline production levels of probiotic-ELMs formulated with pNorVβ-TDC and pNorVβ-McbB cells in SIF as a response of NO concertation, respectively. e-f) Tryptamine and β-carboline production levels of free pNorVβ-TDC and pNorVβ-McbB cells in simulated in colonic fluids (SCF) as a response of NO concertation, respectively. c-d) Tryptamine and β-carboline production levels of probiotic-ELMs formulated with pNorVβ-TDC and pNorVβ-McbB cells in SCF as a response of NO concertation, respectively. Data are mean ± SD.; n=3 biological replicates.

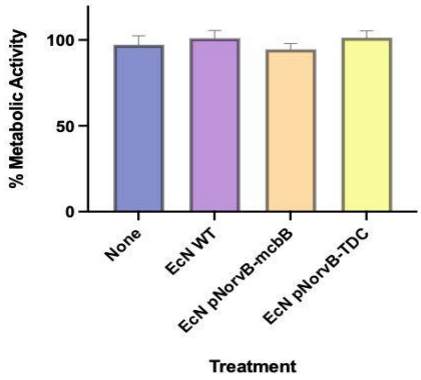

Figure 5.14. Cytotoxicity of engineered EcN cells on Caco-2 cells. % metabolic activity (normalized by the control with no treatment) after treatment with engineered EcN. Data are mean ± SD.; n=3 biological replicates.

fluorometric redox indicator resazurin (7-hydroxy-3H-phenoxazin-3-one 10-oxide), a blue non-fluorescent compound. Following intracellular uptake, resazurin undergoes reduction to the fluorescent resorufin (7-hydroxy-3H-phenoxazin-3-one) in the cytosol, driven by intracellular diaphorases and utilizing NADPH or NADH as a reductant. Resorufin emits a bright red fluorescence within the excitation range of 530–570 nm and an emission range of 580–610 nm, enabling quantification of fluorescence intensity as a measure of cell viability[149]. Results indicated that the engineered EcN exhibited negligible cytotoxic effects on Caco-2 cells, aligning with prior findings that emphasize the excellent safety profile associated with EcN (**Figure 5.14**).

The ability of NO-responsive EcN strains to prevent and treat inflammation was assessed using an *in vitro* murine macrophage model (LPS-challenged RAW264.7 cells). When exposed to LPS, inflammation is induced in RAW2 cells. Adequate quantities of the inflammatory biomarker NO are produced by these cells to activate the NO-responsive circuits employed in our strains and facilitate a straightforward readout through the Griess Assay[150]. The potential of inflammation-preventing NO-responsive EcN strains was assessed by treating RAW2 cells concurrently with 1 μg/ml LPS and relevant interventions. The potential of NO-responsive EcN strains to prevent or reduce inflammation was assessed by treating RAW2 cells concurrently with 1 μg/ml LPS and relevant interventions. For comparative purposes, RAW2 cells were also subjected to treatment with tryptamine and mesalazine (5-ASA), an FDA-approved small molecule drug commonly used as a first-line treatment for IBD[151]. The NO-responsive EcN demonstrated comparable performance to pure tryptamine in terms of inflammation prevention. All strains, along with

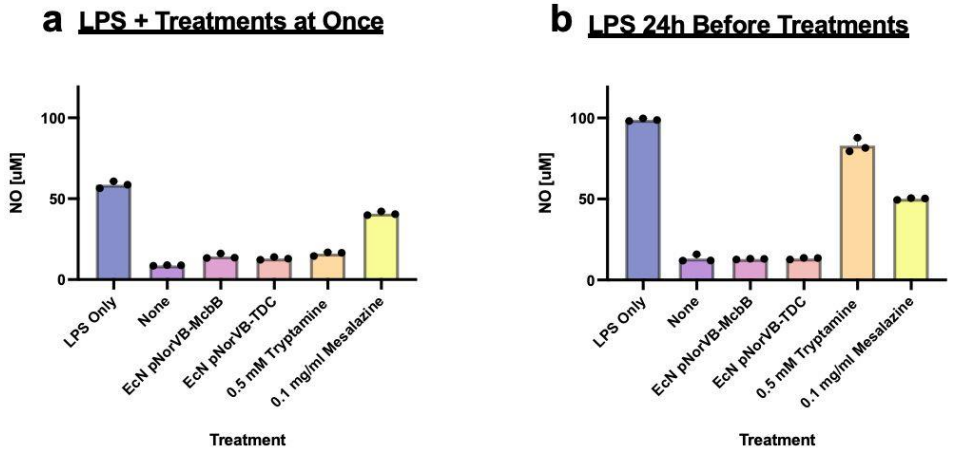

Figure 5.15. Engineered EcN exhibits anti-inflammatory effects in LPS-challenged murine macrophages. a) Evaluation of NO production by RAW264.7 cells 48 hours post various treatments, administered simultaneously with 1 μg/ml LPS challenge. b) Assessment of NO production by RAW264.7 cells 48 hours post various treatments, following a 1 μg/ml LPS challenge 24 hours prior to treatment. Data presented as mean ± SD; n=3 biological replicates.

tryptamine, exhibited superior efficacy in reducing NO production by RAW2 cells compared to mesalazine (**Figure 5.15 a**). To evaluate the therapeutic performance of NO-responsive EcN

strains in the case of active inflammation, first RAW2 cells were exposed to LPS for 24 hours prior to initiating treatments. In the context of active inflammation treatment, the engineered EcN reduced NO levels to that of the negative control, surpassing the efficacy of both tryptamine and mesalazine significantly (**Figure 5.15 b**). The resilience of NO-responsive EcN in addressing inflammation in macrophages under different levels of active inflammation, manipulated by the duration of LPS induction before treatments, underscores its potential for therapeutic use in both active and remission phases of IBD.

Anti-inflammation capacity of probiotic-ELMs had also been screened by monitoring the cytokine expression levels including IL-6 and IL-8 of Caco-2 cells with probiotic-ELM treatment. For this, CacoReady kits (ReadyCell), an *in vitro* cell-based model built on polarized human colorectal adenocarcinoma-derived cells (Caco-2) that resemble the intestinal epithelial barrier, were used. Cells differentiate for 21 days in 96 Transwell® inserts with semiporous (0.4 μm) polystyrene membrane, resulting in an apical compartment and a basal compartment that mimic the intestinal lumen and blood circulation, respectively (**Figure 5.16**).

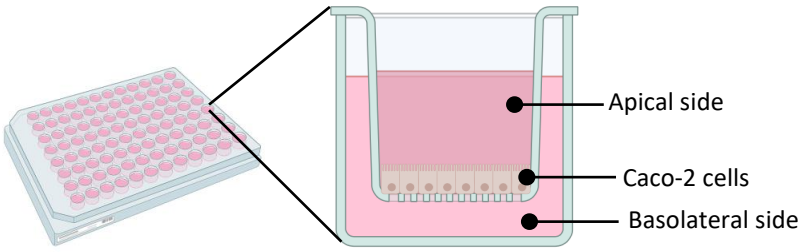

Figure 5.16. Graphical illustration of 96 well Caco-2 kit.

The ability of the strains to address inflammation in intestinal epithelial cells was assessed. Given that Caco-2 cells do not naturally generate sufficient NO within the medically relevant range for IBD, EcN or EcN-laden ELMs were pre-cultivated in colonic fluid from a fed or fasted state, with or without the presence of NO, for 24 hours before introduction to Caco-2 cells. Supernatants,

derived from these cultures, were applied to the apical compartment of a 96-transwell plate containing Caco-2 cells before inducing inflammation on the apical side with 0.1 µg/ml LPS and on the basolateral side with a pro-inflammatory cocktail (0.025 µg/ml IL1β, 0.05 µg/ml TNFα, and 0.05 µg/ml IFNγ).

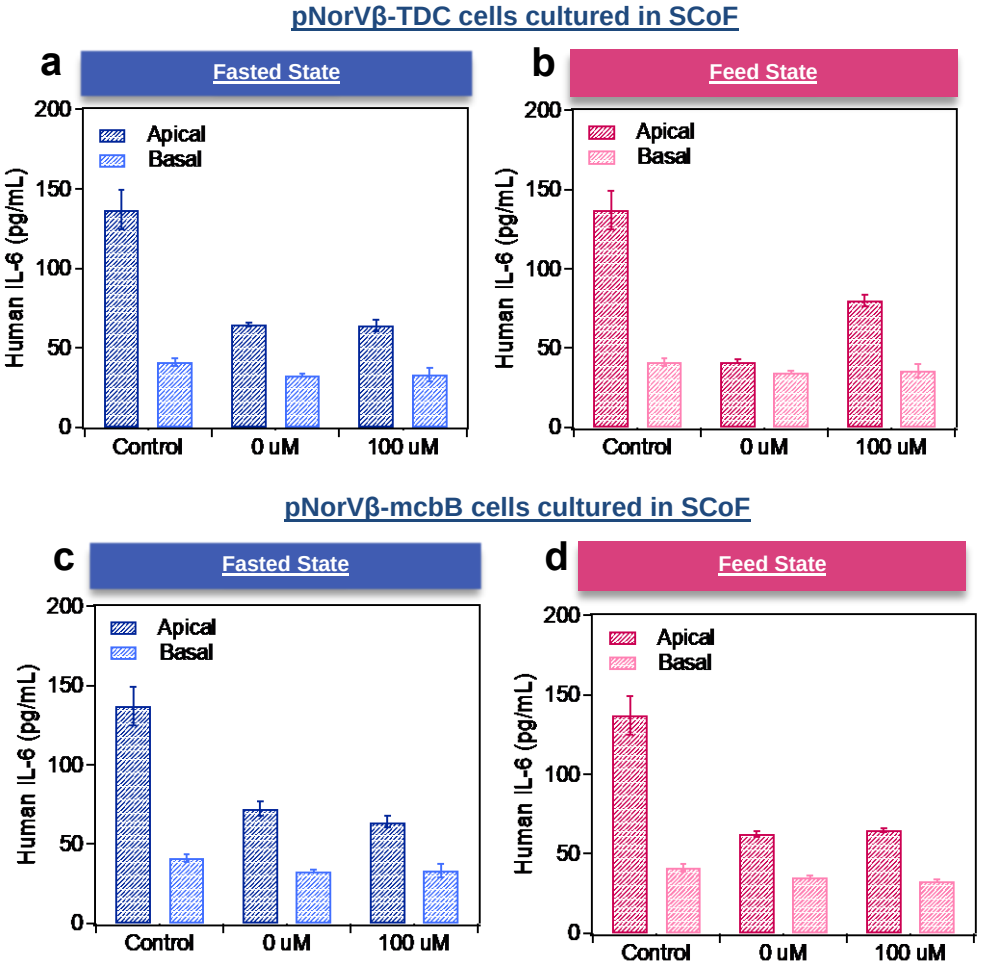

Figure 5.17. Reduction in secretion of pro-inflammatory cytokine, IL6, by Caco-2 cells upon inflammation challenge with NO-responsive EcN. a-b): IL-6 production by Caco-2 cells post inflammation induction, treated with nothing (control) or EcN pNorVβ-TDC pre-induced with 0 or 100 µM NO and pre-cultured in FaSSCoF and FeSSCoF, respectively. c-d) IL-6 production by Caco-2 cells post inflammation induction, treated with nothing (control) or EcN pNorVβ-mcbB pre-induced with 0 or 100 µM NO and pre-cultured in FaSSCoF and FeSSCoF, respectively. Data presented as mean ± SD; n=3 biological replicates.

After 24h incubation, samples were collected from both apical and basolateral sides and IL8 and IL6 levels were measured via ELISA assays. Compared to the control group (no treatment), there was a significant reduction in IL6 levels after treatment with therapeutics produced from either free EcN strains or probiotic-ELMs in feed and fasted state colonic fluids

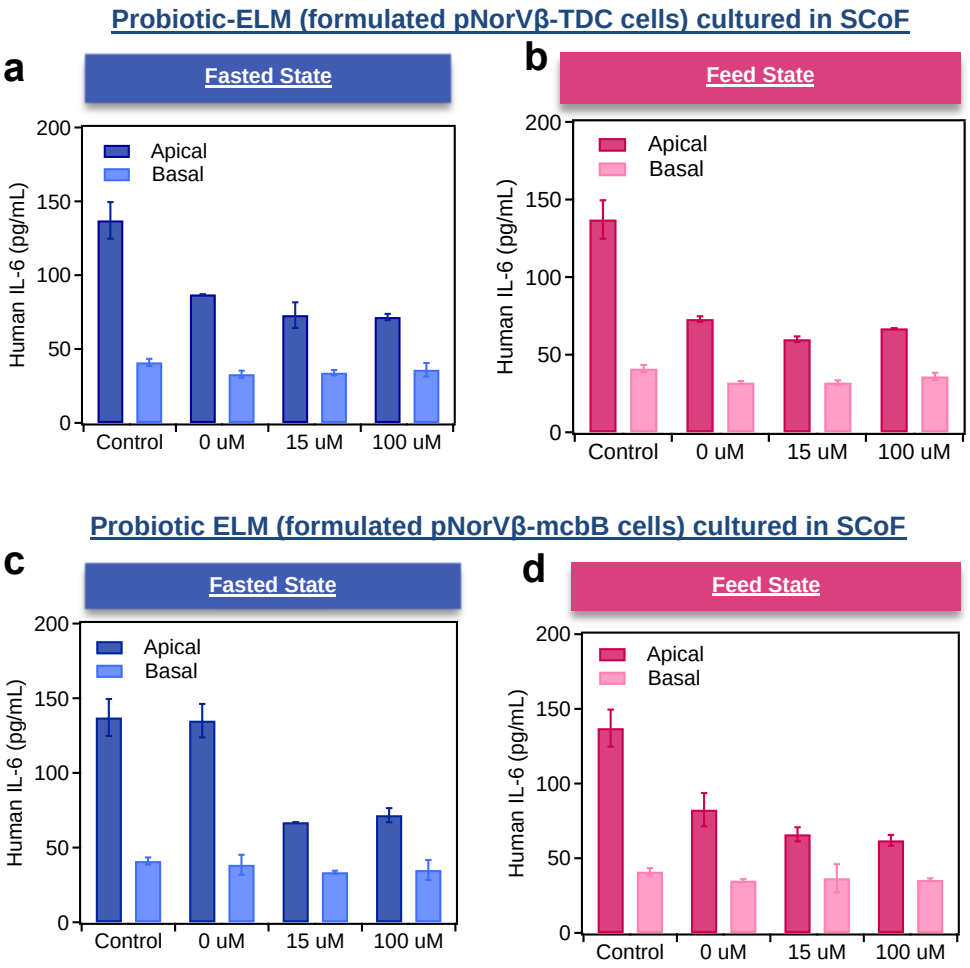

Figure 5.18. Reduction in secretion of pro-inflammatory cytokine, IL6, by Caco-2 cells upon inflammation challenge with NO-responsive probiotic-ELM constructs. a-b): IL-6 production by Caco-2 cells post inflammation induction, treated with nothing (control) or EcN pNorVβ-TDC pre-induced with 0 or 100 µM NO and pre-cultured in FaSSCoF and FeSSCoF, respectively. c-d) IL-6 production by Caco-2 cells post inflammation induction, treated with nothing (control) or EcN pNorVβ-mcbB pre-induced with 0 or 100 µM NO and pre-cultured in FaSSCoF and FeSSCoF, respectively. Data presented as mean ± SD; n=3 biological replicates.

(**Figures 5.17-5.18**). On the other hand, no linear correlation was observed fo IL6 reduction level with the amount of produced therapeutic either tryptamine (**Figures 5.13 e** and **5.13 g**, free EcN

pNorVβ-TDC and probiotic-ELM formulated with EcN pNorVB-TDC, respectively) or β-carboline (**Figures 5.13 f** and **5.13 h**, free EcN pNorVβ-mcbB and probiotic-ELM formulated with EcN pNorVB-mcbB, respectively).

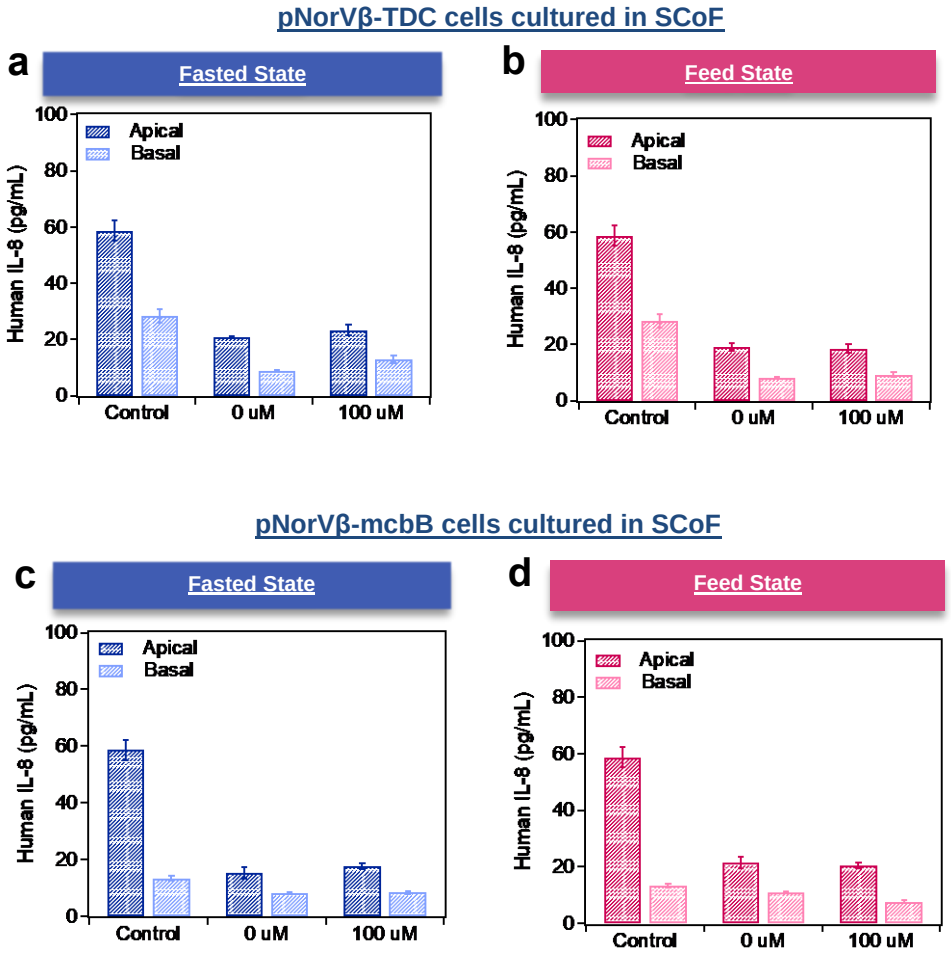

Figure 5.19. Reduction in secretion of pro-inflammatory cytokine, IL8, by Caco-2 cells upon inflammation challenge with NO-responsive EcN. a-b): IL-6 production by Caco-2 cells post inflammation induction, treated with nothing (control) or EcN pNorVβ-TDC pre-induced with 0 or 100 µM NO and pre-cultured in FaSSCoF and FeSSCoF, respectively. c-d) IL-6 production by Caco-2 cells post inflammation induction, treated with nothing (control) or EcN pNorVB-mcbβ pre-induced with 0 or 100 µM NO and pre-cultured in FaSSCoF and FeSSCoF, respectively. Data presented as mean ± SD; n=3 biological replicates.

It is important to highlight that both EcN pNorVB-TDC and EcN pNorVβ-mcbB cells demonstrated the ability to produce tryptamine and β-carboline, respectively, even in the absence of NO (**Figure 5.13 e-h**). While these production levels were lower than those observed in the presence of NO, these quantities might still be adequate to reduce IL6 levels in Caco-2 cells. A

similar trend was observed in IL8 levels of Caco-2 cells which were treated with the therapeutics produced by free EcN strains, EcN pNorVβ-TDC (tyriptamine) (**Figure 5.19 a, b**) and EcN pNorVβ-mcbB (β-carboline) (**Figure 5.19 c, d**) in feed and fasted state colonic fluids. On the other hand, in samples treated with therapeutics derived from probiotic-ELMs, IL-8 production exhibited a NO concentration-dependent decrease for both ELM constructs formulated with EcN

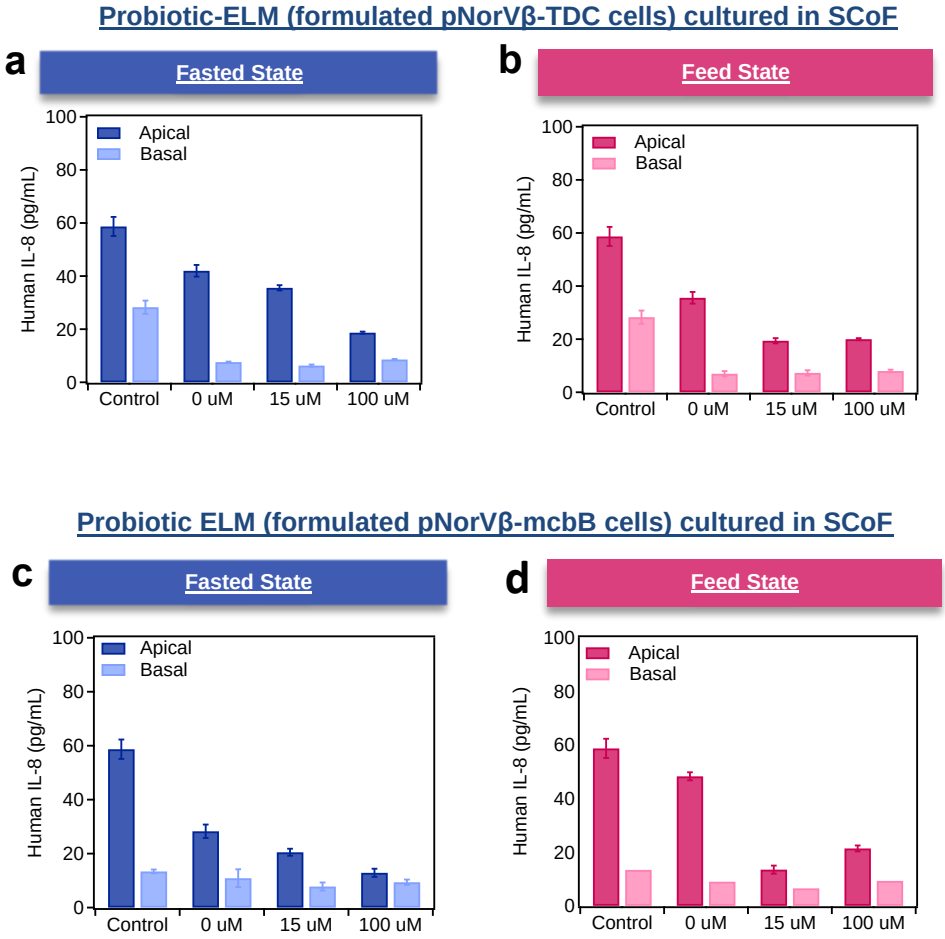

Figure 5.20. Reduction in secretion of pro-inflammatory cytokine, IL8, by Caco-2 cells upon inflammation challenge with NO-responsive probiotic-ELM constructs. a-b): IL-6 production by Caco-2 cells post inflammation induction, treated with nothing (control) or EcN pNorVβ-TDC pre-induced with 0 or 100 µM NO and pre-cultured in FaSSCoF and FeSSCoF, respectively. c-d) IL-6 production by Caco-2 cells post inflammation induction, treated with nothing (control) or EcN pNorVB-mcbβ pre-induced with 0 or 100 µM NO and pre-cultured in FaSSCoF and FeSSCoF, respectively. Data presented as mean ± SD; n=3 biological replicates.

pNorVβ-TDC and EcN pNorVβ-McbB (**Figure 5.20**). A 3-fold decrease in IL-8 (on the apical

side for 100 uM vs 0 uM NO) was observed when cultured with supernatant from EcN pNorVβ-TDC ELMs, was 3 for both fasted and fed states, respectively (**Figure 5.20 a, b**). The supernatant from EcN pNorVβ-McbB ELMs afforded a 5-fold and 3-fold the fold decrease in IL-8 (on the apical side for 100 uM vs 0 uM NO) for the fasted and fed states, respectively (**Figure 5.20 c, d**). Therefore, results showed that using the probiotic-ELMs in inflammation treatment in the gut, enhances the precision of controlling the anti-inflammatory efficacy of the treatment, aligning with the trend of inflammation biomarkers in the solution. Although the mechanism behind this phenomenon is not entirely clear, it underscores the potential for ELMs to serve as a prolonged inflammation treatment. This is particularly valuable during periods of IBD remission when lower levels of anti-inflammatory activity are preferable due to reduced biomarker levels. Notably, this dose-dependent response was exclusively observed in the apical compartment, representing the intestinal lumen. This observation suggests that a minimal secretion of the targeted anti-inflammatory compounds might be adequate for a substantial decrease in inflammation on the basolateral side, facing the underlying tissue.

The Caco-2 permeability assay utilizes a well-established method to measure the rate of flux of a compound across polarized Caco-2 cell monolayers. The data generated through this assay can be employed to predict the in vivo absorption of drugs[147,152]. The permeability of both tryptamine and β-carboline which were produced from free EcN cells (pNorVβ-TDC and pNorVβ-McbB, respectively) and probiotic-ELMs formulated with these strains were also evaluated by using Caco-2 cell lines. First, these therapeutics were produced in feed and fasted state colonic

fluids with the presence of 100 μM, then they were applied to Caco-2 cells' either apical or basolateral sides (**Figure 5.21 a-b**).

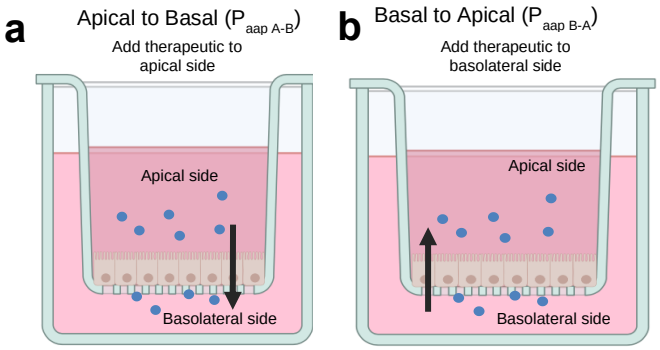

Figure 4.21. Caco-2 permeability assay. a) Apical-to-basal studies, test therapeutics are administered to the apical side of the cell monolayer (upper compartment of the insert), and the evaluation of apical-to-basal (A-B) transport through the cell barrier is conducted by recovering samples and detecting the test therapeutics in the basal (lower) compartment over a specified incubation period. The A-B permeability of test compounds is quantified as the coefficient of apparent permeability ($P_{app\ A-B}$) in cm/s. b) Basal-to-apical studies, test therapeutics are administered to the basal side of the cell monolayer (lower compartment of the insert), and the evaluation of basal-to-apical (B-A) transport through the cell barrier is conducted by recovering samples and detecting the test therapeutics in the apical (upper) compartment over a specified incubation period. The B-A permeability of test compounds is quantified as the coefficient of apparent permeability ($P_{app\ B-A}$) in cm/s.

The transport efficiency of tested samples was evaluated in each sample through apparent permeability coefficient (P_{app}) calculation, as following equitation (5.1):

$$Apparent\ permeability\ coeeficient = \frac{dQ}{dt} x \frac{1}{AxCo} \qquad (5.1)$$

dQ/dt: proportion of test compound that crosses the barrier at each time point (nmol/s)
A: the product of the crossed area (cm^2)
C_o: initial concentration of test compound. (nmol/ml)

Table 5.1 shows the P_{app} values of tryptamine and β-carboline which were produced from free EcN cells (pNorVβ-TDC and pNorVβ-McbB, respectively) and probiotic-ELMs formulated with these strains, in fasted and feed state colonic fluids with the presence of 100 μM NO.

Table 5.1. Permeability of tryptamine and β-Carboline produced in feed and fasted state colonic fluids by free EcN cells and probiotic-ELMs.

Tyriptamine			**β-Carboline**		
Probiotic-ELM contains pNorVβ-TDC cells			**Probiotic-ELM contains pNorVβ-McbB Cells**		
	FaSSCoF	FeSSCoF		FaSSCoF	FeSSCoF
$P_{app\ A-B}$	$2x10^{-5}$ cm/s	$6x10^{-5}$ cm/s	$P_{app\ A-B}$	$3x10^{-4}$ cm/s	$5x10^{-4}$ cm/s
$P_{app\ B-A}$	$1.6x10^{-5}$ cm/s	$3x10^{-5}$ cm/s	$P_{app\ B-A}$	$3x10^{-4}$ cm/s	$6x10^{-4}$ cm/s
Free EcN pNorVβ-TDC cells			**Free pNorVβ-McbB Cells**		
	FaSSCoF	FeSSCoF		FaSSCoF	FeSSCoF
$P_{app\ A-B}$	$2.6x10^{-5}$ cm/s	$6x10^{-5}$ cm/s	$P_{app\ A-B}$	$4x10^{-4}$ cm/s	$6.5x10^{-5}$ cm/s
$P_{app\ B-A}$	$2.3x10^{-5}$ cm/s	$5.8x10^{-5}$ cm/s	$P_{app\ B-A}$	$4x10^{-4}$ cm/s	$1.5x10^{-4}$ cm/s

Permeability studies revealed that both tryptamine and β-carboline, whether secreted from free cells or probiotic-ELMs, exhibited high permeability ($P_{app} > 10x10^{-6}$ cm/s), suggesting a potential for *in vivo* absorption[153]. Efflux ratio (ER) is another key factor that provide information about in vivo absorption of drug candidates. The Caco-2 cell line is a good model to test intestinal efflux transporters which play a crucial role in drug absorption by identifying, binding, and expelling specific drugs into the intestinal lumen. A high drug efflux (>2) indicates poor absorption for tested compounds[153,154].

The efflux ratio serves as a general measure of active processes influencing compound permeability which calculate by dividing the tested compound's P_{app} in the B-A direction by the P_{app} in the A-B direction, as given in the Equation 5.2:

$$ER = \frac{Apparent\ permeability\ coeeficient,B-A}{Apparent\ permeability\ coeeficient,A-B} \qquad (5.2)$$

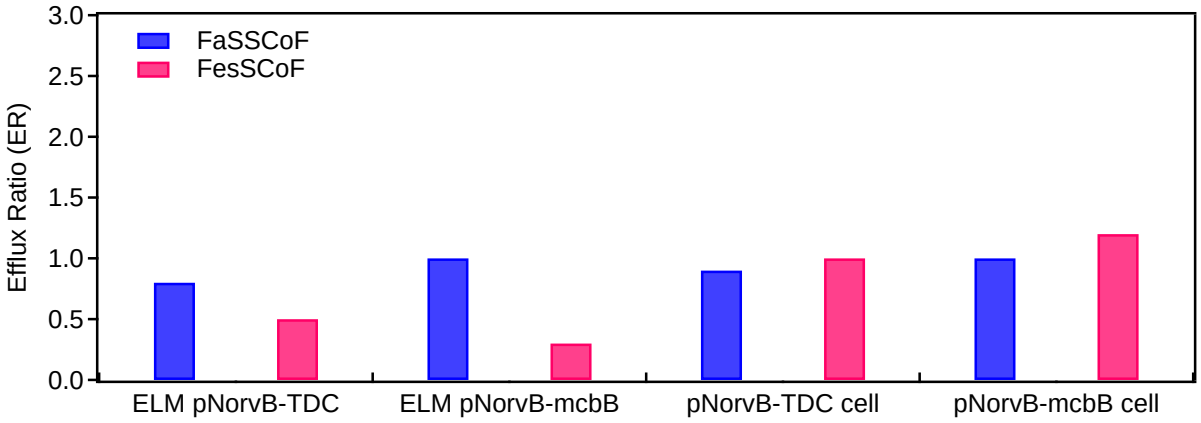

Figure 5.22. Efflux ratio of tryptamine produced from probiotic ELM (ELM pNorvB-TDC), β-carboline produced from probiotic ELM (ELM pNorvB-mcbB), tryptamine produced from free EcN pNorvB-TDC cells, β-carboline produced from free EcN pNorvB-mcbB cells.

Figure 5.22 shows the ER of tryptamine and β-carboline which were produced from free EcN cells (pNorVβ-TDC and pNorVβ-McbB, respectively) and probiotic-ELMs formulated with these strains, in fasted and feed state colonic fluids with the presence of 100 μM NO. ER of each sample was calculated lower than 2 which shows a potential of good absorption *in vivo.*

5.4 CONCLUSION

Developing long-term treatment approaches for IBD that localize treatment to the inflammation site and conditionally act during active inflammation holds promise to enhance efficacy while reducing safety risks and side effects. Engineered probiotics designed to release therapeutic compounds in response to inflammatory biomarkers demonstrate significant potential

for achieving conditional therapeutic outcomes. Creating probiotic-ELM structures with these engineered probiotics offers them spaces where they can persist in the gut for long periods of time and produce targeted therapeutic compounds without competing with native microbiome populations for colonization. The results represented in this Chapter, shows that probiotic-ELM constructs can created to detect and respond to inflammatory biomarkers by secreting anti-inflammatory molecules. These probiotic-ELMs robustly produce anti-inflammatory compounds namely tryptamine and β-carboline in simulated intestinal and colonic environments, with production levels adjusted by medically relevant concentrations of NO for active vs. inactive IBD. Demonstrating safety and efficacy in treating inflammation, probiotic-ELMs exhibit promising results in in vitro models of macrophages and intestinal epithelial cells.

5.5 EXPERIMENTAL SECTION

5.5.1 *Culture Media and Conditions for Bacterial Cells*

Bacterial cells were routinely cultured in Lysogeny broth (LB) medium containing yeast extract (5 g/L), tryptone (10 g/L), and NaCl (10 g/L) for preparation of inoculants and cell propagation with supplementation of appropriate antibiotics as needed (50 μg/ml Kanamycin and/or 30 μg/ml Chloramphenicol and/or 100 μg/ml Ampicillin). For Nitric Oxide sensor experiments, a defined M9G+CAA media was made according to the following formula: 1X M9 salts, 1 g/L casamino acids, 5 g/L glucose, 20 mM $MgSO_4$, and 0.1 mM $CaCl_2$ with supplementation of appropriate antibiotics were added as needed.

5.5.2 *SLA 3D printing of probiotic-ELM constructs*

To prepare the for vat photopolymerization resin 40 wt% PEGDA and 5 wt% glycerol were dissolved in appropriate cell culture media, then 1 mL of cell suspension containing $1x10^9$

cells/mL was introduced to 20 grams of a resin formulation. 1 wt% of lithium phenyl-2,4,6-trimethylbenzoylphosphinate was used as photo initiator. The constructs were 3D printed in the Open Mode using a Formlabs Form 2 printer with a layer height of 100 µm. CAD models were designed in Autodesk Fusion or downloaded from Thingiverse.

5.5.3 *Simulated Intestine and Colon Fluids*

Biorelevant feed and fasted state simulated intestine and colon kits were used to prepare intestinal and colonic fluids, according to the procedure provided from manufacturer. Simulated intestinal media and simulated colonic media was prepared fresh for each experiment and used within 48h. 3D-pinted probiotic-ELMs placed in culture media supplements simulated fluids (1:1) and their bioproduction performance was evaluated. Simulated fluids were refreshed every day during 7 d of culturing. For testing of baseline anti-inflammatory production, engineered EcN were grown in culture tubes for oscillatory condition testing, fed and fasted variations of SSIF or SSCoF were oscillated on a daily basis. Supernatant samples were taken daily for analysis of metabolites via LCMS.

5.5.4 *Quantification of Anti-Inflammatory Metabolites*

Metabolite quantification from supernatant samples was performed using Bruker Esquire LC-Ion Trap Mass Spectrometer with Agilent HPLC. In each day samples were collected from cultured media, centrifuged at 4400 rpm for 10 min, filtered with 0.2-µm nylon syringe filters (Wheaton Science) and mixed with EtOH 1:1 v/v ratio, then analyzed. Mass spectrometer was operated in positive mode, scan range was between 50.00 m/z to 1100.00 m/z, skim1 was 15.0 volt and capillary exit was 55.0 volt. In HPLC analysis Zorbax Eclipse Plus C18 column (3.0 × 150 mm, 3.5 µm; Agilent) was used. The mobile phase consisted of 1% (v/v) acetic acid in water

or acetonitrile. Analyte detection was performed at a wavelength of 280 nm using a flow rate of 0.2 mL min^{-1} with a column temperature of 25°C.

5.5.5 *Live and dead cell analysis*

Live and dead cells were imaged under fluorescence microscopy (EVOS Fluorescent Imaging Microscopy) after staining with Biotium Live/Dead Yeast staining kit according to the procedure provided by the manufacturer.

5.5.6 *Confocal imaging*

Nikon A1R HD25 laser scanning confocal microscope was performed to take cell images. 400 μL of probiotic-ELM resin was placed in silicon mold with 3 mm depth, and cured under 405 nm for 5 min. Then it placed in 6 well plate and cultured in FeSSIF which supplemented with LB media 1:1 ratio for 2 d. Before confocal imaging, culture media removed form photocured samples and samples washed with PBS at 3 times.

5.5.7 *Cell Lines and Culture Conditions*

Human colon epithelial cells (Caco-2, ATCC HTB-37) were cultured in Dulbecco's modified Eagle medium (DMEM, Gibco, ThermoFisher) supplemented with 10% fetal bovine serum (FBS, Biowest, France) and 1% penicillin/streptomycin (Sigma-Aldrich). Murine macrophage cells (RAW264.7, ATCC TIB-71) were cultured in DMEM 10% fetal bovine serum (FBS, Biowest, France) and 1% penicillin/streptomycin (Sigma-Aldrich). For viability studies, Caco-2 cells were seeded in a 96 well microplate at a density of $3x10^4$ cells per well and grown for 24h at 37°C. The media was replaced and Caco-2 cells were cultured with or without engineered EcN at a concentration of $1x10^8$ cells/ml for 24h. For anti-inflammatory assays, RAW264.7 cells were seeded in a 96 well microplate at a density of $3x10^4$ cells per well and grown

for 24h at 37°C. Media was replaced with 140ul DMEM which lacked phenol red (to avoid interference with the colorimetric Griess Assay). For the case of simultaneous inflammation induction and treatment, the 140 µl of media with 1 µg/ml LPS (Sigma Chemical Co., St. Louis, MO, U.S.A) and the presence or absence of $1x10^6$ cells/ml engineered EcN or other treatments (mesalazine, tryptamine). Cells were cultured 48h at 37°C before performing the Griess Assay. For the case of inflammation induction prior to treatments, cells were cultured with 1 µg/ml LPS for 24 h, followed by addition of treatments ($1x10^6$ cells/ml engineered EcN, mesalazine, or tryptamine). Cells were cultured 48h at 37°C before performing the Griess Assay.

5.5.8 *Cell Viability Studies*

Viability of Caco-2 cells was assessed by measuring metabolic activity of Caco-2 using an alamar blue assay (Thermofisher Scientific). Caco-2 cells were seeded in a 96 well microplate at a density of $3x10^4$ cells per well and grown for 24 h at 37°C. The media was replaced, and Caco-2 cells were cultured with or without engineered EcN at a concentration of $1x10^8$ cells/ml for 24 h. To carry out metabolic studies, the Caco-2 cells were rinsed with PBS and incubated at 37°C for 3 h with 10 µl alamar blue reagent dissolved in 80 µL PBS. After incubation, 75 µl per well were analyzed on a plate reader (Tecan Infinite 200 Pro) by reading the absorbance at 570nm. % Metabolic Activity was calculated by dividing absorbance values of each experimental condition by the control.

5.5.9 *Anti-inflammatory in vitro Assays*

5.5.9.1 *In vitro* murine macrophage model

Nitric oxide production by RAW264.7 cells was quantified using the Griess Assay to assess inflammation following LPS-induced inflammation. Briefly, 50 µl of supernatant was mixed with

50 µl Griess Reagent (Millipore Sigma G4410) and allowed to react for 15 min. Absorbance was read at 550nm in a microplate reader (Tecan Infinite 200 Pro), with nitrite concentration calculated using a standard curve of sodium nitrite over the working range of the assay (1-100 µM).

5.5.9.2 *In vitro* Caco-2 cell model

Polarized Caco-2 cells placed in 96 well plate was purchased from Ready cells. After eceiveing the cell, shipment medium was replaced with Dulbecco's Modified Eagle's Medium - low glucose (1 g/L) (Sigma) supplemented with (final concentrations): 0 % v/v Fetal Bovine Serum (Biowest), 2 mM L-glutamine (Lonza) and 100 µ/mL; 0.1 mg/mL Penicillin-Streptomycin. After 3 days culturing, TEER values were measured prior to inflammation and permeability assays (TEER > 500 Ω x cm^2). Anti-inflammatory cytokine production, including IL-6 and IL-8, by Caco-2 cells was quantified by ELISA kits (Sigma).

BIBLIOGRAPHY

[1] Sugianto, W., Altin-Yavuzarslan, G., Tickman, B.I., Kiattisewee, C., Yuan, S.-F., Brooks, S.M., Wong, J., Alper, H.S., Nelson, A., and Carothers, J.M. Gene expression dynamics in input-responsive engineered living materials programmed for bioproduction. *Mater. Today Bio,* **20,** 10067 (2023).

[2] Yuan, S. F., Brooks, S. M., Nguyen, A. W., Lin, W. L., Johnston, T. G., Maynard, J. A., Nelson, A. & Alper, H. S., Bioproduced Proteins On Demand (Bio-POD) in hydrogels using Pichia pastoris. *Bioactiv. Mater.* **6,** 2390–2399 (2021).

[3] Brooks, S. M., Marsan, C., Reed, K. B., Yuan, S. F., Nguyen, D. D., Trivedi, A., Altin-Yavuzarslan, G., Ballinger, N., Nelson, A & Alper, H. S. tripartite microbial co-culture system for de novo biosynthesis of diverse plant phenylpropanoids. *Nat. Commun.* **14,** 4448 (2023).

[4] Gao, L. *et al.* Engineered living hydrogels for robust biocatalysis in pure organic solvents. *Cell Rep. Phys. Sci.* **3,** 101054 (2022).

[5] Altin-Yavuzarslan, G.; Brooks, S. M.; Yuan, S.-F.; Park, J. O.; Alper, H. S.; Nelson, A. Additive Manufacturing of Engineered Living Materials with Bio-Augmented Mechanical Properties and Resistance to Degradation. *Adv. Funct. Mater.* **33,** 2300332 (2023).

[6] Johnston,T. G., Yuan, S. F. Wagner, J. M., Yi, X. Saha A., Smith, P., Nelson, A., Alper H. S. Compartmentalized microbes and co-cultures in hydrogels for on-demand bioproduction and preservation. *Nat. Commun.* 11, 1–11 (2020).

[7] Gantenbein, S., Colucci, E., Käch, J., Trachsel, E., Coulter, F. B., Rühs, P. A., Masania, K. & Studart, A. R. Three-dimensional printing of mycelium hydrogels into living complex materials. *Nat. Mater.* **22,** 128-13, (2023).

[8] Rivera-Tarazona, L. K., Shukla, T., Singh, K. A., Gaharwar, A. K., Campbell, Z. T., & Ware, T. H. 4D printing of engineered living materials. *Adv. Funct. Mater.* **32,** 2106843, (2022).

[9] Zhu, Y., Wang, Q., Chen, Y., Xie, Y., Han, G., Liu, S., & Guo, Y.Living Probiotics-Loaded Hydrogel Microspheres with Gastric Acid Resistance and ROS Triggered Release for Potential Therapy of Inflammatory Bowel Disease. *ACS Appl. Polym Mater* **5**, 957–967 (2023).

[10] Wang, R., Guo, K., Zhang, W., He, Y., Yang, K., Chen, Q., & Xu, H. Poly-γ-glutamic acid microgel-encapsulated probiotics with gastric acid resistance and smart inflammatory factor targeted delivery performance to ameliorate colitis. *Adv Funct Mater* **32,** 2113034 (2022).

[11] Freyman, M.C., Kou, T., Wang, S., and Li, Y. 3D printing of living bacteria electrode. Nano Res. **13,** 1318–1323 (2020).

[12] Su, Y., McCuskey, S.R., Leifert, D., Moreland, A.S., Zhou, L., Llanes, L.C., Vazquez, R.J., Sepunaru, L., and Bazan, G.C. (2021). A Living Biotic–Abiotic Composite that can Switch Function Between Current Generation and Electrochemical Energy Storage. *Adv. Funct. Mater.* **31,** 2007351 (2021).

[13] Choi, J., Min, J., Kim, D., Kim, J., Kim, J., Yoon, H., & Ko, S. H. Hierarchical 3D Percolation Network of Ag–Au Core–Shell Nanowire-Hydrogel Composite for Efficient Biohybride Electrodes. *ACS Nano* **17,** 17966–17978 (2023).

[14] Zhao, C., Chen, H., Song, Y., Zhu, L., Ai, T., Wang, X., Wei, X.Electricity production performance enhancement of microbial fuel cells with double-layer sodium alginate hydrogel bioanodes driven by high-salinity waste leachate. *Water Res.* **242,** 120281 (2023).

[15] Kirubaharan, C. J., Wang, J. W., Abbas, S. Z., Shah, S. B., Zhang, Y., Wang, J. X., & Yong, Y. C, Self-assembly of cell-embedding reduced graphene oxide/ polypyrrole hydrogel as efficient anode for high-performance microbial fuel cell. *Chemosphere* **326,** 138413 (2023).

[16] Wang, Y., Yang, H., Wang, J., Dong, J. & Duan, Y. Self-Supporting Conductive Polyaniline–Sodium Alginate–Graphene Oxide/Carbon Brush Hydrogel as Anode Material for Enhanced Energy in Microbial Fuel Cells. *Coatings* **13,** 790 (2023).

[17] McBee, R. M., Lucht, M., Mukhitov, N., Richardson, M., Srinivasan, T., Meng, D., Chen, H., Kaufman, A., Reitman, M., Muck, C., Schaak, D., Voigt, C & Wang, H. H. Engineering living and regenerative fungal–bacterial biocomposite structures. *Nat. Material.*, **21,** 471-478, (2022).

[18] Zhu, T.; Dittrich, M. Carbonate Precipitation through Microbial Activities in Natural Environment, and Their Potential in Biotechnology: A Review. *Front. Bioeng. Biotechnol.* 4 (2016).

[19] Jonkers, H. M.; Thijssen, A.; Muyzer, G.; Copuroglu, O.; Schlangen, E. Application of Bacteria as Self-Healing Agent for the Development of Sustainable Concrete. *Ecol. Eng*. **36,** 230–235 (2010).

[20] Oh, Jeong-Joo, Satya Ammu, Vivian Dorine Vriend, Roland Kieffer, Friedrich Hans Kleiner, Srikkanth Balasubramanian, Elvin Karana, Kunal Masania, and Marie-Eve Aubin-Tam. Growth, Distribution, and Photosynthesis of Chlamydomonas Reinhardtii in 3D Hydrogels. *Adv. Mater*. 2305505 (2023).

[21] Chipara, Mircea. "Space Materials: The Final Frontier." *Material. Today* **8,** 72 (2005)

[22] Koehle, A. P., Brumwell, S. L., Seto, E. P., Lynch, A. M., & Urbaniak, C., Microbial applications for sustainable space exploration beyond low Earth orbit. *npj Microgravity* **9**, 47 (2023).

[23] Santomartino, R., Averesch, N. J., Bhuiyan, M., Cockell, C. S., Colangelo, J., Gumulya, Y., & Zea, L., Toward sustainable space exploration: a roadmap for harnessing the power of microorganisms. *Nat. Commun.* **14**, 1391 (2023).

[24] DallBauman, L. A., and J. E. Finn. "Adsorption Processes in Spacecraft Environmental Control and Life Support Systems." In *Adsorption and Its Applications in Industry and Environmental Protection*, edited by A. Dąbrowski, 120:455–71. Studies in Surface Science and Catalysis. Elsevier, 1999.

[25] González, L. M., Mukhitov, N. & Voigt, C. A. Resilient living materials built by printing bacterial spores. *Nature Chem. Biol.* **16,** 126–133 (2020).

[26] Brooks, S. M., Reed, K. B., Yuan, S. F., Altin-Yavuzarslan, G., Shafranek, R., Nelson, A., & Alper, H. S., Enhancing long-term storage and stability of engineered living materials through desiccant storage and trehalose treatment. *Biotechnol. Bioeng.* **120,** 572–582 (2023).

[27] Daly, A. C., Riley, L., Segura, T. & Burdick, J. A. Hydrogel microparticles for biomedical applications. *Nat Rev Mater 5,* 20–43 (2020).

[28] Li, Y., Di, Z., Yan, X., Wen, H., Cheng, W., Zhang, J., & Yu, Z., Biocatalytic living materials built by compartmentalized microorganisms in annealable granular hydrogels. *Chem. Eng. J.* **445,** 136822 (2022).

[29] Qian, F., Zhu, C., Knipe, J. M., Ruelas, S., Stolaroff, J. K., DeOtte, J. R. & Baker, S. E.Direct Writing of Tunable Living Inks for Bioprocess Intensification. *Nano letters* 19, 5829–5835 (2019).

[30] Li, L., Zhang, R., Chen, L., Tian, X., Li, T., Pu, B.,& Liu, Y. Permeability-Engineered Compartmentalization Enables In Vitro Reconstitution of Sustained Synthetic Biology Systems. *Adv. Sci.* **9,** 2203652 (2022).

[31] Li, J., Dong, Y., Hu, L., Zhang, Y., Fu, Q., Zhang, L.,& Liao, Q. Microalgae hydrogel-derived monolithicfree-standing air cathode for microbial fuel cells: Tailoring the macroporous structure for enhanced bioelectricity generation. *Renew. Sust. Energy Review.* **153,** 111773 (2022).

[32] Carvalho, R. N., Monteiro, L. L., Sousa, S. A., Ramanaiah, S. V., Leitão, J. H., Cordas, C. M., & Fonseca, L. P., Design and Optimization of Microbial Fuel Cells and Evaluation of a New Air-Breathing Cathode Based on Carbon Felt Modified with a Hydrogel—Ion Jelly®. *Energies* **16,** 4238 (2023).

[33] Moradian, J. M., Mi, J. L., Dai, X., Sun, G. F., Du, J., Ye, X. M., & Yong, Y. C. Yeast-induced formation of graphene hydrogels anode for efficient xylose-fueled microbial fuel cells. *Chemosphere*, **291,** 132963 (2022).

[34] Elsacker, E., Zhang, M., & Dade-Robertson, M. Fungal Engineered Living Materials: The Viability of Pure Mycelium Materials with Self-Healing Functionalities. *Adv. Funct. Mater.*2301875, (2023).

[35] Chen, B., Kang, W., Sun, J., Zhu, R., Yu, Y., Xia, A., Yu, M., Wang, M., Han, J., Chen, Y., Teng, L., Tian, Q., Yu, Y., Li, G., You, L., Liu, Z. & Dai, Z. Programmable living assembly of materials by bacterial adhesion. *Nat. Chem. Biol.* **18,** 289-294, (2022).

[36] Caro-Astorga, J., Walker, K. T., Herrera, N., Lee, K. Y., & Ellis, T. Bacterial cellulose spheroids as building blocks for 3D and patterned living materials and for regeneration. *Nat. Commun.* **12**, 5027, (2021).

[37] Duraj-Thatte, A. M., Courchesne, N. M. D., Praveschotinunt, P., Rutledge, J., Lee, Y., Karp, J. M., & Joshi, N. S. (2019). Genetically programmable self-regenerating bacterial hydrogels. *Adv. Mater.*,**31,** 1901826, (2019).

[38] Rivera-Tarazona, L. K., Bhat, V. D., Kim, H., Campbell, Z. T., & Ware, T. H. Shape-morphing living composites. *Sci. Adv.* **6,** eaax8582, (2020).

[39] Rivera-Tarazona, L. K., Kalairaj, M. S., Corazao, T., Javed, M., Zimmern, P. E., Subashchandrabose, S., & Ware, T. H. Controlling shape morphing and cell release in engineered living materials. *Biomater. Adv.* **143,** 213182, (2022).

[40] Wang, N., Nan F. & Xiao D. C. The extent and mechanism of the effect of protectant material in the production of active lactic acid bacteria powder using spray drying: A review. *Curr Opin Food Sci* **44**, 100807 (2022).

[41] Kanimozhi, N. V., & M. Sukumar. Effect of different cryoprotectants on the stability and survivability of freeze dried probiotics. *Food Chem Adv* **3,** 100428 (2023).

[42] Feng, K., Huangfu, L., Liu, C., Bonfili, L., Xiang, Q., Wu, H., & Bai, Y. Electrospinning and Electrospraying: Emerging Techniques for Probiotic Stabilization and Application. *Polymers* **15**, 2402 (2023).

[43] Aghlara-Fotovat, S., Musteata, E., Doerfert, M. D., Baruch, M., Levitan, M., Tabor, J. J., & Veiseh, Hydrogel-encapsulation to enhance bacterial diagnosis of colon inflammation. *Biomaterials* **301**, 122246–122246 (2023).

[44] Mimee, M., Nadeau, P., Hayward, A., Carim, S., Flanagan, S., Jerger, L.,& Lu, T. K. An ingestible bacterial-electronic system to monitor gastrointestinal health. *Science* **360**, 915–918 (2018).

[45] Inda-Webb, M. E., Jimenez, M., Liu, Q., Phan, N. V., Ahn, J., Steiger, C., Wenthworth, A., Zirtoglu, T., Wong, K., Ishida, K., Fabian, N., Jenskin, J., Kuosmanen, J., Madeni, W., MccNally, R., Hayward, A., Mimee, M., Naedau, P., Chandrasakan, A. P., Yaziiloglu, R. T & Lu, T. K, Sub-1.4 cm3 capsule for detecting labile inflammatory biomarkers in situ. *Nature* **620**, 386–392 (2023).

[46] Cao, Z., Wang, X., Pang, Y., Cheng, S., & Liu, J, Biointerfacial self-assembly generates lipid membrane coated bacteria for enhanced oral delivery and treatment. *Nat Commun* **10**, 5783 (2019).

[47] Peng, P., Feng, T., Yang, X., Nie, C., Yu, L., Ding, R., Zhou, Q., Jiang, X & Li, P, Gastrointestinal Microenvironment Responsive Nanoencapsulation of Probiotics and Drugs for Synergistic Therapy of Intestinal Diseases. *ACS Nano* **17,** 14718–14730 (2023).

[48] Zhou, J., Li, M., Chen, Q., Li, X., Chen, L., Dong, Z., Zhu, W., Yang, Y., Liu, Z & Chen, Q, Programmable probiotics modulate inflammation and gut microbiota for inflammatory bowel disease treatment after effective oral delivery. *Nat Commun* **13**, 3432 (2022).

[49] Yang, J., P, M., Tan, S., Ge, S., Xie, L., Zhou, T., Liu, W., Zhang, K., Zhang, Z., Liu, J & Shi, J, Calcium Tungstate Microgel Enhances the Delivery and Colonization of Probiotics during Colitis via Intestinal Ecological Niche Occupancy. *ACS Cent. Sci.* **9**, 1327–1341 (2023).

[50] Qiao, J., Zeng, R., Chen, Q., Zheng, D., Hao, P., Liu, X, Xhao, F & Zhang, X, Autonomously Assembled Living Capsules by Microbial Coculture for Enhanced Bacteriotherapy of Inflammatory Bowel Disease. *Nano Letters*, **10,** 4375–4383 (2023).

[51] Dai, Z., Yang, X., Wu, F., Wang, L., Xiang, K., Li, P., Lv, Q., Tnaag, J., Dohlman, A., Dai, Lei, Shen, X &You, L, Living fabrication of functional semi-interpenetrating polymeric materials. *Nat Commun* **12**, 3422 (2021).

[52] Praveschotinunt, P., Duray-Thatte, A. M., Gelfat, I., Bahl, F., Chou, D. B & Joshi, N. S, Engineered E. coli Nissle 1917 for the delivery of matrix-tethered therapeutic domains to the gut. *Nat Commun* **10,** 5580 (2019).

[53] Glinel, K., Behrens, A., Langer, R. S., Jaklenec, A. & Jonas, A. M. Nanofibrillar Patches of Commensal Skin Bacteria. *Biomacromol.* **20,** 102–108 (2019).

[54] Li, L. Yang, CC., Ma, B., Lu, S., Liu, J., Pan, Y., Wang, X., Zhang, Y., Wang, H., Sun, T., Liu, D, Hydrogel-Encapsulated Engineered Microbial Consortium as a Photoautotrophic "Living Material" for Promoting Skin Wound Healing. *ACS Appl. Mater. Interfaces* **15**, 6536–6547 (2023).

[55] Sankaran, S., Becker, J., Wittmann, C. & del Campo, A. Optoregulated Drug Release from an Engineered Living Material: Self-Replenishing Drug Depots for Long-Term, Light-Regulated Delivery. *Small* **15**, 1804717 (2019).

[56] Duraj-Thatte, A. M., Manjula-Basavanna, A., Rutledge, J., Xia, J., Hassan, S., Sourlis, A., Rubio, A. G., Lesha, A., Zenkl, M., Kan, A., Weitz, D. A., Zhang, Y. S. & Joshi, N. S. Programmable microbial ink for 3D printing of living materials produced from genetically engineered protein nanofibers. *Nat. Commun.* **12,** 1-8 (2021).

[57] Decante, G., Costa, J. B., Silva-Correia, J., Collins, M. N., Reis, R. L., & Oliveira, J. M. Engineering bioinks for 3D bioprinting. *Biofabrication.* **13,** 032001 (2021).

[58] Rivera-Tarazona, L. K., Campbell, Z. T., & Ware, T. H. Stimuli-responsive engineered living materials. *Soft Matter.* **17,** 785-809 (2021).

[59] Liu, X., Inda, M. E., Lai, Y., Lu, T. K. & Zhao, X. Engineered Living Hydrogels. *Adv. Mater.* 2201326 (2022).

[60] Jin, Y., Kim, J., Lee, J. S., Min, S., Kim, S., Ahn, D. H., Kim, Y. & Cho, S. W. Vascularized liver organoids generated using induced hepatic tissue and dynamic liver-specific microenvironment as a drug testing platform. *Adv. Funct. Mater.* **28,** 1801954 (2018).

[61] Zhang, P., Shao, N., & Qin, L. Recent Advances in Microfluidic Platforms for Programming Cell-Based Living Materials. *Adv. Mater.* **33,** 2005944 (2021).

[62] Chartrain, N. A., Williams, C. B., & Whittington, A. R. A review on fabricating tissue scaffolds using vat photopolymerization. *Acta Biomater.* **74,** 90-111 (2018).

[63] Andreu, A., Su, P. C., Kim, J. H., Ng, C. S., Kim, S., Kim, I., Lee, J., Noh, J., Subramanian, A. S. & Yoon, Y. J. 4D printing materials for Vat Photopolymerization. *Addit. Manuf.* **44,** 102024 (2021).

[64] Narupai, B. & Nelson, A. 100th anniversary of macromolecular science viewpoint: Macromolecular materials for additive manufacturing. *ACS Macro Lett.* **9,** 627-638 (2020).

[65] Smith, P. T., Narupai, B., Tsui, J. H., Millik, S. C., Shafranek, R. T., Kim, D. H. & Nelson, A. Additive Manufacturing of Bovine Serum Albumin-Based Hydrogels and Bioplastics. *Biomacromolecules.* **21,** 484-492 (2019).

[66] Sanchez-Rexach, E., Smith, P. T., Gomez-Lopez, A., Fernandez, M., Cortajarena, A. L., Sardon, H. & Nelson, A. 3D-Printed Bioplastics with Shape-Memory Behavior Based on Native Bovine Serum Albumin. *ACS Appl. Mater. Interfaces*. **13,** 19193-19199 (2021).

[67] Smith, P. T., Altin, G., Millik, S. C., Narupai, B., Sietz, C., Park, J. O., & Nelson, A. Methacrylated Bovine Serum Albumin and Tannic Acid Composite Materials for Three-Dimensional Printing Tough and Mechanically Functional Parts. *ACS Applied Materials & Interfaces*. **18,** 21418–21425 (2022).

[68] Beck, E. C., Barragan, M., Tadros, M. H., Gehrke, S. H., & Detamore, M. S. Approaching the compressive modulus of articular cartilage with a decellularized cartilage-based hydrogel. *Acta biomaterialia*, **38,** 94-105 (2016).

[69] Yu, K., Spiesz, E. M., Balasubramanian, S., Schmieden, D. T., Meyer, A. S., & Aubin-Tam, M. E. Scalable bacterial production of moldable and recyclable biomineralized cellulose with tunable mechanical properties. *Cell Rep. Phys. Sci.* **2,** 100464 (2021).

[70] Gilbert, C., Tang, T. C., Ott, W., Dorr, B. A., Shaw, W. M., Sun, G. L., Lu, T. K. & Ellis, T. Living materials with programmable functionalities grown from engineered microbial co-cultures. *Nat. Mater.* **20,** 691-700 (2021).

[71] Manjula-Basavanna, A., Duraj-Thatte, A. M. & Joshi, N. S. Robust Self-Regeneratable Stiff Living Materials Fabricated from Microbial Cells. *Adv. Funct. Mater.* **31,** 2010784 (2021).

[72] Huang, J., Liu, S., Zhang, C., Wang, X., Pu, J., Ba, F. & Zhong, C. Programmable and printable Bacillus subtilis biofilms as engineered living materials. *Nat. Chem. Biol.* **15,** 34-41 (2019).

[73] Melchels, F. P., Feijen, J. & Grijpma, D. W. A poly (D, L-lactide) resin for the preparation of tissue engineering scaffolds by stereolithography. *Biomaterials.* **30,** 3801-3809 (2009).

[74] Duina, A. A., Miller, M. E. & Keeney, J. B. Budding yeast for budding geneticists: a primer on the Saccharomyces cerevisiae model system. *Genetics.* **197,** 33-48 (2014).

[75] Xue, R., Liu, Y., Zhang, Q., Liang, C., Qin, H., Liu, P. & Wei, Y. Shape changes and interaction mechanism of Escherichia coli cells treated with sericin and use of a sericin-based hydrogel for wound healing. Appl. Environ. Microbiol. **82,** 4663-4672 (2016).

[76] Gaeta, M., Randazzo, R., Villari, V., Micali, N., Pezzella, A., Purrello, R. & D'Urso, A. En Route to a Chiral Melanin: The Dynamic "From-Imprinted-to-Template" Supramolecular Role of Porphyrin Hetero-Aggregates During the Oxidative Polymerization of L-DOPA. *Front. Chem.* **8,** 1188 (2020).

[77] S. Moulay. Dopa/catechol-tethered polymers: bioadhesives and biomimetic adhesive materials. *Polym. Rev.* **54,** 436–513 (2014).

[78] Michalicha, A., Roguska, A., Przekora, A., Budzyńska, B. & Belcarz, A. Poly (levodopa)-modified β-glucan as a candidate for wound dressings. *Carbohyd. Polym.* **272**, 118485 (2021).

[79] Kajisa, T., Yanagimoto, Y., Saito, A. & Sakata, T. Biocompatible poly (catecholamine)-film electrode for potentiometric cell sensing. *ACS Sens.* **3,** 476-483 (2018).

[80] Park, J., Brust, T. F., Lee, H. J., Lee, S. C., Watts, V. J. & Yeo, Y. Polydopamine-based simple and versatile surface modification of polymeric nano drug carriers. *ACS Nano.* **8,** 3347-3356 (2014).

[81] Yang, Q., Liang, J. & Han, H. Probing the interaction of magnetic iron oxide nanoparticles with bovine serum albumin by spectroscopic techniques. *J. Phys. Chem. B.* **113,** 10454-10458 (2009).

[82] Siddiqui, G. A., Siddiqi, M. K., Khan, R. H. & Naeem, A. Probing the binding of phenolic aldehyde vanillin with bovine serum albumin: evidence from spectroscopic and docking approach. *Spectrochim. Acta-A: Mol. Biomol. Spectrosc.* **203,** 40-47 (2018).

[83] Sun, C., Yang, J., Wu, X., Huang, X., Wang, F. & Liu, S. Unfolding and refolding of bovine serum albumin induced by cetylpyridinium bromide. *Biophys. J.* **88,** 3518-3524 (2005).

[84] Salehi, B., Fokou, P. V. T., Sharifi-Rad, M., Zucca, P., Pezzani, R., Martins, N. & Sharifi-Rad, J. The therapeutic potential of naringenin: a review of clinical trials. *Pharmaceut.* **12,** 11 (2019).

[85] Zeng, W., Jin, L., Zhang, F., Zhang, C. & Liang, W. Naringenin as a potential immunomodulator in therapeutics. *Pharmacol. Res.* **135,** 122-126 (2018).

[86] Hernández-Aquino, E., & Muriel, P. Beneficial effects of naringenin in liver diseases: Molecular mechanisms. *World J. Gastroenterol.* **24,** 1679 (2018).

[87] Hu, Y. J., Wang, Y., Ou-Yang, Y., Zhou, J., & Liu, Y. Characterize the interaction between naringenin and bovine serum albumin using spectroscopic approach. *J. Lumin.* **130,** 1394-1399 (2010).

[88] Zhang, Y., Li, Y., Dong, L., Li, J., He, W., Chen, X. & Hu, Z. Investigation of the interaction between naringin and human serum albumin. *J. Mol. Struct.* **875,** 1-8 (2008).

[89] Karygianni, L., Ren, Z., Koo, H. & Thurnheer, T. Biofilm matrixome: extracellular components in structured microbial communities. *Trends Microbiol.* **28,** 668-681 (2020).

[90] Gibson, D. G., Young, L., Venter, J. C., Hutchison, C. A. & Smith, H. O. Enzymatic assembly of DNA molecules up to several hundred kilobases. *Nat. Methods.* **6,** 343 (2009).

[91] Zhou, S., Yuan, S., Nair, P. H., Alper, H. S., Deng, Y. & Zhou, J. Development of a growth coupled and multi-layered dynamic regulation network balancing malonyl-CoA node to enhance (2S)-naringenin biosynthesis in *Escherichia coli*. *Metab. Eng.* **67,** 41-52 (2021).

[92] Morse, N. J., Wagner, J. M., Reed, K. B., Gopal, M. R., Lauffer, L. H. & Alper, H. S. T7 Polymerase Expression of Guide RNAs in vivo Allows Exportable CRISPR-Cas9 Editing in Multiple Yeast Hosts. *ACS Synth. Biol*. **7,** 1075–1084 (2018).

[93] Duraj-Thatte, A.M., Courchesne, N.-M.D., Praveschotinunt, P., Rutledge, J., Lee, Y., Karp, J.M., and Joshi, N.S. Hydrogels: Genetically Programmable Self-Regenerating Bacterial Hydrogels. *Adv. Mater.* **31,** (2019).

[94] Paunović, N., Meyer, D., Krivitsky, A., Studart, A.R., Bao, Y., and Leroux, J.-C. 4D printing of biodegradable elastomers with tailorable thermal response at physiological temperature. *J. Control. Rel.* **361,** 417–426 (2023).

[95] Li, X., Tsutsui, Y., Matsunaga, T., Shibayama, M., Chung, U., and Sakai, T. Precise Control and Prediction of Hydrogel Degradation Behavior. *Macromol*. **44,** 3567–3571 (2011).

[96] Carberry, B.J., Hernandez, J.J., Dobson, A., Bowman, C.N., and Anseth, K.S. Kinetic Analysis of Degradation in Thioester Cross-linked Hydrogels as a Function of Thiol Concentration, pKa, and Presentation. *Macromol*. **55,** 2123–2129 (2022).

[97] DelRe, C., Jiang, Y., Kang, P., Kwon, J., Hall, A., Jayapurna, I., Ruan, Z., Ma, L., Zolkin, K., Li, T. Near-complete depolymerization of polyesters with nano-dispersed enzymes. *Nature* **592,** 558–563 (2021).

[98] Iyer, H., Grandgeorge, P., Jimenez, A.M., Campbell, I.R., Parker, M., Holden, M., Venkatesh, M., Nelsen, M., Nguyen, B., and Roumeli, E. Fabricating Strong and Stiff Bioplastics from Whole Spirulina Cells. *Adv. Funct. Mater.* **33,** 2302067 (2023).

[99] Erdal, N.B., and Hakkarainen, M. (2022). Degradation of Cellulose Derivatives in Laboratory, Man-Made, and Natural Environments. *Biomacromol.* **23,** 2713–2729 (2022).

[100] Su, J., Zhao, K., Ren, Y., Zhao, L., Wei, B., Liu, B., Zhang, Y., Wang, F., Li, J., Liu, Y., Liu, K & Zhang, H, Biosynthetic Structural Proteins with Super Plasticity, Extraordinary Mechanical Performance, Biodegradability, Biocompatibility and Information Storage Ability. Angew. Chem. International Edition **61,** (2022).

[101] Yu, S., Sadaba, N., Sanchez-Rexach, E., Hilburg, S.L., Pozzo, L.D., Altin-Yavuzarslan, G., Liz-Marzán, L.M., Jimenez de Aberasturi, D., Sardon, H., and Nelson, A. 4D Printed Protein-AuNR Nanocomposites with Photothermal Shape Recovery. Adv. Func. Mater. *n/a*, 2311209. (2024)

[102] Mujtaba, A., Keller, M., Ilisch, S., Radusch, H. J., Thurn-Albrecht, T., Saalwachter, K., & Beiner, M. Mechanical properties and cross-link density of styrene–butadiene model composites containing fillers with bimodal particle size distribution. *Macromol*. **45,** 6504-6515 (2012).

[103] Danielsen, S.P.O., Beech, H.K., Wang, S., El-Zaatari, B.M., Wang, X., Sapir, L., Ouchi, T., Wang, Z., Johnson, P.N., Hu, Y., Lundbeg, D. J., Stoychev, G., Craig, S. L., Johnson, J. A., Kalow, J.A., Olsen & B. D., Rubinstein, M. Molecular Characterization of Polymer Networks. *Chem. Rev*. **121,** 5042–5092 (2021).

[104] R. S. Gona, A. S. Meyer. Engineered proteins and three-dimensional printing of living materials. *MRS Bulletin*. 2020, **45**, 1034-1038 (2020).

[105] D. Datta, E. L. Weiss, D. Wangpraseurt, E. Hild, S. Chen, J. W., Golden, S. S. Golden, J. K. Pokorski, JUMP Cell Painting dataset: morphological impact of 136,000 chemical and genetic perturbations. *bioRxiv*, 2023-01 (2023).

[106] S. Molinari, R. F. Tesoriero Jr, D. Li, S. Sridhar, R. Cai, J. Soman, C. M. Ajo-Franklin, A de novo matrix for macroscopic living materials from bacteria.*Nat. Commun*. **13**, 5544 (2022).

[107] M. R. Binelli, P. A. Rühs, G. Pisaturo, S. Leu, E. Trachsel, A. R. Studart, Living materials made by 3D printing cellulose-producing bacteria in granular gels. *Biomater. Adv*. **141,** 213095(2022).

[108] Y. T. Kim, A. Ahmadianyazdi, A. Folch, A 'print–pause–print'protocol for 3D printing microfluidics using multimaterial stereolithography. *Nat. Protoc.* **18**, 1243-1259 (2023).

[109] C. A. Durst, M. P. Cuchiara, E. G. Mansfield, J. L. West, K. J. Grande-Allen, Flexural characterization of cell encapsulated PEGDA hydrogels with applications for tissue engineered heart valves. *Acta Biomater.* **7**, 2467-2476 (2011).

[110] A. L. Nachlas, S. Li, R. Jha, M. Singh, C. Xu, M. E. Davis, Human iPSC-derived mesenchymal stem cells encapsulated in PEGDA hydrogels mature into valve interstitial-like cells. *Acta Biomater*. **71,** 235-246 (2018).

[111] A. D. Benjamin, R. Abbasi, M. Owens, R. J. Olsen, D. J. Walsh, T. B. LeFevre, J. N. Wilking, Light-based 3D printing of hydrogels with high-resolution channels. *BPEX*. **5,** 025035 (2019).

[112] W. Li, M. Wang, H. Ma, F. A. Chapa-Villarreal, A. O. Lobo, Y. S. Zhang, Stereolithography apparatus and digital light processing-based 3D bioprinting for tissue fabrication. *Iscience.* **26,** 106039 (2023).

[113] C. Warr, J. C. Valdoz, B. P. Bickham, C. J. Knight, N. A. Franks, N. Chartrand, P. M. V. Ry, K. A. Christensen, G. P. Nordin, A. D. Cook, Biocompatible PEGDA resin for 3D printing. *ACS Appl. Bio. Mater.* **3,** 2239-2244 (2020).

[114] M. Hisham, G. S. Kumar, A. P. Deshpande, Process optimization and optimal tolerancing to improve dimensional accuracy of vat-photopolymerized functionally graded hydrogels. *RINENG* **14,** 100442 (2022).

[115] Y. Xia, Y. Wu, T. Yu, S. Xue, M. Guo, J. Li, Z. Li, Multifunctional glycerol–water hydrogel for biomimetic human skin with resistance memory function. *ACS Appl. Mater. Interfaces*, **11,** 21117-21125. (2019).

[116] M. Watanabe, H. Li, M. Yamamoto, J. I. Horinaka, Y. Tabata, A. W. Flake. Addition of glycerol enhances the flexibility of gelatin hydrogel sheets; application for in utero tissue engineering. *J. Biomed. Mater. Res. Part B Appl. Biomater.* **109,** 921-931 (2021).

[117] J. Caro-Astorga, K. Y. Lee, T. Ellis. Increasing bacterial cellulose compression resilience with glycerol or PEG400 for robuster engineered living materials. *Carbohydr. Polym.* **4,** 100245 (2022).

[118] F. Jiang, D. Drummer. Curing kinetic analysis of acrylate photopolymer for additive manufacturing by photo-DSC. *Polym.* **12,** 1080 (2020).

[119] K. Wnuczek, A. Puszka, Ł. Klapiszewski, B. Podkościelna. Preparation, thermal, and thermo-mechanical characterization of polymeric blends based on di (meth) acrylate monomers. *Polym.* **13,** 878 (2021).

[120] S. Bhusari, S. Sankaran, A. Del Campo. Regulating bacterial behavior within hydrogels of tunable viscoelasticity. *Adv. Sci.* **9,** 2106026 (2022).

[121] H. Priks, T. Butelmann, A. Illarionov, T. G. Johnston, C. Fellin, T. Tamm, A. Nelson, R. Kumar, P. J. Lahtvee. Physical confinement impacts cellular phenotypes within living materials. *ACS Appl. Bio. Mater.* **3,** 4273-4281(2020).

[122] The Crohn's & Colitis Foundation of America, https://www.crohnscolitisfoundation.org (accessed May 11, 2020).

[123] American Cancer Society, Key Statistics for Colorectal Cancer, https://www.cancer.org/cancer/colon-rectal-cancer/about/key-statistics.html (accessed May 11, 2020).

[124] Fakhoury, M.; Negrulj, R.; Mooranian, A.; Al-Salami, H, Inflammatory Bowel Disease: Clinical Aspects and Treatments. *J. Inflamm. Res.* **7,** 113-120. (2014).

[125] Zimová, L.; Vetchý, D.; Muselík, J.; Štembírek, J, The Development and In Vivo Evaluation of A Colon Drug Delivery System Using Human Volunteers. *Drug Deliv.* **19,** 81-89 (2012).

[126] Pinto, J. F, Site-Specific Drug Delivery Systems Within the Gastro-Intestinal Tract: From the Mouth to the Colon. *Int. J. Pharm.* **395,** 44-52 **(2010).**

[127] Arafat, M.; Fouladian, P.; Blencowe, A.; Albrecht, H., Song, Y.; Garg, S, Drug-Eluting Non-Vascular Stents for Localised Drug Targeting in Obstructive Gastrointestinal Cancers. *J. Control Release.* **308,** 209-231 (2019).

[128] Kraitzer, A.; Zilberman, M, Controlled Release of Antiproliferative Drugs from Polymeric Systems for Stent Applications and Local Cancer Treatment. *Adv. Eng. Mater.* **14,** 294-310 (2012).

[129] Borandeh, S., van Bochove, B., Teotia, A., & Seppälä, J, Polymeric drug delivery systems by additive manufacturing. *Adv. Drug Delivery Review.* **173**, 349-373 (2021).

[130] Hmar, E. B. L., Paul, S., & Sharma, H. K, An Insight into the Combination of Probiotics and their Implications for Human Health. *EMDDT (Formerly Current Drug Targets-Immune, Endocrine & Metabolic Disorders),* **24,** 1-12 (2024).

[131] Han, Z. Y., Zhang, C., An, J. X., Qiao, J. Y., & Zhang, X. Z, Microalgal biomass-assisted delivery of probiotics for modulation of gut homeostasis and alleviation of intestinal inflammation. *Nano Today*, **54,** 102093 (2024).

[132] Jakubczyk, D., Leszczyńska, K., & Górska, S, The effectiveness of probiotics in the treatment of inflammatory bowel disease (IBD)—a critical review. *Nutr.* **12**, 1973. (2020).

[133] Naseer, M., Poola, S., Ali, S., Samiullah, S., & Tahan, V, Prebiotics and probiotics in inflammatory bowel disease: where are we now and where are we going?. *Curr. Clin. Pharmacol.* **15**, 216-233 (2020).

[134] Reis, S. K., Socca, E. A. R., de Souza, B. R., Genaro, S. C., Durán, N., & Fávaro, W. J, Tissue and Cell Effects of probiotic supplementation on chronic inflammatory process modulation in colorectal carcinogenesis. *Tissue and Cell*, 102293 (2024).

[135] Kim, H. J., Jeon, H. J., Kim, J. Y., Shim, J. J., & Lee, J. H, Lactiplantibacillus plantarum HY7718 Improves Intestinal Integrity in a DSS-Induced Ulcerative Colitis Mouse Model by Suppressing Inflammation through Modulation of the Gut Microbiota. *Int. J. Mol. Sci.* **25,** 575 (2024).

[136] Chen, H., Lei, P., Ji, H., Yang, Q., Peng, B., Ma, J., Fang, Y,m Qu, L. I., Li, H., Wu. W., Jin, L & Sun, D, Advances in Escherichia coli Nissle 1917 as a customizable drug delivery system for disease treatment and diagnosis strategies. *Mater. Today Bio*.**18,** 100543 (2023).

[137] Han, S., Lu, Y., Xie, J., Fei, Y., Zheng, G., Wang, Z., Liu, J., Ling, Z., Berrglund, B., Yao, M & Li, L, Probiotic gastrointestinal transit and colonization after oral administration: A long journey. *Front. Cell. Infect. Microbiol.* **11,** 609722 (2021).

[138] da Silva, M. N., Tagliapietra, B. L., do Amaral Flores, V., & dos Santos Richards, N. S. P, In vitro test to evaluate survival in the gastrointestinal tract of commercial probiotics. *Currr. Researc. Food Sci.* **4,** 320-325 (2021).

[139] Bezkorovainy, A, Probiotics: determinants of survival and growth in the gut. *AJCN.* **73,** 399-405 (2001).

[140] Vertzoni, M., Diakidou, A., Chatzilias, M., Söderlind, E., Abrahamsson, B., Dressman, J. B., & Reppas, C, Biorelevant media to simulate fluids in the ascending colon of humans and their usefulness in predicting intracolonic drug solubility. *Pharm. Res.* 27, 2187-2196 (2010).

[141] Begley, M., Hill, C., & Gahan, C. G, Bile salt hydrolase activity in probiotics. *AEM.* **72,** 1729-1738 (2006).

[142] Darwish, M. S., Abou-Zeid, N. A., Khojah, E., Al Jumayi, H. A., Alshehry, G. A., Algarni, E. H., & Elawady, A. A, Supplementation of Labneh with Passion Fruit Peel Enhanced Survival of E. coli Nissle 1917 during Simulated Gastrointestinal Digestion and Adhesion to Caco-2 Cells. *Foods*, **11,** 1663 (2022).

[143] Avdagić, N., Zaćiragić, A., Babić, N., Hukić, M., Šeremet, M., Lepara, O., & Nakaš-Ićindić, E, Nitric oxide as a potential biomarker in inflammatory bowel disease. *BJBSM* **13,** 5 (2013).
[144] Rachmilewitz, D., Stamler, J. S., Bachwich, D., Karmeli, F., Ackerman, Z., & Podolsky, D. K, Enhanced colonic nitric oxide generation and nitric oxide synthase activity in ulcerative colitis and Crohn's disease. *Gut*, **36,** 718 (1995).
[145] Ding, X., Hu, X., Chen, Y., Xie, J., Ying, M., Wang, Y., & Yu, Q, Differentiated Caco-2 cell models in food-intestine interaction study: Current applications and future trends. *Trends in Food Sci. Technol.* **107,** 455-465 (2021).
[146] Sambuy, Y., De Angelis, I., Ranaldi, G., Scarino, M. L., Stammati, A., & Zucco, F, The Caco-2 cell line as a model of the intestinal barrier: influence of cell and culture-related factors on Caco-2 cell functional characteristics. *CBT.* **21,** 1-26 (2005).
[147] Van Breemen, R. B., & Li, Y, Caco-2 cell permeability assays to measure drug absorption. *Expert Opinion on Drug Metabol. Toxicol.* **1,** 175-185 (2005).
[148] Broeders, J. J., Blaauboer, B. J., & Hermens, J. L, In vitro biokinetics of chlorpromazine and the influence of different dose metrics on effect concentrations for cytotoxicity in Balb/c 3T3, Caco-2 and HepaRG cell cultures. *Toxicol. in vitro*, **27,** 1057-1064 (2013).
[149] Page, B., Page, M., & Noel, C, A new fluorometric assay for cytotoxicity measurements in-vitro. *Int. J. Oncol.* **3,** 473-476 (1993).
[150] Sun, J., Zhang, X., Broderick, M., & Fein, H, Measurement of nitric oxide production in biological systems by using Griess reaction assay. *Sensors*, **3,** 276-284 (2003).
[151] Veloso, P. M., Machado, R., & Nobre, C, Mesalazine and inflammatory bowel disease–From well-established therapies to progress beyond the state of the art. *Eur. J. Pharm. Biopharm.* **167,** 89-103 (2021).
[152] Lu, R., Zhou, Y., Ma, J., Wang, Y., & Miao, X, Strategies and mechanism in reversing intestinal drug efflux in oral drug delivery. *Pharm.* **14,** 1131 (2022).
[153] Ren, S., & Lien, E. J. Caco-2 cell permeability vs human gastro-intestinal absorption: QSPR analysis. *Prog. Drug Res.* 1-23 (2000).
[154] Yazdanian, M., Glynn, S. L., Wright, J. L., & Hawi, A, Correlating partitioning and Caco-2 cell permeability of structurally diverse small molecular weight compounds. *Pharm. Res.* **15,** (1998).

VITA

Gokce Altin Yavuzarslan is a dedicated researcher with a Ph.D. in Molecular Engineering from the University of Washington (2018-2024). Her expertise lies in the innovative realm of engineered living materials (ELMs) and their applications in treating gastrointestinal inflammations. Throughout her academic journey, she earned a master's degree in molecular engineering (2018-2020) and conducted significant research at Istanbul Technical University, contributing to the fields of food engineering and functional food formulations. As a Research Assistant at the University of Washington since 2018, under the guidance of Prof. Alshakim Nelson, Gokce has spearheaded projects focused on in situ production and continuous delivery of anti-inflammatory agents using 3D printed ELMs. Her work includes tailoring microbial-polymer interactions to adjust material properties and developing bioreactors with tunable stiffness and toughness. Prior to her Ph.D., Gokce served as a Research Scientist at BIOACTIVE Research & Innovation in Istanbul (2015-2018), investigating the antioxidant and anti-inflammatory properties of polyphenols and omega-3 fatty acids. She also contributed significantly to the field of nanotechnology during her research internship at Harvard Medical School. Gokce has been recognized for her scientific achievements, receiving the Molecular Engineering & Sciences Scientific Achievement Award in 2023 and the 1st place Poster Award at the Gordon Research Conference in Additive Manufacturing of Soft Materials in 2022. Her commitment to education and outreach is evident in her involvement in activities like "Introduce a Girl to Green Technology" and "Introduce a Girl to Biotechnology." Her rich publication record and patent reflect her expertise in material formulation, nanotechnology, and bioactive compounds.